**SKB**

# Fracture parameterisation for repository design and post-closure analysis (Post), phase 2, 3 and 4 – Final Report

**Ignacio Pérez Rey**

**Fredrik Johansson**

**Diego Mas Ivars**

**Hossein A Kasani**

**Jörgen Larsson**

**Lars Jacobsson**

**Mathias Flansbjer**

SVENSK KÄRNBRÄNSLEHANTERING

# Fracture parameterisation for repository design and post-closure analysis (Post), phase 2, 3 and 4 – Final Report

Ignacio Pérez Rey[1,2], Fredrik Johansson[2], Diego Mas Ivars[2,3],

Hossein A Kasani[4], Jörgen Larsson[5], Lars Jacobsson[5],

Mathias Flansbjer[5]

1 University of Vigo
2 KTH Royal Institute of Technology
3 Svensk Kärnbränslehantering AB
4 Nuclear Waste Management Organization
5 RISE Research Institutes of Sweden

# Abstract

The prediction of fracture deformations is one of the key aspects when planning the safety assessment of a geological repository for spent nuclear fuel excavated in a crystalline rock mass. A secondary fracture shear displacement caused by a post-glacial earthquake having the potential of intersecting the deposition holes has been identified as a threat to the integrity of the copper canister as per the KBS-3 disposal concept. To study the mechanical behaviour of large fractures exposed to a shear displacement of 50 mm, the project Parametrisation of Fractures (POST) was initiated.

The initial stage of the POST project was established and carried out from 2014 to 2016 by Posiva, SKB and NWMO with the objective of developing the strategy and guidelines for characterising and assessing fracture stability at the deposition holes. However, the project presented some limitations (i.e., in finding representative fracture sets and difficulties in conducting the associated experiments under controlled conditions). This led to the conclusion that studying large fractures under controlled laboratory conditions would minimize experimental uncertainties. However, there is a lack of shear test data for larger rock fractures tested under realistic constant normal stiffness (CNS) conditions subjected to representative normal stress levels. Therefore, the development of a new laboratory shear testing device capable of accommodating a 50 mm shear displacement up to 10 MPa normal stresses and CNS conditions was recommended.

This report contains the main activities carried out to experimentally investigate the mechanical properties of rock fractures through high-quality laboratory normal and direct shear tests under certain conditions, representative of a 400–500 m depth nuclear waste repository to be developed at Forsmark (Sweden). The project was carried out by SKB, NWMO, RISE and KTH during the years 2017–2024, and was divided into three stages (2, 3, and 4).

These activities covered, first, the design, manufacturing and validation of a large shear testing equipment able to perform normal and shear loading tests accurately. Subsequently, a comprehensive testing program comprising several normal and direct shear tests of natural (typical of the repository) and tensile induced (ultimate case with respect to expected roughness and dilation) rock fractures at three different scales (35 mm × 70 mm, 70 mm × 100 mm, and 300 mm × 500 mm), and under constant normal load (CNL) and CNS conditions was carried out. From a statistical analysis of these results, no effect of scale on the shear strength (defined as the onset of full shear slip) could be observed with a 95 % significance. Furthermore, the dilation-induced strengthening effect on the shear strength after fully mobilised shear slip (at approximately 30–50 mm of shear displacement) for the tested fractures under CNS conditions were verified for the large-scale specimens.

The suitability of ultra-high strength concrete replica fractures, either showing a natural match or an almost perfect match, for parametric investigations into the mechanical properties of hard rock fractures, was also studied through an ad-hoc experimental manufacturing and testing program. The replica manufacturing method, in combination with a novel procedure for geometric quality assessment developed within the project, were concluded to be suitable to use for further parameter studies.

In parallel to the mechanical investigations, further rock and replica fracture characterisation was made by resorting to state-of-the-art technologies, specifically, high-resolution geometry scanning of the fracture surfaces before and after testing, contact pressure distribution and acoustic emission measurements. These investigations have generated a comprehensive and well-document dataset, enabling future use for improvements on already existing shear strength criteria and development of new ones.

# Sammanfattning

Att kunna prediktera deformationer i bergsprickor är en av de viktigaste aspekterna vid planering och säkerhetsbedömning av ett geologiskt slutförvar för använt kärnbränsle placerad i en kristallin bergmassa. En sekundär skjuvförskjutning på 50 mm orsakad av en postglacial jordbävning har potential att skära av deponeringshålen där det använda kärnbränslet placeras. Detta har identifierats som ett hot mot kopparkapselns integritet enligt deponeringskonceptet KBS-3. För att studera det mekaniska beteendet av större bergsprickor med upp till 50 mm skjuvförskjutning initierades projektet "Parametrisation of Fractures" (POST).

Den inledande fasen av POST-projektet etablerades och genomfördes från 2014 till 2016 av Posiva, SKB och NWMO med målet att utveckla en strategi och riktlinjer för att karakterisera och bedöma stabiliteten vid deponeringshålen. Erfarenheter från projektet visade dock på vissa svårigheter och begränsningar (t.ex. när det gäller att hitta representativa sprickor och att genomföra de tillhörande experimenten). Detta ledde till slutsatsen att studier av större sprickor bör genomföras under kontrollerade laboratorieförhållanden, vilket minimerar de experimentella osäkerheterna. Det saknas emellertid testdata från skjuvförsök för större bergsprickor som testats under representativa normala spänningsnivåer under konstant normal styvhet (CNS). En ny storskalig utrustning för skjuvprovning utvecklades därför i projektet som kan hantera en skjuvförskjutning på upp till 50 mm. I utrustningen kan provning utföras under både konstant normalbelastning (CNL) och CNS-förhållanden med normalspänningar på upp till 10 MPa.

Denna rapport innehåller de huvudsakliga aktiviteterna som genomfördes för att experimentellt undersöka de mekaniska egenskaperna hos storskaliga bergsprickor. Högkvalitativa normalbelastnings- och skjuvförsök genomfördes i laboratorium under förhållanden representativa för det 400–500 m djupa slutförvar som ska utvecklas i Forsmark (Sverige). Projektet genomfördes av SKB, NWMO, RISE and KTH under åren 2017–2024 och var uppdelat i tre etapper (2, 3 och 4).

Dessa aktiviteter omfattade inledningsvis konstruktion, tillverkning och validering av en stor utrustning som kan utföra försök med hög noggrannhet under normal- och skjuvbelastning. Därefter genomfördes ett omfattande försöksprogram som omfattade flera normalbelastnings- och skjuvförsök av naturliga (typiska för förvaret) och draginducerade (mest extrema fallet med avseende på förväntad råhet och dilatation) bergsprickor. Försöken genomfördes i tre olika skalor (35 mm × 70 mm, 70 mm × 100 mm och 300 mm × 500 mm) under både CNL och CNS förhållanden. Baserat på en statistisk analys kunde det med 95 % signifikans dras slutsatsen att någon effekt från provskalan på skjuvhållfastheten inte kunde observeras (definierad vid fullt mobiliserad glidning). Dessutom verifierades en signifikant ökad skjuvhållfasthet för de storskaliga proverna efter 30–50 mm skjuvdeformation under CNS-förhållanden.

Lämpligheten att använda replikat av ultrahöghållfast betong för sprickor i hårt berg med naturlig eller nästan perfekt matchning för parametriska undersökningar av de mekaniska egenskaperna studerades genom ett ad-hoc anpassat experimentellt tillverknings- och testprogram. Resultaten från den utvecklade metoden för repliktillverkning i kombination med en ny metodik för geometrisk kvalitetsbedömning som utvecklats inom projektet visade att metoden är lämplig att använda för vidare parameterstudier av sprickors mekaniska egenskaper.

Parallellt med de mekaniska undersökningarna gjordes ytterligare karakterisering av berg- och repliksprickor genom att använda modern teknik som högupplöst geometrisk skanning av sprickytorna före och efter skjuvprovning samt kontakttrycksfördelning och akustiska emissionsmätningar. Tillsammans har dessa undersökningar genererat en omfattande och väldokumenterad uppsättning av data, vilka kan användas i framtida forskning för att förbättra befintliga modeller för prediktion av skjuvhållfasthet och utveckla nya.

# Contents

# 1 Introduction

## 1.1 Background

Prediction of fracture deformations around a geological repository for spent nuclear fuel is one of the key aspects included in the safety assessment of the repository. For example, a hypothetical secondary fracture shear displacement during a post-glacial earthquake in excess of 50 mm along fractures that intersect deposition holes is considered, regarding acceptability criteria, a threat to the integrity of the copper canister in the KBS-3 repository concept (SKB 2011). The principles of the KBS-3 concept for storage of spent nuclear fuel are illustrated in Figure 1-1. In addition, fracture normal and shear displacement induced by thermal, glacial, or seismic load may also alter the groundwater flow.

Thus, the initial motivation for the first phase of the POST (Parameterisation Of Fractures) project, carried out during the years 2014–2016, was to demonstrate that a 50 mm slip of in situ fractures in a nuclear waste repository at a depth of around 450 m in crystalline rock mass is extremely unlikely. Several in situ experiments at Äspö HRL in Sweden and ONKALO in Finland were planned, designed, and studied via computer simulations (Mas Ivars et al. 2015, Valli and Hakala 2016). The PUSH Test, which was an in-situ shear test with a constant normal stiffness (CNS) boundary condition, was carried out accompanied by back calculations (Valli et al. 2016). It was observed that the shear resistance increased as an effect of the rough fractures in combination with a shear displacement induced fracture dilatancy. The results emphasised the importance of characterizing the geometrical properties of the fractures and the CNS loading condition. The other in situ experiments were not realised due to the experimental complexity, uncertainties, and high associated costs. Small scale direct shear experiments were carried out on specimens with breccia and calcite infilled fractures (100 mm ×100 mm) under constant normal load (CNL) and CNS conditions in the laboratory. The effect of the soft infill materials in the fracture helped to constrain the shear-induced dilatancy occurring in the experiments. Consequently, there were no difference in the results between CNL and CNS loading conditions. Moreover, contact pressure distribution measurements prior to shearing in laboratory direct shear tests on the already referred fractures showed partly sparse contacts, in the order of 30–60 % of the fracture total nominal area (Jacobsson 2016). In addition, surfaces of natural fractures were scanned by 3D photogrammetry which produced point clouds that were used to create realistic numerical models in 3DEC for simulating the shear behaviour.
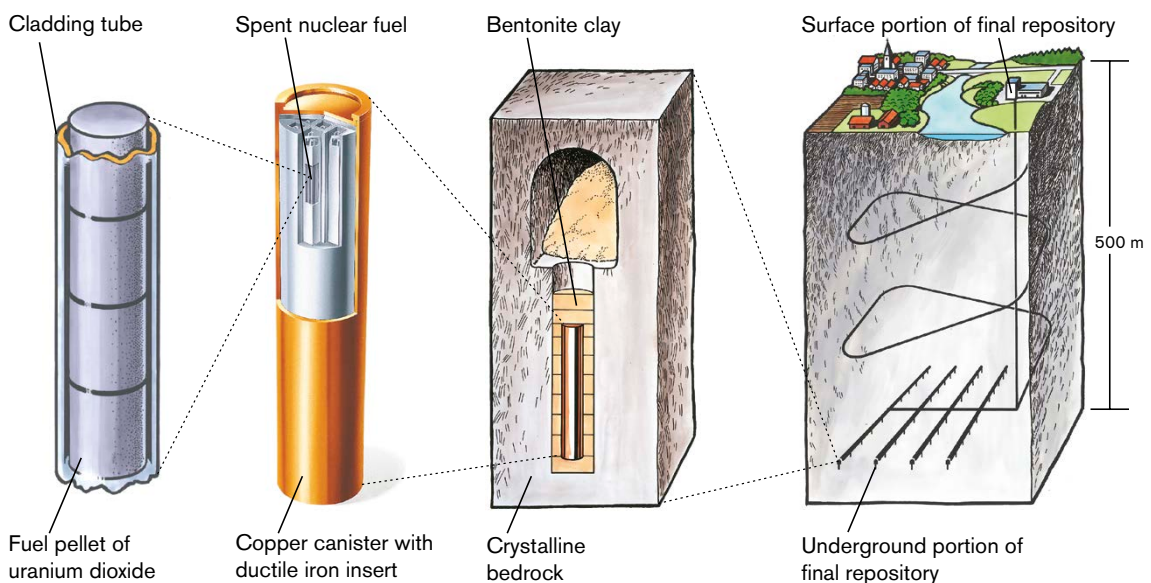


*Figure 1-1. The KBS-3 concept for storage of spent nuclear fuel (SKB 2011).*

The initial part of the POST project revealed that there are several challenges associated with field testing including finding fracture sets representative of the geological conditions potentially encountered in an underground repository at about 450 m depth at Forsmark, difficulties in conducting the experiments, and large uncertainties which result in these tests being cost ineffective. It was concluded that to minimize experimental uncertainties, large scale fractures would be better studied under controlled laboratory conditions. Part of the uncertainties lies in the lack of shear test data for larger rock fractures under realistic CNS normal loading boundary conditions and representative normal stress levels to better understand the effects of fracture scale and their incorporation in the models. Therefore, it was recommended that a new laboratory shear testing device should be developed with the ability to accommodate shear displacement up to 50 mm under normal stresses up to 10 MPa and CNS conditions. Even though the peak shear strength of fractures usually occurs at relatively small shear displacements, especially for well mated fractures under CNL conditions, under CNS conditions the large-scale undulation of the fracture influences the peak shear strength due to dilation. This results in in an increased shear strength with shear displacement; an effect that also is more pronounced in hard, crystalline rock. It is therefore important to investigate the shear strength up to a shear displacement of 50 mm (considered a maximum allowed shear displacement of the copper canisters). A second recommendation was to develop a methodology for replicating fractures for studying different loading conditions on specimens with identical fracture surfaces and at different fracture scales (Siren et al. 2017).

The mechanical behaviour of rock fractures depends on the *rock material properties*, the *fracture geometry*, the *loading state*, and the *scale*. Deformation, strength, fracturing, and friction properties of the rock material stem from its microstructure, composition, and degree of alteration – they all contribute to the fracture behaviour. Concerning the fracture geometry, the composite fracture topography, that consists of the fracture surface roughness, the degree of matedness (closely related to aperture), and infill materials, directly affects the fracture behaviour. The local stress state of a fracture in a rock mass is difficult and complex to determine since the loads depend on the in-situ stress state and the additional stress that is generated during the shear displacement due to the constraint imposed by the surrounding rock. For this reason, fractures at greater depth are best represented to be under CNS, whereas fractures at shallow depth are under CNL conditions (Goodman, 1976). Dilation induced during shear displacement under CNS conditions increases the normal stresses and thus the frictional shear strength. However, previous in-situ and laboratory fracture shear experiments, with a few exceptions, are either conducted on small specimens (up to 200 mm) or on larger specimens at low normal stresses (up to 1– 2 MPa). Only limited investigations have been conducted under CNS loading conditions on fractures in hard rock subjected to a normal stress of 5 to 10 MPa, representative for the stress state at a repository depth under both CNL and CNS loading conditions; and no investigations at all have been done under these conditions under a 50 mm shear displacement. A gap in knowledge about the mechanical properties of rock fractures under these conditions therefore exists.

The effect of fracture scale on shear strength has previously been extensively observed and studied in laboratory and in-situ experiments. The general observation is that the peak shear strength decreases but the associated shear displacement increases with increasing fracture size for natural rock fractures (Bandis et al. 1981). However, increasing shear strength with increasing fracture size or no scale effect has also been reported by others, see for example the review in (Bahaaddini et al. 2014). Furthermore, it has been suggested that the degree of fracture matedness in combination with the sample size and roughness plays a controlling role on the peak shear strength (Johansson 2016). Due to these contradictory results, there is a need to clarify if a scale effect is present or not in the mechanical properties of rock fractures.

In the last decade, there has been a rapid development in characterisation techniques which has increased our ability to obtain an accurate description of the fracture topography before and after the laboratory tests, using high resolution optical scanning of the fracture surfaces. These advances have also enabled us to monitor the normal and shear displacements on the fracture plane via local displacement transducers and Digital Image Correlation (DIC), which can be used to generate a set of data that is richer and more complete than currently available data. These technological developments have made it possible for direct shear experiments to provide unique data that can be used for further research and development on constitutive models for rock fractures. Finally, the use of high-strength concrete replicas of rock fractures to study their mechanical behaviour is an unexplored approach with good potential in conjunction with the aforementioned technical developments.

## 1.2    Project phases

Due to the multi-year plan for the continuation of the initial POST project, it was decided to divide administratively the POST2 project into POST2, POST3 and POST4 phases. This made it easier for the main funding organisations, the Nuclear Waste Management Organization (NWMO) of Canada and the Swedish Nuclear Fuel and Waste Management Company (*Svensk Kärnbränslehantering AB*, SKB), to run and control the project and its planned deliverables. However, these three phases of the project, POST2, POST3 and POST4 have the exact same overall objectives, as described below in Section 1.3.

## 1.3    Aim

The overall aim of the POST project for the phases 2, 3 and 4 was to experimentally investigate the mechanical properties of rock fractures by conducting high-quality laboratory direct shear testing under conditions representative for the nuclear waste repository planned at Forsmark. These conditions imply unfilled rock fractures in hard crystalline granitic rock under normal stresses representative of the planned repository depth. Due to the previous learning from the POST project in phase 1, which experienced difficulties to perform in-situ shear tests and to obtain results with high quality, it was recommended (as previously described above) that future phases of the POST project preferably should perform research in controlled laboratory environments (Siren et al. 2017). Therefore, all testing in the phases 2, 3, and 4 covered in this report were chosen to be performed in laboratory.

The specific objectives of the project were to:

*   Develop a laboratory equipment for conducting well-controlled experiments on large rock fracture specimens and their replicas (as explained in Section 3.6.2) at relatively large normal stresses under CNL and CNS conditions while allowing a 50 mm shear displacement.

*   Determine the mechanical behaviour of large rock fractures subjected to 50 mm of shear displacement including shear strength, normal and shear stiffnesses, and dilation under CNS and CNL conditions.

*   Assess and verify the expected strengthening effect due to dilation effects under CNS conditions.

*   Clarify if any scale effect could be observed on the mechanical parameters when samples on rock fractures of different sizes are tested.

*   Investigate if replicas are suitable to use for parameter investigations of the mechanical properties of hard rock fractures.

*   Generate a comprehensive and well-documented dataset using best available standards and techniques for future research to enable subsequent improvement on existing constitutive models and development of new ones.

## 1.4    Disposition

The report starts in Chapter 2 with a description of the methodology used to reach the specific objectives of the project. This chapter also includes the test plan covering all direct shear test performed, both on rock samples and replicas. Chapter 3 describes the cutting and preparation of the rock and replica samples. In Chapter 4, the characterisation of intact rock and replica material as well as the fracture properties are presented. In Chapter 5, the shear test equipment used for the direct shear tests is described, especially the large-scale shear test equipment developed for this project. Chapter 6 presents the results of the performed shear tests, which are thereafter discussed in Chapter 7. Conclusions are presented in Chapter 8. Certain chapters of this summary report correspond to other reports prepared by RISE, where the information is presented in greater detail. For a more in-depth analysis of specific aspects of this study, the reader is encouraged to refer to these supplementary documents, namely: Jacobsson et al. (2024a, 2024b, 2024c) and Flansbjer et al. (2024).

## 1.5 Limitations

The normal loading and direct shear test within this project were performed on rock samples and replicas corresponding to hard, crystalline rock representative for the conditions at the planned nuclear waste repository at Forsmark. Thus, only granite rock samples were tested in this project. No other rock types were tested.

The tests were also performed under relatively high normal stresses corresponding to the repository depth. No shear tests were performed at low normal stresses and the influence from changes in initial normal stresses has not been studied.

Furthermore, the aim of the project is to investigate the shear strength under CNL and CNS conditions, given the current characteristics of the fracture (including roughness, uniaxial compressive strength of the fracture surface, aperture, etc.). The aim is not to recreate the historical shear displacement and shear strength of the fractures (which some of the fracture mya have experienced in the past).

The term scale effect on the peak shear strength in the report refers to fractures tested in the laboratory up to a sample size of 300 mm × 500 mm and does not refer to the total in-situ size. Large scale undulations (on scales larger than the laboratory sample size) are thus not captured in the performed shear tests.

The testing program did not include the assessment of normal loading and direct shear tests on natural fractures with infilling or coating. In the event the studied natural fractures have any infilling or coating, their potential effect has not been considered in these stages of the POST project.

Replicas were only tested at small scale. The original project plan included large-scale testing of replicas. However, constraints in budget and time of the project, implied that the test plan for the large-scale replicas was abandoned. Being able to perform parametric studies was neither deemed critical for the project objectives.

All direct shear test in the project were performed at a constant shear rate. Influence from changes in shear rate on the mechanical properties of the fractures were not studied. Furthermore, direct shear tests were conducted only under one initial normal stress level, with a single stiffness value applied during tests on rock fractures (although covered in the replica study).

# 2 Methodology

This section outlines the methodology followed to perform a sound mechanical characterisation of rock fractures under conditions representative of the planned nuclear waste repository in Forsmark, and thereby aligning with the previously described specific objectives. Tests on two types of rock fractures, natural and tensile-induced, and replicas were performed in this project. Further information about the structure of the project and methodology can be found in Jacobsson et al. (2021).

## 2.1 Overview

The idea is to use several methods in the workflow to characterize and quantify the fractures and their mechanical behaviour and combine these to get a better and fulsome picture of the deformation and wear processes in the fractures. A comprehensive overview of the characterisation and testing process both for rock and concrete (replica) fractures, which shows the different steps in the workflow is presented in Figure 2-1.The blue boxes represent the main processes to which the fractures were subjected to (from preparation or manufacturing to final analyses, discussion and conclusions). The green boxes represent complementary processes of analysis, on some occasions common or related to both types of fractures. The different parts are linked to and support each other which are shown by the arrows in the diagram. The described process for the rock fractures was conducted for three specimen scales (small, medium and large), whereas the replicas of rock fractures were made only in one scale (medium).

The first step consisted in finding an appropriate rock quarry able to provide granitic material representative of that found in the Forsmark area, where the nuclear waste repository will be built. A granite quarry in Flivik (Sweden) was selected, from which large granite blocks (ranging each from 15 to 20 ton) were extracted. Blocks that contained thin cracks were found and selected, and two of them were later used for preparing the specimens. Subsequent subdivision of these blocks through cutting and splitting operations were performed at *Emmaboda Granit* stone processing plant in Emmaboda, Sweden. The splitting operations were done to produce fresh tensile-induced rock fractures. Finally, the specimens were cut to the specified dimensions at *Söders* stonemasonry in Kinna, and at RISE (Research Institutes of Sweden) in Borås. Geometry scanning was done on the unprocessed main blocks and some of the subdivided blocks to determine the fracture traces seen from the block sides. Replicas were made of ultra-high strength concrete Ducorit D4 having approximately the same mechanical properties as the intact rock. This enables a good methodology for replicating the fractures. The process of sample preparation, from the large blocks to the final rock and replica material specimens is covered in detail in Chapter 3.
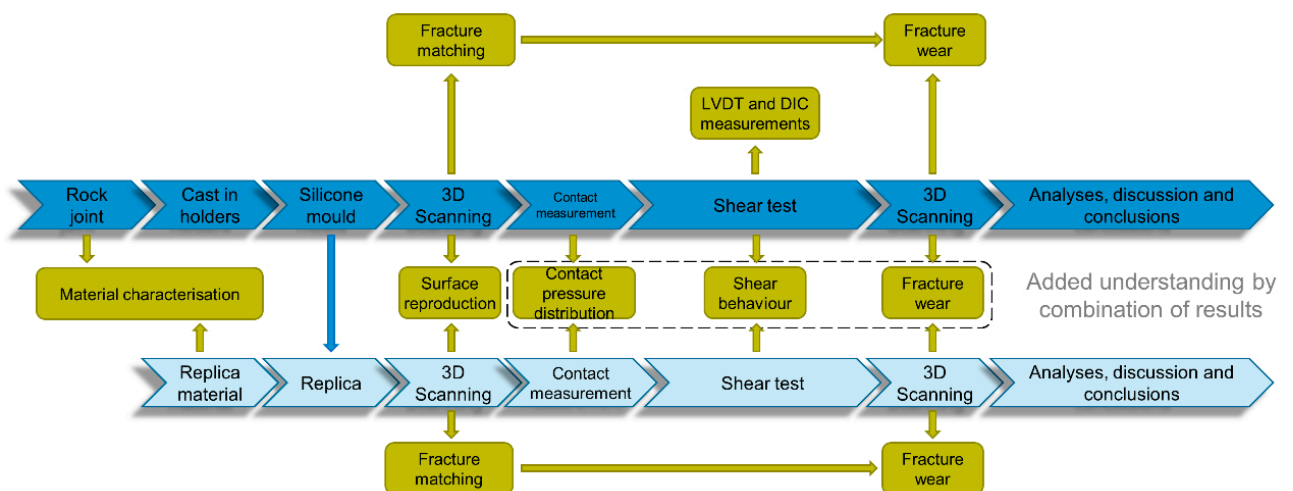


*Figure 2-1.* *Overview of the methods for the mechanical characterisation and testing of rock (dark blue) and replica (light blue) fractures within the project. Complementary processes are shown by green boxes.*

The mechanical characterisation of both rock and replica material (concrete) was performed by means of different laboratory tests (i.e. uniaxial compressive strength, direct tensile strength and splitting (Brazilian) indirect tensile strength tests) on cylindrical specimens. Changes in concrete specimens' geometries associated with the curing process were also assessed through shrinkage tests on concrete rectangular-based slabs. The basic frictional behaviour of planar rock and concrete (saw-cut) surfaces was studied by means of tilt tests and complemented with micro-roughness surface-texture assessment performed at the University of Vigo (Spain). Supplementary surface-based strength measurements were also performed on rock and concrete fractures and block surfaces through Schmidt hammer tests.

Rock and replica fracture surfaces were also characterised by different approaches, prior and after the tests enabling fracture wear analyses. Concerning the large-size fractures, 3D laser scanning technology was used. In what refers to the medium- and small-size fracture surfaces, a blue-LED structured-light-based technology was used. From the scans high-quality point clouds and surface models were obtained.

The development of the manufacturing process and quality assessment of the final replica fracture specimens (as described in Chapter 3) was supported by a novel method to assure their geometric compliance with the original surface (Larsson et al. 2023a, b). The method was entirely developed within this project and relies on two novel suggested parameters able to quantify geometric deviations between the rock fractures and their corresponding replicas to determine the replication accuracy or spot manufacturing problems. Further analyses on the contact areas between the blocks constituting the direct shear test specimens and on several surface features were also implemented. Images retrieved from processed pressure-sensitive film were assessed, and contact analyses were also performed based on 3D point cloud comparisons between the upper and lower specimens' blocks by means of dedicated software (GOM Inspect Pro and MATLAB). The mechanical characterisation of materials (rock and concrete) and fracture properties through the already mentioned tests and techniques are covered in detail in Chapter 4.

Several sets of normal load and direct shear tests under two boundary conditions (constant normal load and constant normal stiffness) were performed to determine shear strength and normal and shear stiffness of the fractures at different scales (see Section 2.2). Note that during the shear test, the load is continuously corrected due to the reduced contact area between the upper and lower part of the samples. This implies that a more correct term is constant normal stress rather than constant normal load. However, in this report, the term constant normal load has been used since it is the most common terminology for this type of test. Two testing apparatuses were used for this purpose. A new direct shear test machine capable of testing up to $400 \times 600$ mm fractures was specifically designed and manufactured for this project and was used to test the large specimens. The machine was based around the existing four-pillar load frame (20 MN) at RISE in Borås as already suggested during phase 1. An existing direct shear testing machine at RISE in Borås was used for tests on medium- and small-size fractures. A more detailed description of these machines, measuring devices and methods, and the types of tests performed in this project is presented in Chapter 5. This includes also the description of some novel experimental improvements such as local fracture displacements measurements based on DIC in addition to conventional non-local indirect measurements on the shear boxes by Linear Variable Displacement Transformers (LVDTs) and stiffness compensation during CNS tests.

A comprehensive set of results was derived from the testing program presented hereinafter, for both tensile-induced, natural and replica fractures. All these results are summarised in Chapter 6, and further discussed in Chapter 7. The previous steps served to reach the main conclusions of this project, as well as possible future recommendations, presented in Chapter 8.

## 2.2    Testing plan

To meet the objectives of the project, a comprehensive testing plan was developed. To analyse potential scale effects on the mechanical properties of the rock fractures, it was deemed necessary to test samples under at least three different sample sizes. At least one of these sample sizes required to be at large scale, ideally close to the recommended size for in-situ testing of rock fractures according to the ISRM guidelines (700 mm × 700 mm × 350 mm) (ISRM 2007). The largest specimen size within the test program was set to 300 mm × 500 mm, although the new machine was designed to accommodate a 400 mm × 600 mm specimen. This was considered acceptable, since the main part of the scale effects on rock fractures have been observed at smaller scales (less than 200 mm) (Bandis 1980) and it is close to the size recommendation for in-situ experiments. The larger size in the machine allows to somewhat scale up the larger size specimens in future projects if this is desired. From a practical point of view to efficiently extract cores from tunnels in future investigations or drilling cores along fractures are estimated to practically be done up to 300–400 mm diameter.

According to the proposed corrections for scale on the peak shear strength for rock fractures (Barton and Bandis 1982), the parameter JRC influences a potential scale effect. This implies that higher roughness has the potential to generate a more pronounced scale effect, more easily identified. Later research (Johansson 2016) has shown that it may rather be the combination of matedness and roughness of the fracture that govern the peak shear strength than its scale. To generate ideal condition for a potential scale effect to be identified, and at the same time being able to investigate the influence from matedness, it was decided that the testing plan included both tensile induced, rough, perfectly mated fractures, and natural less mated fractures.

Since the testing conditions needed to be representative for the conditions at the repository depth, the test program contains shear tests on natural fractures under CNS conditions. To investigate the influence from dilation on the shear strength under CNS conditions further motivated the incorporation of tensile induced, rough fractures in the testing programme, since rougher fractures implies higher dilation and thus would expect to increase the shear strength under CNS conditions. For comparative purposes, it was also decided that the testing plan should include direct shear tests under CNL conditions as well. Results from CNL tests have been extensively studied in the last decades and can therefore be used as a reference and a baseline for the results from the CNS tests. All CNL test were performed under a normal stress of 5 MPa and all CNS tests were performed under an initial normal stress of 5 MPa and a constant normal stiffness of 10 MPa/mm. The normal stiffness was estimated based on the elastic properties of the rock mass at Forsmark.

To be able to assess potential scale effects and the variability of the shear strength, it was also considered important to have at least three samples for each fracture size, fracture type and boundary condition. For the smallest sample size, this number was increased to six samples. This implied that the testing plan included 24 tests for the smallest samples (35 mm × 60 mm): 12 under CNS conditions and 12 under CNL conditions. At the intermediate scale (70 mm × 100 mm), the testing plan included 12 tests: 6 under CNS conditions and 6 under CNL conditions. For the large-scale tests (300 mm × 500 mm), the testing plan included 11 tests: 6 under CNS conditions and 4 under CNL conditions. The main reason that the large-scale tests under CNL conditions on natural fractures only included one sample was due to budget constrains in the project. In total, the testing plan included 46 specimens (Table 2-1). The designation of the specimens in the table is explained as follows: N and TI designates natural and tensile-induced rock fractures, respectively. S, M and L designates small, medium, and large-size specimens, while CNS and CNL designates the boundary condition used in the tests. The term "*number*" is the numbering of the specimen in that series.

**Table 2-1. Summary of the direct shear testing program on rock fractures comprising forty-six specimens where the CNL tests were tested under a constant normal stress of 5 MPa and the CNS test were tested with an initial normal stress of 5 MPa.**

| Fracture size [mm × mm] | Fracture type | Boundary condition | Number of specimens | Designation |
|---|---|---|---|---|
| 35 × 60 | Natural | CNS | 6 | N*number*-S- CNS |
| | Tensile induced | CNS | 6 | TI*number*-S- CNS |
| | Natural | CNL | 6 | N*number*-S- CNL |
| | Tensile induced | CNL | 6 | TI*number*-S- CNL |
| 70 × 100 | Natural | CNS | 3 | N*number*-M- CNS |
| | Tensile induced | CNS | 3 | TI*number*-M- CNS |
| | Natural | CNL | 6* | N*number*-M- CNL |
| | Tensile induced | CNL | 3 | TI*number*-M- CNL |
| 300 × 500 | Natural | CNS | 3 | N*number*-L- CNS |
| | Tensile induced | CNS | 3 | TI*number*-L- CNS |
| | Natural | CNL | 1 | N*number*-L- CNL |
| | Tensile induced | CNL | 3 | TI*number*-L- CNL |

*) 6 rock fractures have been tested under the CNL boundary condition, however, only three have been tested at 5 MPa initial normal stress. Specimen N2 were tested at 2 MPa, specimen N3 at 1 MPa, and specimen N4 at 10 MPa. So, in total 49 rock fractures have been tested, and 46 of them under 5 MPa initial normal stress.

One of the objectives of the project was to investigate if replicas were suitable to use for parameter investigations of the mechanical properties of rock fractures. To meet this objective, it was also decided to include replicas in the test program. These tests were performed at the specimen size 70 mm × 100 mm under both CNL and CNS conditions.

The most difficult fractures to replicate are tensile induced fractures, since they are very rough at microscale and have a small aperture. These fractures therefore are suitable to use to investigate the effectiveness of a developed replication process for this objective. To include tensile induced fractures for the testing program with respect to the replication of fractures is therefore motivated. Two different types of replicas were therefore used, natural match and perfect match. Natural match implied that two silicone moulds were manufactured, one for the upper part and one for the lower part of the rock fracture specimen, required to replicate the original joint matching. By casting one upper and one lower part of the replica from two different silicone moulds, a more "natural" (less mated) match was generated. The perfect match implied that a silicone mould was generated by the lower part of the of fracture surface, while the upper replica fracture surface was created as a negative imprint of the lower fracture surface. By doing so, a perfect match was obtained between the lower and the upper parts of the replica. For the natural match replicas, 6 specimens were included in the testing plan for CNL conditions. For the perfect match specimens, 3 specimens were included in the testing plan for CNL conditions and 6 specimens for the CNS conditions. In total, 15 specimens were included in the testing plan for replicas, see Table 2-2. The designation of the specimens in the table is explained as follows: RNM and RPM designates replicas natural match and replicas perfect match, respectively. N1 refer to the rock specimen used to create the replica. CNL and CNS designates the boundary condition used in the tests, while the term "*number*" is the numbering of the specimen in that series.

**Table 2-2. Summary of the direct shear testing program on replicas comprising fifteen specimens he CNL tests were tested under a constant normal stress of 5 MPa and the CNS test were tested with an initial normal stress of 5 MPa.**

| Replica size [mm × mm] | Replica type | Boundary condition | Number of specimens | Designation |
|---|---|---|---|---|
| 70 × 100 | Natural match | CNL | 6 | RNM-N1-CNL-*number* |
| | Perfect match | CNL | 3 | RPM-N1-CNL-*number* |
| | Perfect match | CNS | 6 | RPM-N1-CNS-*number* |

# 3 Sample description and preparation

This section starts with a general description of the materials: granite rock and concrete Ducorit®D4 employed for specimen preparation. Then, the process of rock specimen preparation, from quarry to manageable samples ready to be used in tests for characterisation purposes (direct shear tests on rock fractures, and rock material characterisation tests) is presented. This description aims to provide traceability of each specimen's orientation through all steps back to the quarry. This traceability also enables that all samples are tested in the same shear direction. The section is complemented with a description of the manufacturing process of the replica specimens from the original rock ones. Finally, a brief description of the steel specimens prepared for calibration and determination of normal stiffnesses of the shear testing systems is included.

The rock sampling and specimen manufacturing are further described in Jacobsson et al. (2024c), the development of replica specimens in Flansbjer et al. (2024) and the operations for fixating the specimens in specimen holders for mechanical testing in Jacobsson et al. (2024a, b).

## 3.1 General description of materials

### 3.1.1 Granite material

The granite material was taken from a quarry in Flivik located in Sweden. The Flivik quarry is located approximately 11 km north of Äspö and was chosen as a suitable candidate for delivering the large stone blocks needed for the tests, but still capable of acting as analogues to other "granitic" rock-types found in the Forsmark area (granite to quartz-monzodiorite and quartz-monzonite to quartz-diorite). Although differing in mineral composition and texture (such as grain-size and lower quartz content), they also belong to the Transcandinavian Igneous Belt TIB-1 suite of plutonic rocks emplaced in the period 1.81–1.76 Ga, and thus in large share post-emplacement tectonic history, both at large-scale (such as movement of entire plates) as well as at local scale (glaciation and de-glaciation). Shallow located granites usually have induced microcraks with preferred orientations in orthogonal planes due to its geological history (Nadan & Engelder, 2009). This means that the physical properties tend to be orthotropic despite its isotropic grain structure. Moreover, this rock type, described as a medium-grained granite (Figure 3-1a), is considered to have high strength, both in compression and tension. The directions of tensile induced sampling, namely normal to shear direction (N), parallel shear direction (P1) and perpendicular shear direction (P2), are indicated in Figure 3-1b.
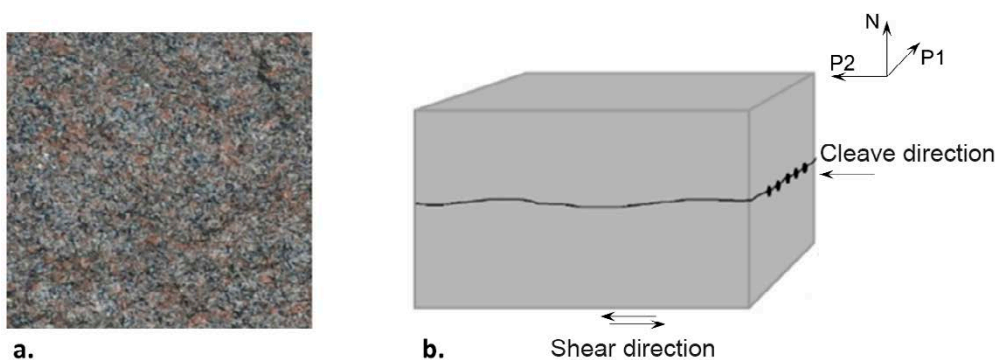


*Figure 3-1.* *Photo of the medium-grained granite (a) and direction of sampling for the blocks (b).*

### 3.1.2 Replica material

An Ultra High-Performance Concrete (UHPC), called Ducorit ® D4 from Densit AS (US) was proposed to be the replica material. It is a ready-mix ($d_{max}$ = 4 mm) product with self-compacting properties. Ducorit ® D4 is reported to have minimal shrinkage and high early-age strength. The material properties specified by the producer is presented in Table 3-1.

Ducorit ® D4 is expected to be more brittle than the granite material applied in this project, i.e. the fracture energy is lower, which is mainly due to the fine-grained structure of the concrete. Furthermore, for this replica material to be suitable, the compressive strength and stiffness of this material should be within the same range as that of the granite material.

**Table 3-1. Summary of material properties for Ducorit ® D4 (Data source: Densit AS).**

| Property | Value | Description |
|---|---|---|
| Compressive strength class | C170/185 | Characteristic strength wrt. 150 mm × 300 mm cyl, 150 mm × 150 mm cubes |
| Uniaxial compressive strength, $f_c$, | 200 MPa | Min. 28 days curing at 20 °C (75 mm × 75 mm cubes) |
| Static modulus of elasticity, $E_c$ | 70 GPa | |
| Dynamic modulus of elasticity, $E_d$ | 88 GPa | |
| Tensile strength, $f_t$ | 10 MPa | |
| Flexural strength, $f_{bt}$ | 23.5 MPa | |
| Poisson's ratio, $v$ | 0.19 | |
| Density, $\rho$ | 2 740 kg/m$^3$ | |

At the beginning of the project, both replicas and grouting were performed with the same grout (Ducorit D4). N1-S-CNL to N4-S-CNL specimens were grouted with Ducorit ® D4. Nevertheless, at some point this product was discontinued, so the remaining rock specimens were grouted with Ducorit ® S5, with similar modulus of elasticity (a relevant concern for a grouting material) as Ducorit ® D4.

## 3.2 Initial rock-block preparation

### 3.2.1 Block extraction at the quarry

The process started with the extraction of four blocks from the Flivik quarry (Figure 3-2), which were afterwards subdivided by splitting and cutting at *Emmaboda Granit* stone processing plant. Finally, the specimens were cut to final dimensions at *Söders* stonemasonry in Kinna and at RISE in Borås. The main characteristics and photos of these blocks are presented in Table 3-2.

Figure 3-3 shows a flowchart where the main subdivision of the blocks presented in Table 3-2 and their subsequent naming are illustrated, with the aim that the reader can trace the general nomenclature used in this Section. More detailed information about the block extraction and preparation can be found in Jacobsson et al. (2024a).

***Figure 3-2.*** *Location in the quarry where the blocks were extracted. The red lines show horizontal exfoliation fractures, and the small picture on the right-hand side of the photo illustrates the height of the wall. The vertical wall having drill holes (blasted surface) corresponds to the hardway plane (one of the granite cleavage orientation planes associated with the genesis of this rock), and the perpendicular plane with smooth wire cut would correspond to the grain plain.*

**Table 3-2. Summarised description of the blocks extracted from the Flivik quarry.**

| Block | Description | Photo |
|---|---|---|
| **Block 19.6** | Mass = 19.6 t<br><br>The block has a thin natural fracture extending 60 % to 100 % in two sides, and 5 % in the other two sides. |  |
| **Block 15.2** | Mass = 15.2 t<br><br>A thin natural fracture is horizontally oriented in the photo but was originally vertically oriented in the rock mass along the *grain* plane. |  |
| **Block 20.7** | Mass = 20.7 t<br><br>A thin natural fracture is horizontally oriented in the photo but was originally vertically oriented in the rock mass along the *grain* plane (this block was not used). |  |
| **Block 17.4** | Mass = 17.4 t<br><br>Reserve block. A thin natural fracture is horizontally oriented in the photo but was originally vertically oriented in the rock mass along the *grain* plane (this block was not used). |  |
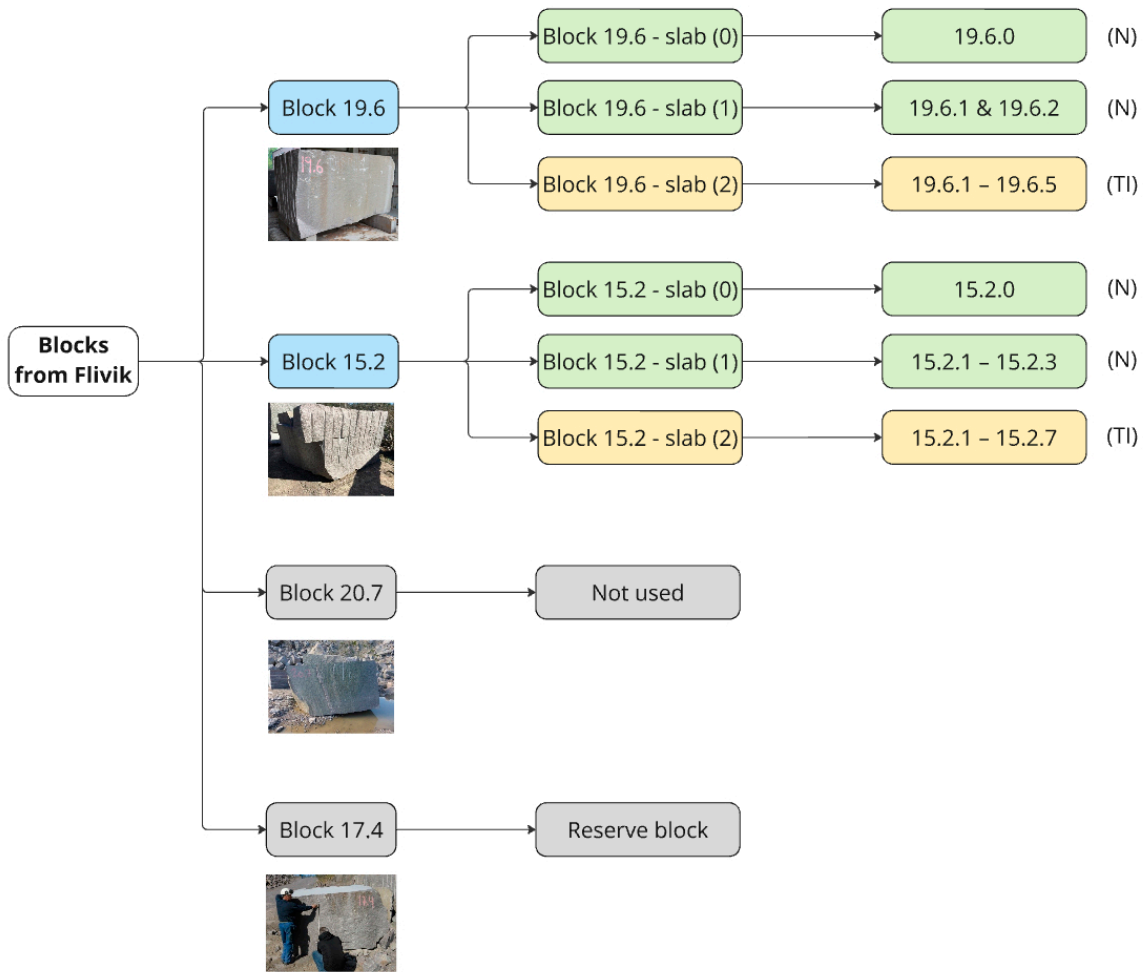
***Figure 3-3.*** *Flowchart illustrating the subdivision of the blocks presented in Table 3-2 and subsequent naming for tracing purposes within this Section.*

### 3.2.2 Block subdivision at the stone masonry

The granite block processing executed at *Emmaboda Granit* stone processing plant is presented herein. Blocks 19.6 and 15.2 (Table 3-2) were further subdivided and selected subordinate blocks were further split to create tensile induced (TI) fractures.

The first operation consisted of applying wire cutting to cut off end parts and to subdivide Blocks 19.6 and 15.2. Four individual cuts were made on Block 19.6, and six individual wire-cuts were made on Block 15.2. These operations are illustrated both in Figure 3-4 and Figure 3-8. Block 20.7 was not used since a fracture opened during handling of the block in the quarry. Block 17.4 was saved as a reserve block.

### Subdivision and splitting of Block 19.6

The remaining material after the first cutting of Block 19.6 consisted of a large side slab (subsequently denoted 19.6.0) and two more blocks, one containing a natural fracture, denoted as Block 19.6–slab (1), and another one denoted as Block 19.6–slab (2) (Figure 3-4).

Block 19.6–slab (1) was subdivided into two blocks (denoted 19.6.1 (N) and 19.6.2 (N)) (Figure 3-5a), and Block 19.6–slab (2) was subdivided into four blocks with approximate dimensions 1 350 mm × 750 mm × (550–750) mm, which were denoted as Blocks 19.6.1–19.6.4 (TI), and a fifth one corresponding to the bottom part, denoted as 19.6.5 (TI) (Figure 3-5b). A tensile-induced crack was produced afterwards in Block 19.6.1 (TI) to Block 19.6.4 (TI), in a similar way as shown by Figure 3-6 for Block 19.6.2 (TI) (for complete traceability of the orientation for the splitting of the different blocks, see Jacobsson et al. (2024c)). The splitting outcomes for Block 19.6.1 (TI) to Block 19.6.4 (TI) is illustrated by Figure 3-7.



*Figure 3-4.* *Block 19.6. a. Cut 1 (producing a thin side slab, subsequently denoted 19.6.0 (N)) and Cuts 2–4 producing two large slabs (Block 19.6–slab (1) and Block 19.6–slab (2)) plus two thin end slabs; b. Side and top view of Block 19.6 after the cuts.*
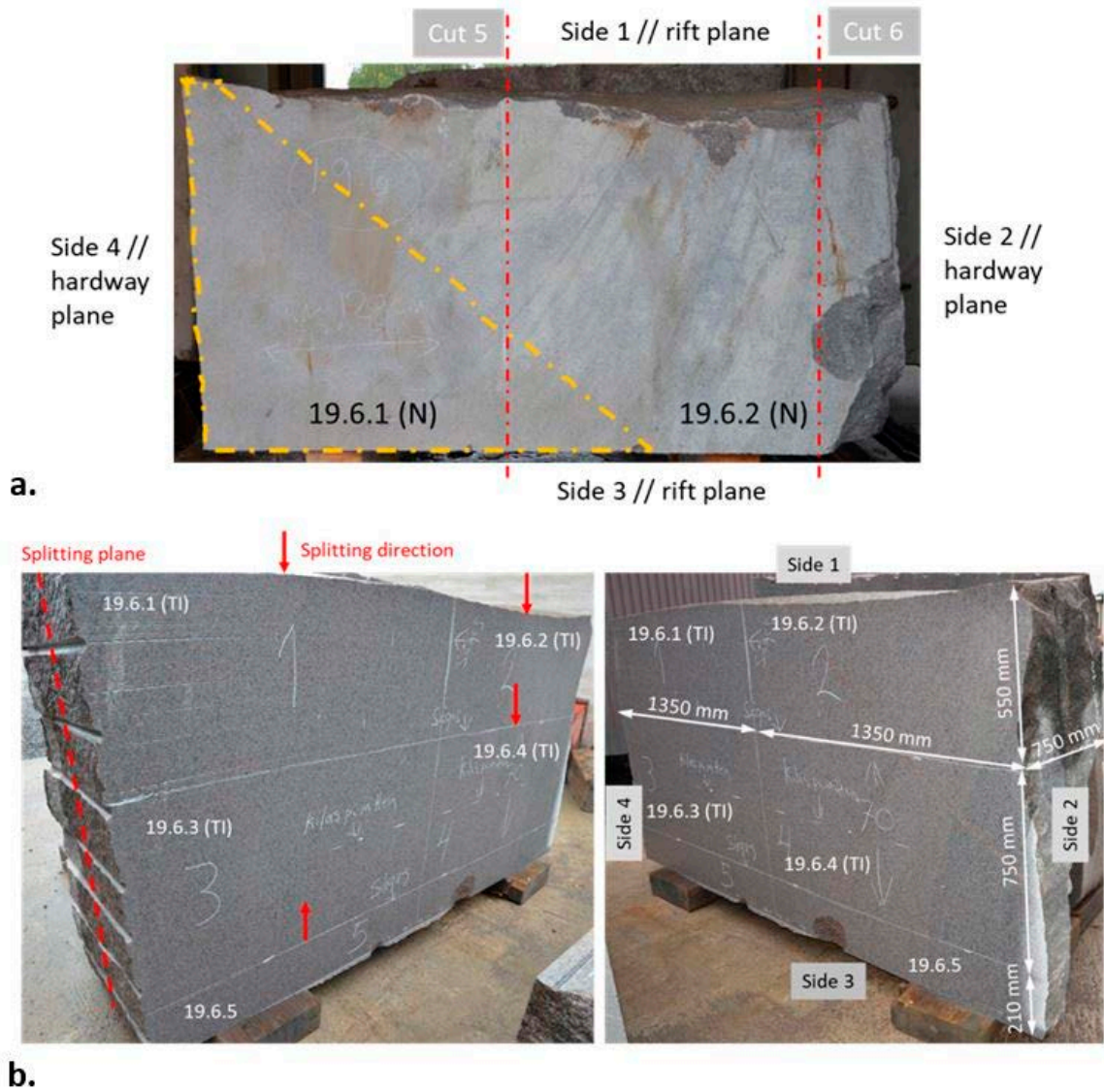
**Figure 3-5.** *a. Subdivision of Block 19.6–slab (1), and b. Block 19.6–slab (2).*



**Figure 3-6.** *Block 19.6.2 (TI) a. Overview of drilling process (17 mm diameter drill, and centre depth of 80 mm); b. Overview of splitting process by means of wedge-driving with a sledgehammer.*
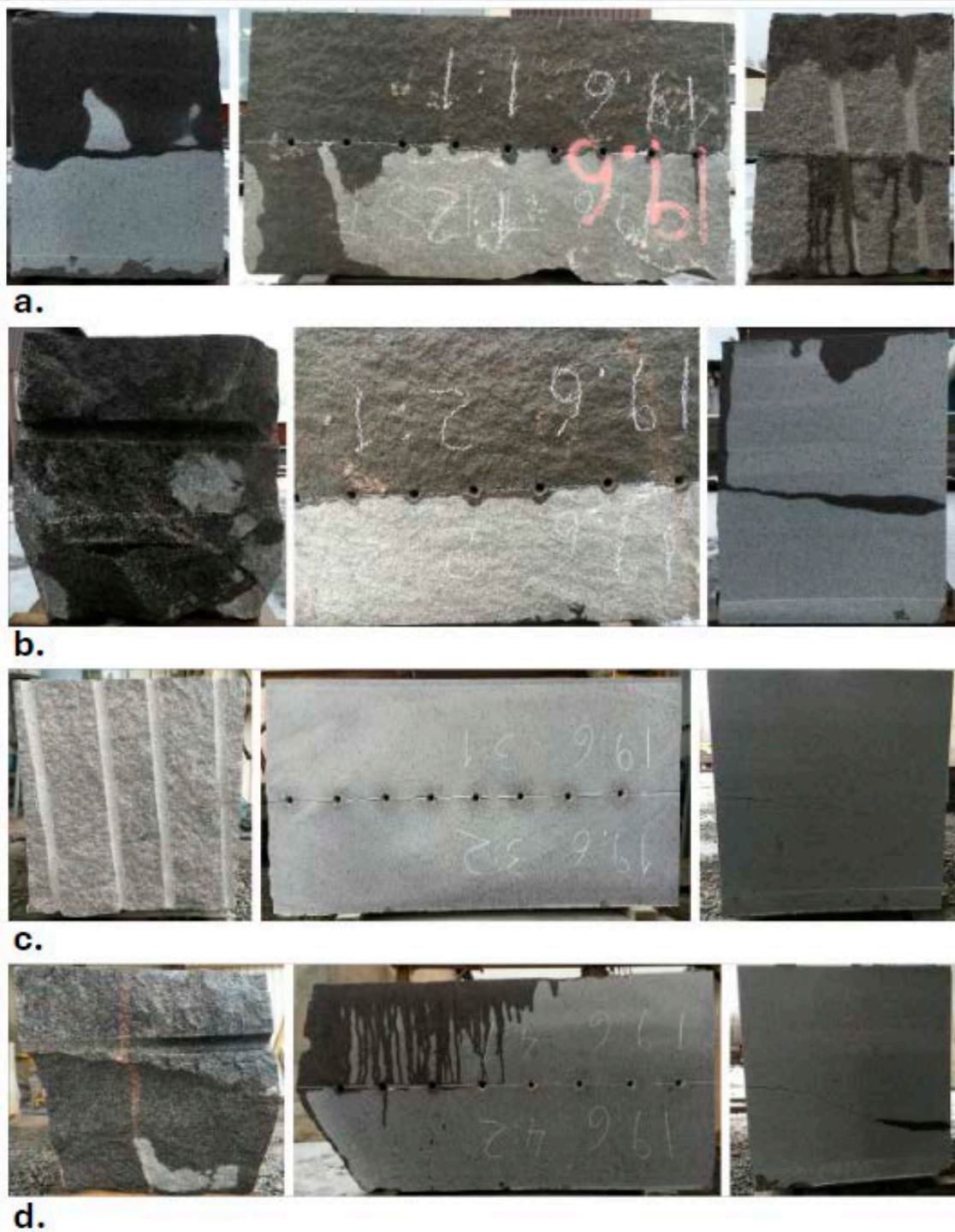
***Figure 3-7.*** *a. Splitting outcome of Block 19.6.1 (TI), showing a rather straight crack with an effective TI-fracture area of 1 300 × 480 mm; b. Splitting outcome of Block 19.6.2 (TI), with a rather straight crack with an effective TI-fracture area of 1 100 × 490 mm; c. Splitting outcome of Block 19.6.3 (TI), and d. Splitting outcome of Block 19.6.4 (TI). The crack propagation took longer for this compared to the others, with an effective TI-fracture area of 1 100 × 600 mm.*

### Subdivision and splitting of Block 15.2

With regard to Block 15.2, the remaining material after the first cutting of this block consisted of a large side slab, subsequently denoted as Block 15.2.0 (N) and containing part of a natural fracture, and two other slabs: one containing the natural fracture plane, denoted as Block 15.2–slab (1) and another one with no fracture (intact rock), named Block 15.2–slab (2), respectively. In addition, there was also surplus material containing a natural fracture (Figure 3-8).
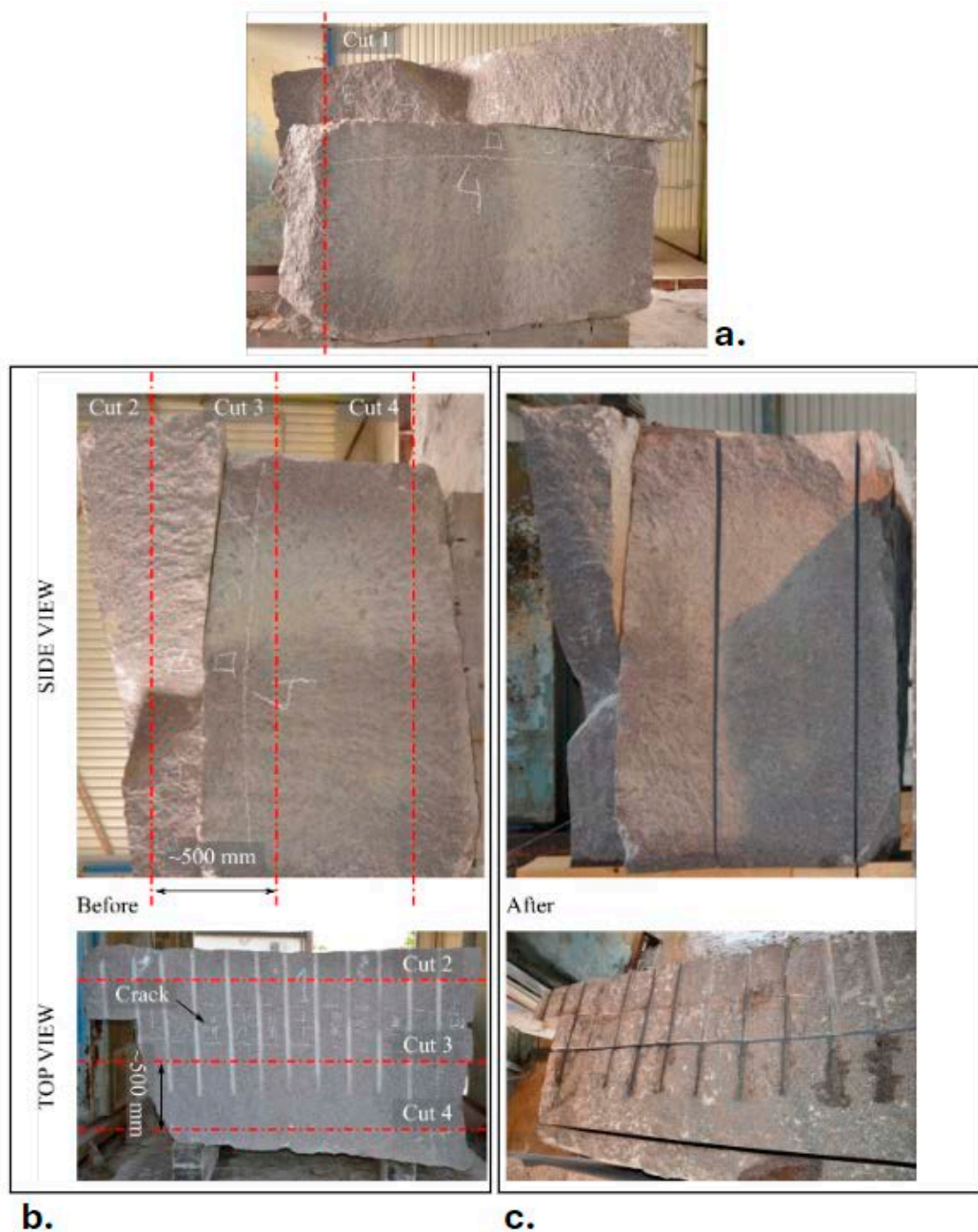


*Figure 3-8.* *Block 15.2: a. Cut 1 (producing Block 15.2.0 (N)); b. Cuts 2, 3 and 4 (side and top view) producing two large slabs – Block 15.2–slab (1) from Cuts 2 and 3, Block 15.2–slab (2) from Cuts 3 and 4, plus two thin end slabs; c. Side and top view of Block 15.2 after the cuts.*

After the first cuttings on Block 15.2, three blocks denoted Block 15.2.1 (N) to Block 15.2.3 (N) were extracted from Block 15.2–slab (1) (Figure 3-9a). From Block 15.2–slab (2), six blocks with varying dimensions from 500–800 mm × 400 mm and denoted as Block 15.2.1 (TI) to Block 15.2.6 (TI), were cut as shown in Figure 3-9b. The remaining part of the Block 15.2–slab (2) was denoted as Block 15.2.7.
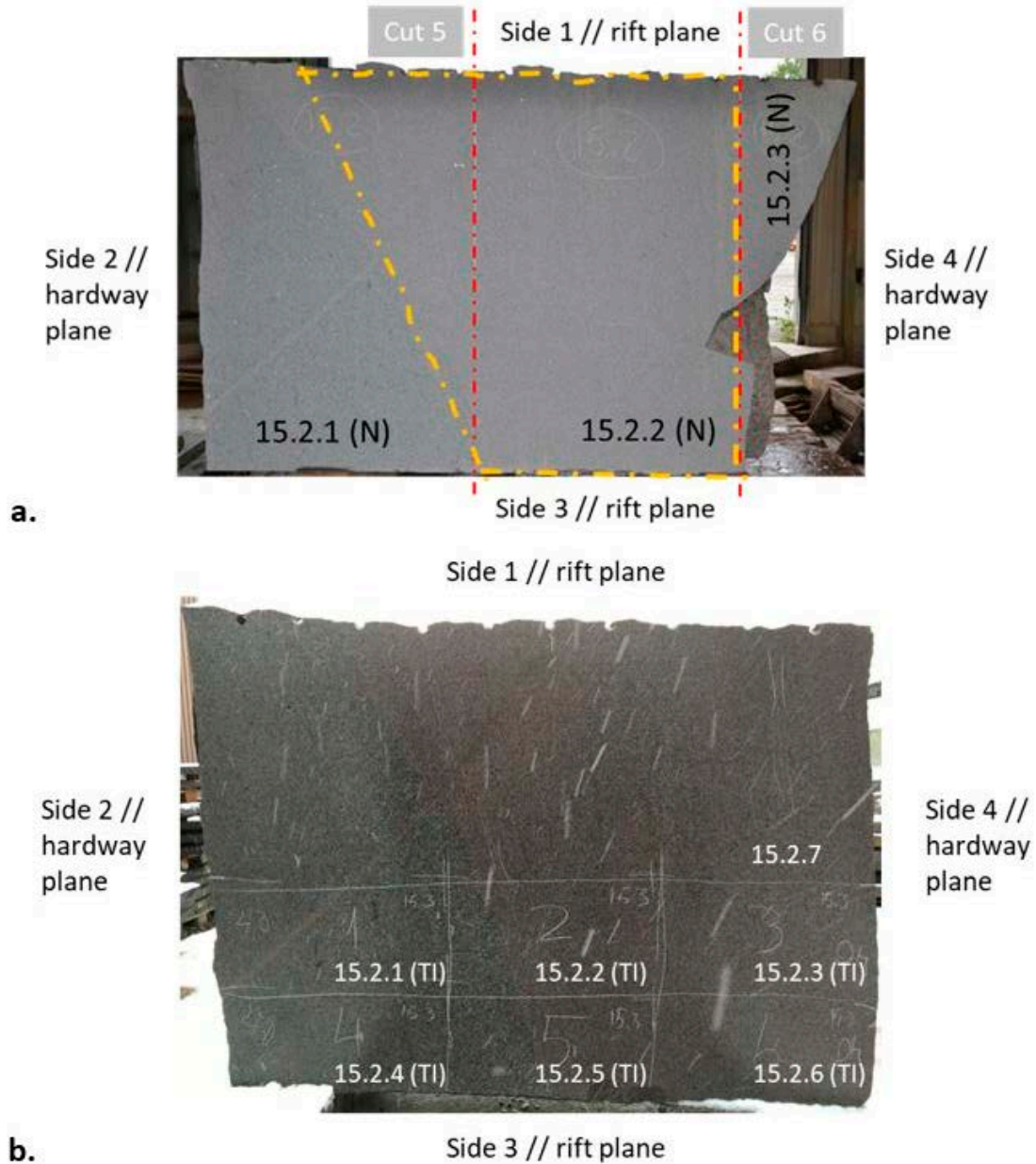


**Figure 3-9.** *a. Subdivision of Block 15.2–slab (1) into Block 15.2.1 (N) to Block 15.2.3 (N), and b. Subdivision of Block 15.2–slab (2) into Block 15.2.7 and Block 15.2.1 (TI) to Block 15.2.6 (TI). The suffix "(TI)" indicates that they will be subsequently split.*

## 3.3 Rock fracture specimens

Two sets of granite blocks were shipped from *Emmaboda Granit* stonemasonry to *Söders stonemasonry* to manufacture manageable test specimens. The first set contained granite blocks with natural fractures and the second set with tensile induced fractures.

From the granite blocks with natural fractures, large specimens (300 mm × 500 mm × 350 mm) for shear testing were produced. In addition, Block 15.2.0 of size 150 mm × 300 mm × 2 000 mm and containing a natural fracture was shipped to RISE's facilities in Borås (Sweden) for further processing of medium-sized specimens for shear testing, namely N1- to N4-M-CNL, N6- and N-7-M-CNL, N5-M-CNS, and N8- and N9-M-CNS (70 mm × 100 mm × 100 mm).

From the granite blocks with tensile induced fractures, large specimens (300 mm × 500 mm × 350 mm) for shear testing were cut (shear direction parallel to the 500 mm side). The saw cut planes were determined by visual inspection followed by marking directly on the granite blocks. Moreover, a slab (150 mm × 300 mm × 600 mm) was cut and shipped to RISE's facilities for further processing of medium-sized specimens for shear testing, namely TI1-CNL to TI4-CNL and TI5-CNS (70 mm × 100 mm × 100 mm).

### 3.3.1 Large-size specimens

During sawing of the large specimens (300 mm × 500 mm × 350 mm), the fractures were held closed, maintaining the upper and the lower parts forming the fracture in their original relative position by using steel belts (Figure 3-10a) and clamps (Figure 3-10b). After cutting, the specimens were fixed also with steel belts and pieces of wood with screw fractures to uphold the original position of the fractures during transport (Figure 3-11).

The rock specimens were measured and cast in parallelepipedic specimen holders during the preparation step. The mass of each rock specimen was about 150 kg. Consequently, the handling of the specimens and the specimen cast in holders were made using a lifting device. The specimen length and width were measured by a steel scale to the nearest millimetre.

The specimens were cast in steel holders using a high strength cement (Ducorit ® S5 Densit) in order to avoid fracturing of the cement during shearing and to provide a high stiffness. The specimen was first placed with the fracture centred and aligned with the machine shear plane. The specimen was subsequently grouted in two steps after it became ready for testing. The gap between the upper and lower specimen holder was 40 mm. All the specimen preparation steps are described in Table 3-3.

**Table 3-3. Activities during large-size specimen preparation.**

| Step | Activity |
| --- | --- |
| 0 | Measure the specimen dimensions using a steel scale |
| 1 | Centre the fracture by tuning the position of the specimen in the lower holder |
| 2 | Cast the lower part of the specimen and let the cement cure for minimum 14 days |
| 3 | Put spacers (black) and material for holding the space (light rose) preventing to grout the centre part (Figure 3-12) |
| 4 | Fixate the upper holder in correct position using the guiding system and cast the upper specimen holder and let the cement cure for minimum 14 days |
| 5 | Remove the spacer material (light rose) |
| 6 | Open the fracture (make access for geometry scanning of the fracture surfaces) |
| 7 | Take digital photos of each specimen |
| 8 | Add a speckle pattern (*) to the areas where optical measurements will be done |
| 9 | Add holders for AE-measurement sensors (results are not included in this report) |
| 10 | Scan the fracture surfaces (Section 4.3) |

(*) The speckle pattern is used for digital image correlation analysis, see Section 5.1.2.

*Figure 3-10. Photos showing how the fractures were kept closed during cutting using steel belts (a, b) and clamps (c).*



*Figure 3-11. Photo of the 300 mm × 500 mm × 350 mm specimens with natural cracks, fixed with steel belts and pieces of wood with screw fractures to maintain the fractures in original position during transportation.*

The different steps during grouting (steps 1–5) are illustrated in Figure 3-12.

A list of all large-size specimens showing the specimen identification, host block, dimensions, and test date is presented in Table 3-4. The specimens labelled "N" have natural fractures and the specimens labelled "TI" have tensile-induced fractures.

**Table 3-4. List of large-size rock specimens, with the host block from which they were obtained and main dimensions (length and width).**

| Specimen ID | Host block | Specimen designation | Length (mm) | Width (mm) | Area (mm²) | Test date (YY-MM-DD) |
|---|---|---|---|---|---|---|
| TI1-L-CNL | 19.6.2 (TI) | 19.6.2.2 | 483 | 301 | 145 383 | 21-05-04 |
| TI2-L-CNL | 19.6.2 (TI) | 19.6.2.3 | 491 | 302 | 148 282 | 21-05-11 |
| TI3-L-CNL | 19.6.2 (TI) | 19.6.2.1 | 480 | 301 | 144 480 | 21-08-05 |
| N1-L-CNL | 19.6.1 (N) | 19.6.1.2 | 501 | 300 | 150 300 | 21-08-31 |
| TI1-L-CNS | 19.6.3 (TI) | 19.6.3.1 | 501 | 302 | 151 302 | 21-11-16 |
| TI2-L-CNS | 19.6.3 (TI) | 19.6.3.2 | 501 | 302 | 151 302 | 21-11-23 |
| TI3-L-CNS | 19.6.3 (TI) | 19.6.3.3 | 500 | 302 | 151 000 | 22-03-01 |
| N1-L-CNS | 15.2.2 (N) | 15.2.2.4 | 501 | 301 | 150 801 | 22-03-08 |
| N2-L-CNS | 15.2.2 (N) | 15.2.2.3 | 501 | 301 | 150 801 | 22-06-16 |
| N3-L-CNS | 15.2.2 (N) | 15.2.2.2 | 501 | 301 | 150 801 | 22-06-28 |

### 3.3.2 Medium- and small-size specimens

The blocks containing the fractured rock were also processed in several stages to obtain the final size of 70 mm × 100 mm (medium-size) and 35 mm × 60 mm (small-size), yielding two type of undisturbed fracture sets: tight natural fractures with small weathering and infilling material, and tensile induced, fresh and perfectly mated fractures.

Concerning the medium-size specimen preparation, all rectangular blocks measuring 70 mm × 100 mm × 100 mm with natural fractures were cut out from a slab from Block 15.2. The orientation of the rectangular specimens in relation to the slab from Block 15.2 can be traced from Figure 3-13, where the circle and the arrow mark the same position and direction, respectively. A general (Figure 3-14) and detailed (Figure 3-15) view of the orientation are shown for a medium-size specimen.
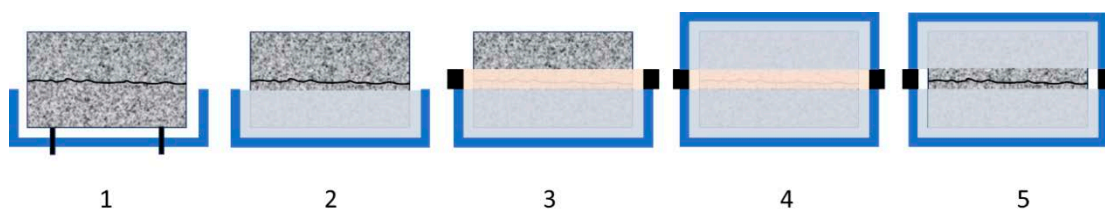


***Figure 3-12.*** *Steps 1–5 for large-size specimen fixation in holders.*

*Figure 3-13.* *Photos from which the orientation of the rectangular medium-size specimens in relation to the slab from Block 15.2 can be traced, by that the circle and the arrow in the photos marks the same position and direction, respectively.*
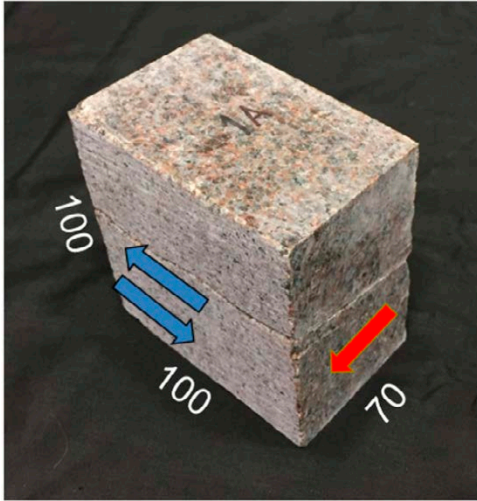
**Figure 3-14.** *N1-M-CNL specimen with the blue arrows indicating the shear direction and a red arrow indicating a certain direction to be tracked in Figure 3-15. The same representation applies for all medium-size natural fractures.*
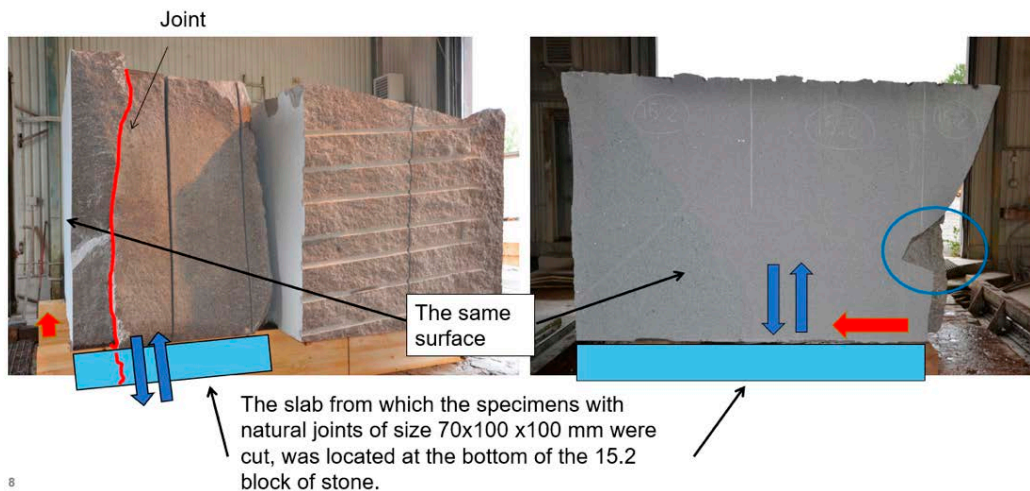


**Figure 3-15.** *The original position of the slab in Figure 3-14 illustrated by the drawn rectangle. The orientation of the blue arrows, indicating the shear direction, and the red arrows, is the same as in Figure 3-14.*

The small-size specimens were obtained from Blocks 15.2.3. Some examples of the Block 15.2.3B and specimens showing natural and tensile-induced fractures are shown in Figure 3-16.

The rock specimens were measured and cast in specimen holders during the preparation step. The specimen length and width were measured using digital callipers. A piece of steel was placed on the rear end with respect to the shear direction for reinforcement and to reduce pieces breaking off the specimen edge due to tensile stress for tests at this scale. An example of these reinforcing pieces of steel is shown in Figure 3-17 for a small-size specimen. Further pictures of these steel pieces can be consulted in Jacobsson et al. (2024b).

The specimens were cast in steel holders using a high strength cement (Ducorit ® S5 Densit, with similar modulus of elasticity as Ducorit ® D4) to avoid fracturing of the cement during shearing and to provide a high stiffness. The specimen was first placed with the fracture centred and aligned with the machine shear plane (Figure 3-18). For those specimens measured with AE, a recess was added in the grout of the lower part of the 70 mm × 100 mm specimens to make space for AE-sensors. The specimen was subsequently grouted in two steps and was then ready for testing (Figure 3-19). The gap between the upper and lower specimen holder was 10 mm. All the specimen preparation steps are described in Table 3-5.
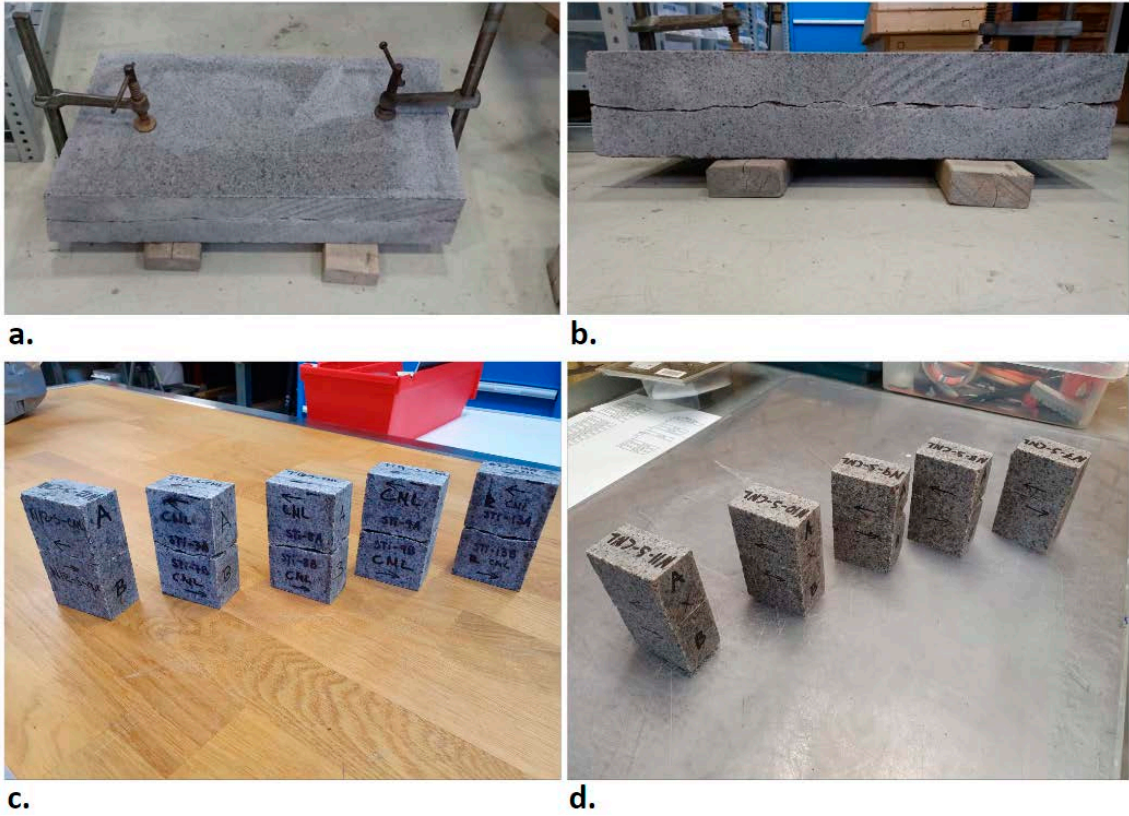
*Figure 3-16.* *a.–b. Two views of 15.2.3b block with a tensile-induced fracture from which some small-size specimens were obtained; c.–d. Different (tensile-induced and natural fracture) small-size specimens.*
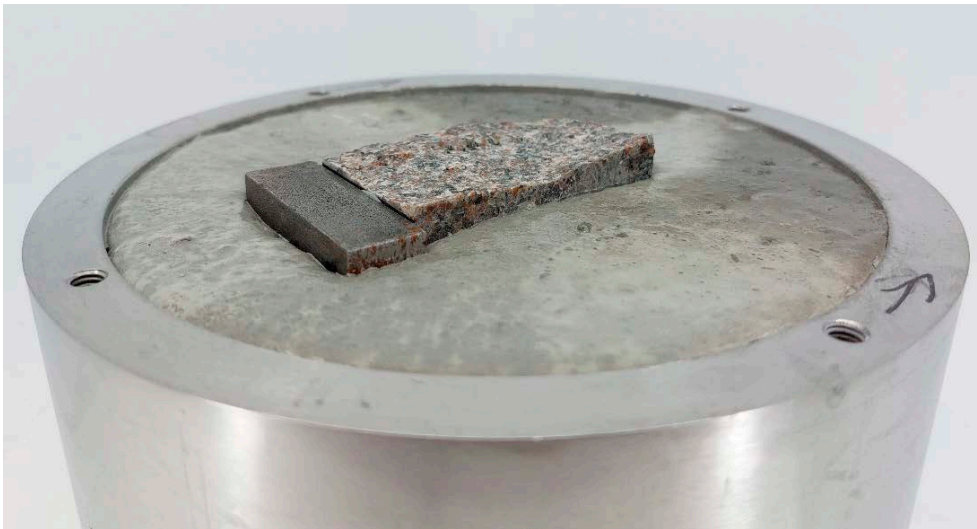


*Figure 3-17.* *Detailed view of the position of a steel piece to avoid breaking off the specimen due to induced tensile stresses when testing.*
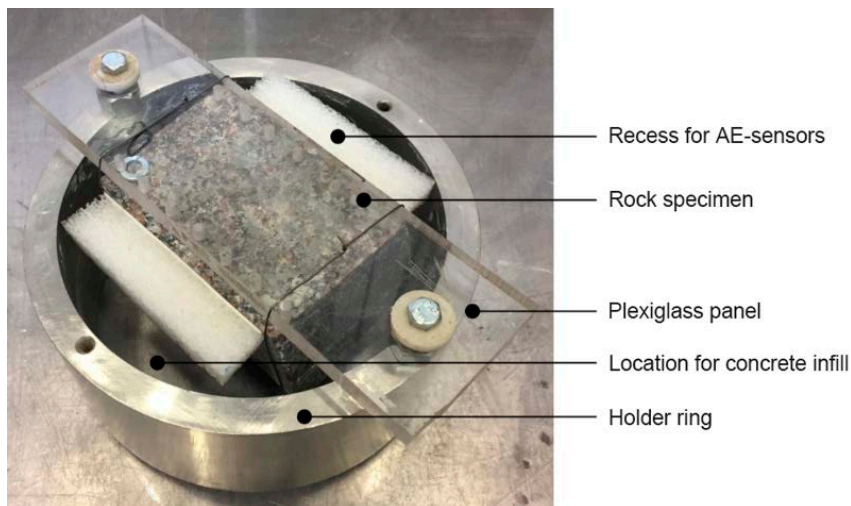
*Figure 3-18. Aligning lower part of the medium-size rock sample to the holder ring.*
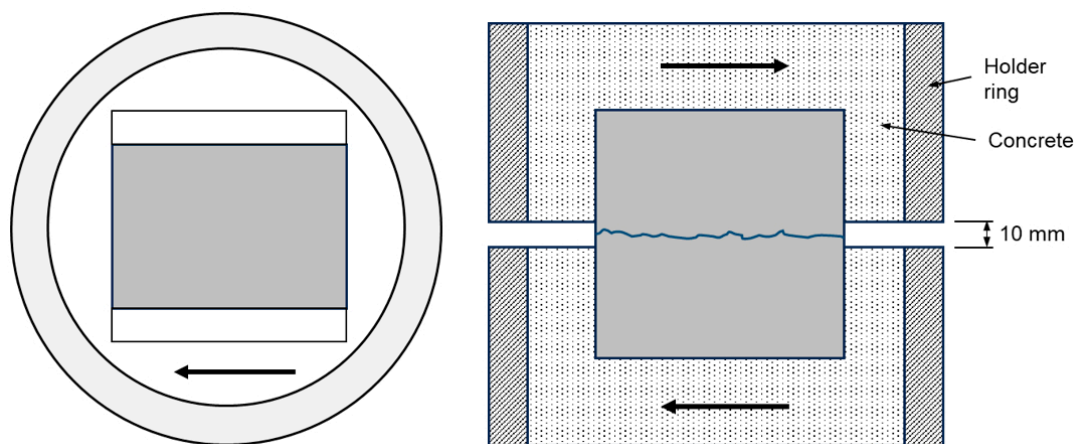


*Figure 3-19. Schematics of a medium-size specimen fixed in holders. Left: Top view of lower part; Right: Sectioned side view of the whole specimen. The arrows illustrate the shear directions.*

**Table 3-5. Activities during medium- and small-size specimen preparation.**

| Step | Activity |
|------|----------|
| 0 | Measure the specimen dimensions using digital callipers |
| 1 | Centre the fracture by tuning the position of the specimen in the lower holder |
| 2 | Cast the lower part of the specimen and let the concrete cure for minimum 14 days |
| 3 | Put spacers to obtain 10 mm cap between the holder rings and material for keeping the space preventing to grout the centre part |
| 4 | Cast the upper specimen holder and let the cement cure for minimum 14 days |
| 5 | Remove the spacer material |
| 6 | Open the fracture (make access for geometry scanning of the fracture surfaces) |
| 7 | Take digital photos of each specimen |
| 8 | Scan the fracture surfaces (Section 4.3) |

A list of all medium- (Table 3-6 and Table 3-7) and small-size (Table 3-8 and Table 3-9) specimens showing the specimen identification, host block, dimensions, and test date is presented. The specimens labelled "N" have natural fractures and the specimens labelled "TI" have tensile induced fractures.

**Table 3-6. List of medium-size specimens (approximate dimensions 70 mm × 100 mm) containing natural fractures (N), listed by specimen's ID, host block and main dimensions.**

| Specimen ID | Host block | Length (mm) | Width (mm) | Area (mm²) | Test date (YY-MM-DD) |
|---|---|---|---|---|---|
| N5-M-CNS | 15.2.0 (N) | 69.6 | 99.2 | 6 904 | 22-02-14 |
| N8-M-CNS | 15.2.0 (N) | 68.4 | 103.9 | 7 407 | 22-02-14 |
| N9-M-CNS | 15.2.0 (N) | 70.2 | 102.7 | 7 210 | 22-02-15 |
| N1-M-CNL | 15.2.0 (N) | 71.1 | 101.7 | 7 231 | 18-03-21 |
| N6-M-CNL | 15.2.0 (N) | 71.5 | 103.6 | 7 407 | 22-02-10 |
| N7-M-CNL | 15.2.0 (N) | 70.5 | 103.1 | 7 269 | 22-02-11 |

**Table 3-7. List of medium-size specimens (approximate dimensions 70 mm × 100 mm) containing tensile-induced fractures (TI), listed by specimen's ID, host block and main dimensions.**

| Specimen ID | Host block | Length (mm) | Width (mm) | Area (mm²) | Test date (YY-MM-DD) |
|---|---|---|---|---|---|
| TI4-M-CNS | 15.2.3 (TI) | 69.6 | 100 | 6 960 | 22-11-14 |
| TI5-M-CNS | 15.2.3 (TI) | 70.6 | 99.9 | 7 053 | 22-02-15 |
| TI6-M-CNS | 15.2.3 (TI) | 69.7 | 100.6 | 7 012 | 22-02-16 |
| TI1-M-CNL | 15.2.3 (TI) | 70.1 | 100.2 | 7 024 | 22-02-11 |
| TI2-M-CNL | 15.2.3 (TI) | 70.2 | 100.5 | 7 055 | 22-11-17 |
| TI3-M-CNL | 15.2.3 (TI) | 69.5 | 100.6 | 6 992 | 22-11-16 |

**Table 3-8. List of small-size specimens (approximate dimensions 35 mm × 60 mm) containing natural fractures (N), listed by specimen's ID, host block and main dimensions.**

| Specimen ID | Host block | Length (mm) | Width (mm) | Area (mm²) | Test date (YY-MM-DD) |
|---|---|---|---|---|---|
| N1-S-CNS | 19.6.1.4 | 35.2 | 61.0 | 2 147 | 23-10-23 |
| N2-S-CNS | 19.6.1.4 | 35.2 | 61.0 | 2 147 | 23-10-24 |
| N3-S-CNS | 19.6.1.4 | 35.2 | 61.4 | 2 161 | 23-10-24 |
| N4-S-CNS | 19.6.1.4 | 35.2 | 60.4 | 2 126 | 23-10-25 |
| N5-S-CNS | 19.6.1.4 | 35.3 | 60.7 | 2 143 | 23-10-26 |
| N6-S-CNS | 19.6.1.4 | 35.5 | 60.5 | 2 148 | 23-10-26 |
| N7-S-CNL | 19.6.1.4 | 35.7 | 60.9 | 2 174 | 23-05-30 |
| N8-S-CNL | 19.6.1.4 | 35.6 | 60.9 | 2 168 | 23-05-30 |
| N9-S-CNL | 19.6.1.4 | 35.6 | 60.2 | 2 143 | 23-05-31 |
| N10-S-CNL | 19.6.1.4 | 35.6 | 60.8 | 2 164 | 23-06-02 |
| N11-S-CNL | 19.6.1.4 | 35.4 | 61.2 | 2 166 | 23-06-07 |
| N12-S-CNL | 19.6.1.4 | 35.5 | 60.8 | 2 158 | 23-06-07 |

**Table 3-9. List of small-size specimens (approximate dimensions 35 mm × 60 mm) containing tensile-induced fractures (TI), listed by specimen's ID, host block and main dimensions.**

| Specimen ID | Host block | Length (mm) | Width (mm) | Area (mm²) | Test date (YY-MM-DD) |
|---|---|---|---|---|---|
| TI1-S-CNS | 15.2.3 | 35.2 | 58.5 | 2 059 | 23-06-29 |
| TI2-S-CNS | 15.2.3 | 35.2 | 58.3 | 2 052 | 23-10-17 |
| TI3-S-CNS | 15.2.3 | 35.2 | 58.4 | 2 056 | 23-10-18 |
| TI4-S-CNS | 15.2.3 | 35.2 | 58.4 | 2 056 | 23-10-18 |
| TI5-S-CNS | 15.2.3 | 35.2 | 58.3 | 2 052 | 23-10-19 |
| TI6-S-CNS | 15.2.3 | 35.3 | 58.6 | 2 069 | 23-10-23 |
| TI7-S-CNL | 15.2.3 | 35.2 | 58.9 | 2 073 | 23-06-08 |
| TI8-S-CNL | 15.2.3 | 35.2 | 60.5 | 2 130 | 23-06-08 |
| TI9-S-CNL | 15.2.3 | 35.4 | 60.5 | 2 142 | 23-06-09 |
| TI11-S-CNL | 15.2.3 | 35.4 | 60.3 | 2 135 | 23-10-16 |
| TI12-S-CNL | 15.2.3 | 35.4 | 60.2 | 2 131 | 23-10-17 |
| TI13-S-CNL | 15.2.3 | 35.2 | 60.2 | 2 119 | 23-06-09 |

## 3.4 Intact rock material specimens

Standard material strength testing and deformability characterisation of the granite was made through uniaxial compressive strength (UCS) tests, direct tensile strength (DTS) tests and indirect tensile strength (ITS) through Brazilian tests (see Chapter 4). All specimens for this type of material characterisation were taken from Block 15.2.2.1. Complementarily, some granite material was prepared for characterisation of the basic frictional behaviour of saw-cut rock surfaces by means of tilt tests.

### 3.4.1 Material for strength and deformability characterisation

The material for preparing the specimens intended for strength and deformability characterisation was oriented in three directions in relation to the shear direction of the fractures of Blocks 15.2.2.2–4:

- N direction: normal to the plane of the fracture (normal to the *grain* plane).

- P1 direction: in the plane of the fracture and parallel to the shear direction of Blocks 15.2.2.2–4 (normal to the *rift* plane).

- P2 direction: in the plane of the fracture, but perpendicular to the shear direction of Blocks 15.2.2.2–4 (normal to the *hardway* plane).

In Table 3-10, a summary of the extracted cores from Block 15.2.2.1 for material characterisation is provided.

**Table 3-10. Cores taken from Block 15.2.2.1B (note that the given dimensions correspond to the core where the specimens for testing were extracted from).**

| Test type | No. of specimens and geometry | Direction | Labels |
|---|---|---|---|
| UCS and DTS | 10 cores (Ø 54 mm, length 160 mm) | N | D54N1–D54N10 |
| | 10 cores (Ø 54 mm, length 200 mm) | P1 | D54P1–D54P10 |
| Brazilian | 4 cores (Ø 54 mm, length 100 mm) | N | BRN1–BRN4 |
| | 3 cores (Ø 54 mm, length 200 mm) | P1 | BRP11–BRP13 |
| | 5 cores (Ø 54 mm, length 120 mm) | P2 | BRP21–BRP25 |

The granite specimens for UCS and DTS tests consisted of 54 mm diameter and 135 mm height cores. The specimens were taken from Block 15.2.2.1B ($200 \times 1\,100 \times$ c. 400 mm) in two directions: parallel to the shear direction (P1) and normal to shear direction (N). These cores were drilled from the block close to each other in each direction, as illustrated in Figure 3-20.

Concerning the Brazilian test specimens, 30 rock specimens were prepared. The specimens were taken from three perpendicular directions in a block, namely parallel to shear direction (P1), perpendicular to shear direction (P2) and normal to shear direction (N), as illustrated in Figure 3-21. The cores were drilled from the block and the specimens were sawn from the cores to get the prescribed dimensions. Parts of the cores with obvious tool marks on the circumference were discarded.

### 3.4.2 Material for basic frictional characterisation

Twelve parallelepipedic slabs ($300 \times 80 \times 70$ mm) were cut from Block 15.2.1.5 and six of them were sent to the University of Vigo (Spain) for performing tilt tests. Since the slab that was cut from Block 15.2.1 was about 600 mm in length, it was subsequently cut into two parts, namely A and B (Figure 3-22 and Figure 3-23), since a length of 300 mm was required for further preparation of the specimens to be used in tilt tests (Figure 3-24).
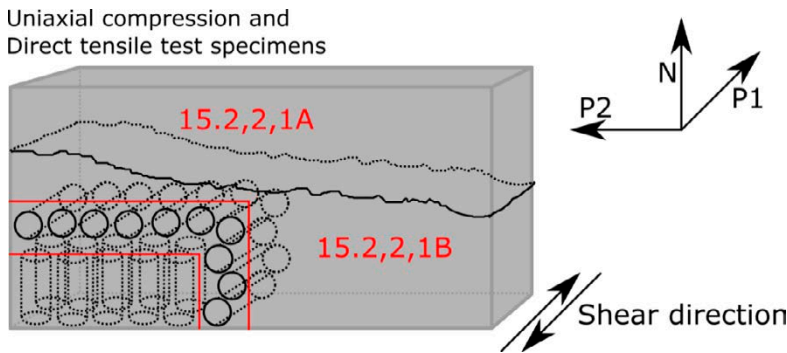


***Figure 3-20.*** *Specimen extraction for UCS and DTS tests from Block 15.2.2.1B.*
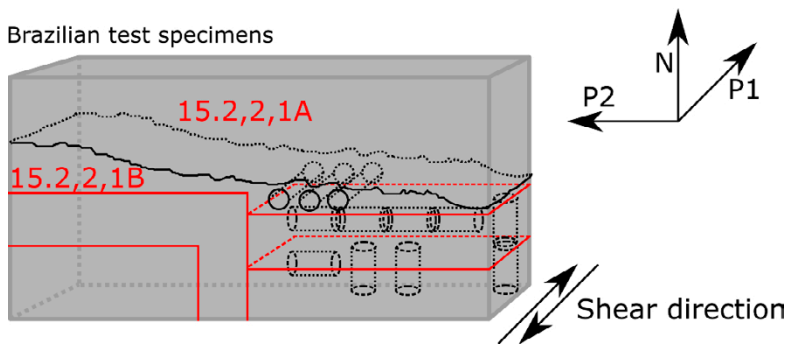


***Figure 3-21.*** *Specimen extraction for Brazilian tests from Block 15.2.2.1B.*

**Figure 3-22.** *Sized slabs from Block 15.2.1.5 (300 mm × 80 mm × 70 mm) categorised as Groups A and B, for further preparation of tilt-test specimens at the University of Vigo (Spain).*
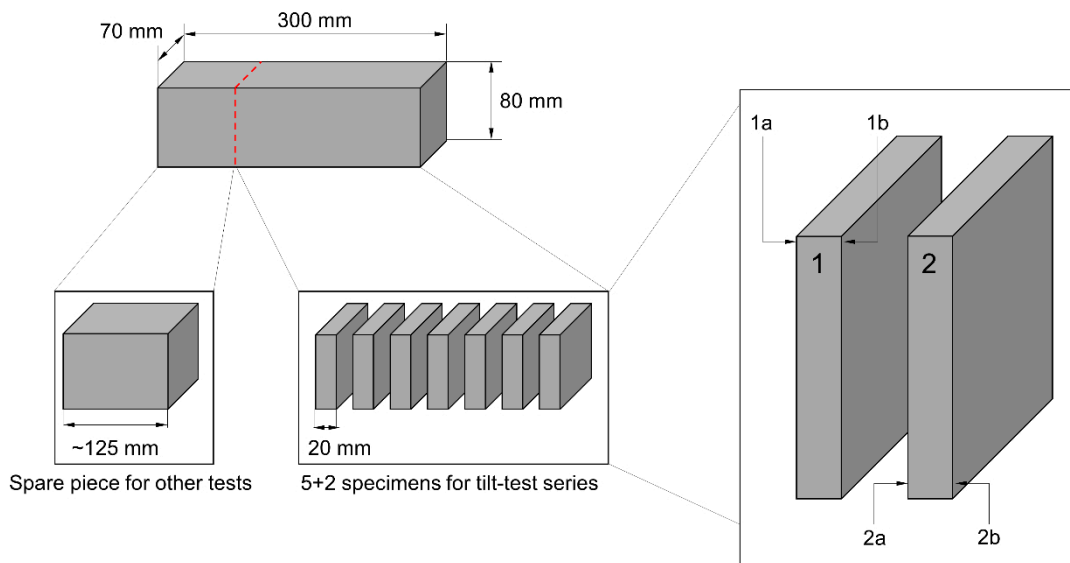


**Figure 3-23.** *Sequence for obtaining tilt-test specimens from rectangular-based slabs.*

**Figure 3-24.** *Granite specimens for tilt-tests.*

## 3.5 Replica material specimens

The mechanical characterisation (strength and deformability) of the replica material was also made through uniaxial compressive strength (UCS) tests, direct tensile strength (DTS) tests and indirect tensile strength (ITS) by means of Brazilian tests. Shrinkage tests were performed on rectangular concrete slabs and, complementarily, some replica material was prepared for characterisation of the basic frictional behaviour of saw-cut concrete surfaces by means of tilt tests.

### 3.5.1 Material for strength and deformability characterisation

Strength and deformability tests for characterising the replica material required the preparation of concrete cylinders, which were initially cast with dimensions of Ø54/200 mm in plastic cylindrical moulds. These cylinders were sawn afterwards to their final length of 135 mm (UCS and DTS tests) or 27 mm (Brazilian tests). The specimens were demoulded and stored in a climate room for 7 days (20 °C, RH 50 %) and then stored in the laboratory until testing. A summary of the prepared replica specimens for these test series (UCS, DTS and ITS) are provided in Table 3-11, Table 3-12 and Table 3-13, respectively. Note that it was necessary to add an additional amount of water, indicated as a percentage, with respect to that recommended by the manufacturer.

**Table 3-11. List of prepared replica material specimens for compression tests (the + sign stands for an amount of water that exceeds the recommended level by the manufacturer).**

| Casting date | Additional water content [%] | Specimen ID | Testing age [days] |
|---|---|---|---|
| 2017-05-31 | + 3−5 | (1-4)-14d | 14 |
| | | (5-8)-21d | 21 |
| | | (9-12)-28d | 28 |
| | | (13-16)-71d | 71 |
| 2017-09-12 | + 3−5 | (17-20)-7d | 7 |
| 2017-12-07 | + 8 | (1-3)-28d | 28 |
| 2018-03-01 | + 13 | (1-3)-28d | 28 |
| 2018-05-07 | + 9 | (1-3)-28d | 28 |

**Table 3-12. List of prepared replica material specimens for direct tensile tests (the + sign stands for an amount of water that exceeds the recommended level by the manufacturer).**

| Casting date | Additional water content [%] | Specimen ID | Number of specimens | Test age [days] |
|---|---|---|---|---|
| 2017-09-12 | + 5 | 2 | 1 | 28 |
| | | 10, 12 | 2 | 59 |
| 2018-02-07 | + 12 | (1-6)-28d | 6 | 28 |

**Table 3-13. List of prepared replica material specimens for Brazilian tests (the + sign stands for an amount of water that exceeds the recommended level by the manufacturer).**

| Casting date | Additional water content [%] | Specimen ID | Number of specimens | Test age [days] |
|---|---|---|---|---|
| 2017-09-12 | + 5 | (1-5)-7d | 5 | 7 |
| | | (6-10)-14d | 5 | 14 |
| | | (11-15)-21d | 5 | 21 |
| | | (16-20)-28d | 5 | 28 |
| | | (21-25)-71d | 5 | 71 |

Concerning the shrinkage test, rectangular-based prismatic specimens (400 mm × 100 mm × 100 mm) were cast with two measurement studs located at the outer ends, as shown in Figure 3-25. The measurement studs are reference points for measuring the change in length of the specimens over time.

All specimens were covered by plastic foil during the first 24 hours of curing. Three specimens were exposed to boundary conditions prescribed by the standard (water and climate room), while two additional specimens were solely placed in a climate room. The second set of specimens are meant to simulate the boundary conditions which are most plausible during the replica production. A detailed account of the boundary conditions and measurements are listed in Table 3-14.



*Figure 3-25. Specimens with end studs for shrinkage measurements.*

**Table 3-14.Shrinkage measurement details.**

| Test method | Number of specimens | Curing conditions | Measurement age | Measurement date |
|---|---|---|---|---|
| Shrinkage ("Water", boundary conditions according to standard) | 3 | 1 day, in the mould at 20 ± 2 °C<br>6 days, in water at 20 ± 2 °C<br><br>In climate room at 20 ± 2 °C and 50 ± 5 % RH | 1<br>7<br>14<br>21<br>28<br>35<br>42<br>49<br>56 | 2017-10-26<br>2017-11-01<br>2017-11-08<br>2017-11-15<br>2017-11-22<br>2017-11-29<br>2017-12-06<br>2017-12-13<br>2017-12-20 |
| Shrinkage ("Climate room", alternative boundary conditions) | 2 | 1 day, in the mould at 20 ± 2 °C<br><br>In climate room at 20 ± 2 °C and 50 ± 5 % RH | 1<br>7<br>14<br>21<br>28<br>35<br>42<br>49<br>56 | 2017-10-26<br>2017-11-01<br>2017-11-08<br>2017-11-15<br>2017-11-22<br>2017-11-29<br>2017-12-06<br>2017-12-13<br>2017-12-20 |

## 3.5.2 Material for basic frictional characterisation

The preparation of tilt-test specimens for the basic frictional characterisation of replica material planar surfaces, was made from four concrete rectangular-based slabs (Figure 3-26) measuring 300 mm × 80 mm × 70 mm each, which were sent to the University of Vigo (Spain). The concrete specimens for tilt-tests were prepared in a similar manner as for the rock specimens (Figure 3-23), and are shown in Figure 3-27.
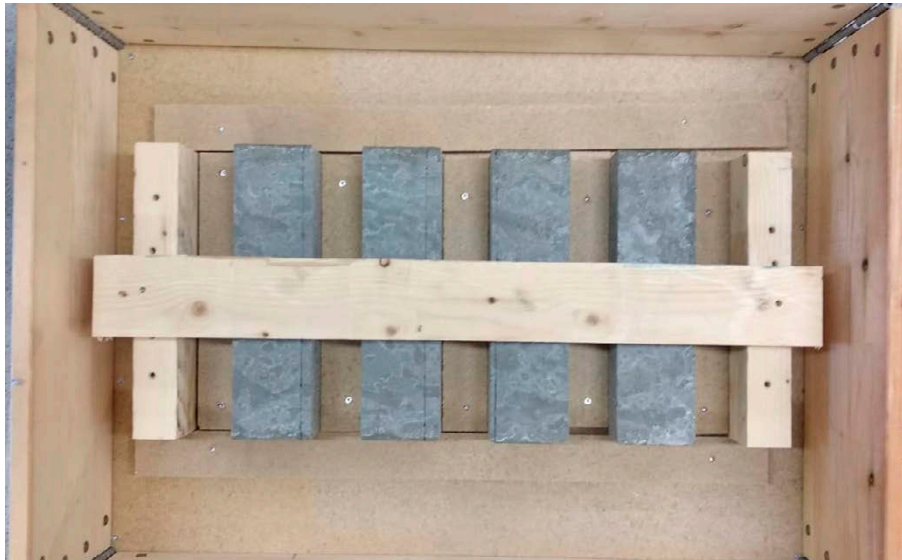


*Figure 3-26. Replica material slabs for preparation of tilt-test specimens.*

**Figure 3-27.** *Concrete specimens for tilt-tests.*

## 3.6 Replica material fracture specimens

In this section, the material and replication method for medium-size rock fracture specimens (70 mm × 100 mm) is summarised. The replication process encompasses the selection of an appropriate rock fracture to be replicated and grouting material together with a silicon product to produce the moulds, a suitable technique, and a verification method. The replication technique followed in this work is the negative surface imprinting, which involves the production of a negative surface imprint of the original rock surface that is then used as a mould surface. A summary of the methodology applied for developing the replicas is shown in Figure 3-28. A detailed description of the manufacturing process can be found in Larsson et al. (2023a) and in Flansbjer et al. (2024).
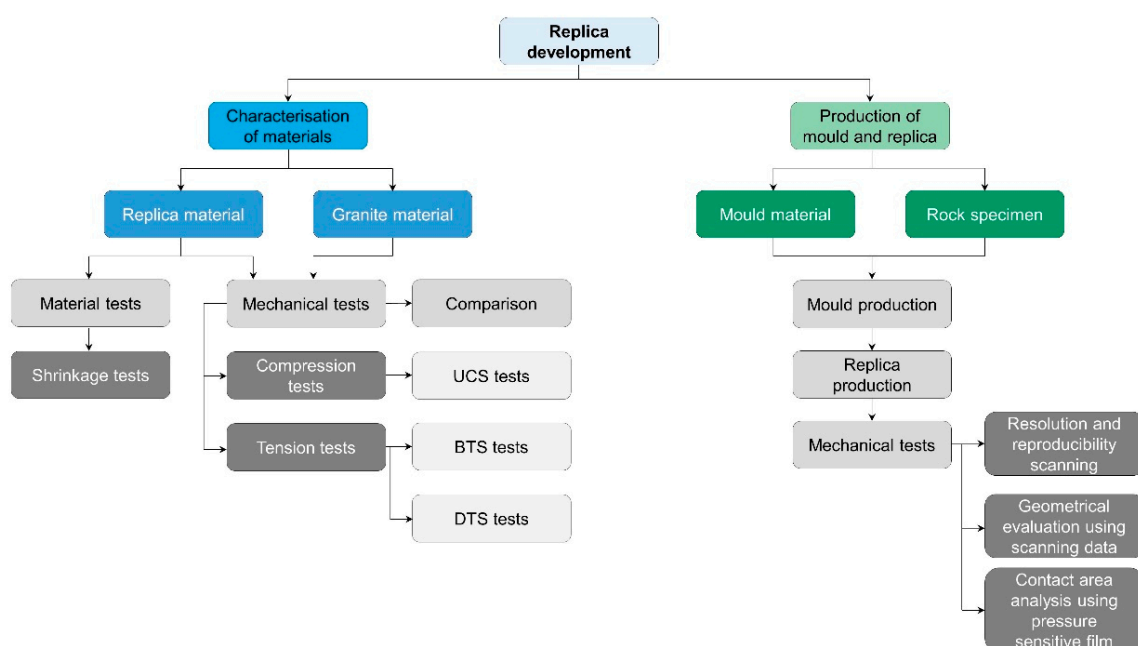


**Figure 3-28.** *Methodology applied in the replica development program.*

### 3.6.1 Materials

*Replicas*

The UHPC, called Ducorit®D4 and manufactured by Densit AS, was proposed to be the replica material. A complete description of this material is already given in Section 3.1.2 (Replica material).

*Grouting*

The same cementitious material used to produce the replicas (Ducorit®D4) was proposed and used as the grouting material. Moreover, a self-levelling hydraulic cement, namely Quik-Rok (Ameristar), was applied to achieve a smooth and even surface at the extremities of the specimens, e.g. as a 5–10 mm layer, (particularly related to ends cast without a plane casting surface). This product is simply mixed with water and formulated to set within 15 min under normal conditions.

*Silicone*

A suggested silicone product for the replica moulds was ELASTOSIL ® M4601 A/B (Wacker Chemie AG). It is a two-component – denoted as Silicone (A) and Hardener (B) – silicone rubber with very good flow properties. It allows for easy and safe handling, as well as room-temperature curing.

### 3.6.2 Manufacturing of replicas

In this section, the specific procedures for the manufacturing of replicas are given. A rock fracture specimen was initially fixed to the specimen holders intended for usage in direct shear tests. Secondly, imprints of the rock fracture surfaces were produced and used as moulds in the casting of subsequent replicas. Two types of replicas were manufactured: naturally mated (requiring the production of casts of upper and lower rock fracture), and fully mated, where the upper replica surface was cast directly as an imprint of the lower one.

*Rock fracture specimen preparation*

A natural granite rock fracture specimen with no infilling material of size $100 \times 70 \times 100$ mm (length × width × height), was fixed to the metal specimen holders with encapsulating grout made of UHPC Ducorit ® D4 from Densit AS. The fracture splits the specimen in two halves of approximately the same height, 50 mm. Before fixation, the lower part was positioned by attaching it with steel wires to a plastic panel fixed to the specimen holder. Spacers were positioned in those areas of the fracture surface required to get the specimen in a fixed position in relation to the flat surface of the panel. This was done with the intention to make the best-fit plane of the fracture surface parallel to the theoretical shear plane, which is parallel to the top surface of the specimen holder. The specimen was adjusted to be centred relative to the specimen holder ring. Vertically, the specimen was adjusted making the best-fit plane of the fracture surface lay 5 mm above the top surface of the specimen holder ring (Figure 3-29a). Approximately 4 kg of Ducorit ® D4 were gradually mixed with 4 dL (deciliter) of water during 10–15 min and then poured to fill the space surrounding the rock fracture specimen. The grout was hardened under standard laboratory conditions covered with plastic foil for approximately 5 days to slow down evaporation.

After hardening, the plastic panel, spacers and steel wires were removed after which the upper rock fracture was placed on top of the lower rock fracture specimen by manual fitting of the fracture surfaces (Figure 3-29b). Then, a spacer ring was mounted separating the lower and the upper specimen holders. The upper specimen holder was mounted on top of the spacer ring. A gap of 10 mm symmetrically distributed about the fracture surface was created by pouring silicone into the space prescribed for the gap between the specimen holders followed by curing for approximately 24 hours. The upper fracture specimen was fixed to the upper specimen holder with Ducorit ® D4 concrete following the same procedure as described for the lower specimen but leaving a 5–10 mm space at the top of the
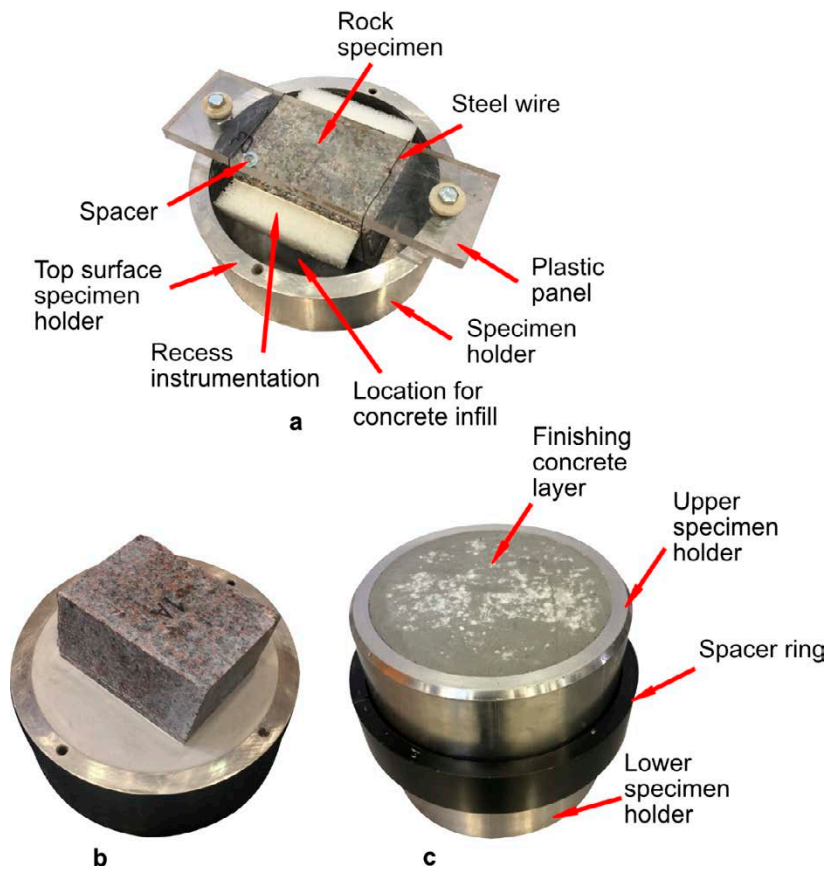
*Figure 3-29.* a. Positioning of the lower rock fracture to the specimen holder before fixation with encapsulating grout; b. Upper part of the rock fracture placed on top of the lower after being fixed by encapsulating grout; c. Upper part of the rock fracture specimen filled with encapsulating grout while placed on the spacer ring. Larsson et al. (2023a)

specimen holder for a surface finishing layer. After hardening of the concrete, a finishing layer of concrete (Quik-Rok ® mixed for 10 minutes, 3.5:1 with water by volume) was poured up to the top of the specimen holder surface followed by curing covered by plastic foil under standard laboratory conditions for about 5 days (Figure 3-29c). After curing, the silicon infill, the spacer ring and tape were removed and the lower and the upper rock fracture specimens were separated to be used for the subsequent manufacturing of replicas.

### *Mould production*

The moulds of the rock fracture surfaces were made of silicone (ELASTOSIL® M4601 A/B from Wacker Chemie AG) mixed in proportions 9:1 (silicone:hardener by weight). As a first step, a release agent was applied on the rock fracture and the grouting surfaces. Then, a thin layer of silicone was applied over the fracture surface and air bubbles removed with a soft paintbrush. After that, an aluminium cover was fixed to the specimen holder containing the rock fracture and silicone poured through the centre hole until the three surrounding holes (risers) were filled up indicating that the whole space has been filled (Figure 3-30a). The silicone was cured for 24 h in standard laboratory conditions. Then, the lid was removed with the negative silicone imprint integrated in the cover (Figure 3-30b). In total, six moulds from the lower rock fracture surface and three from the upper rock fracture surface were manufactured.
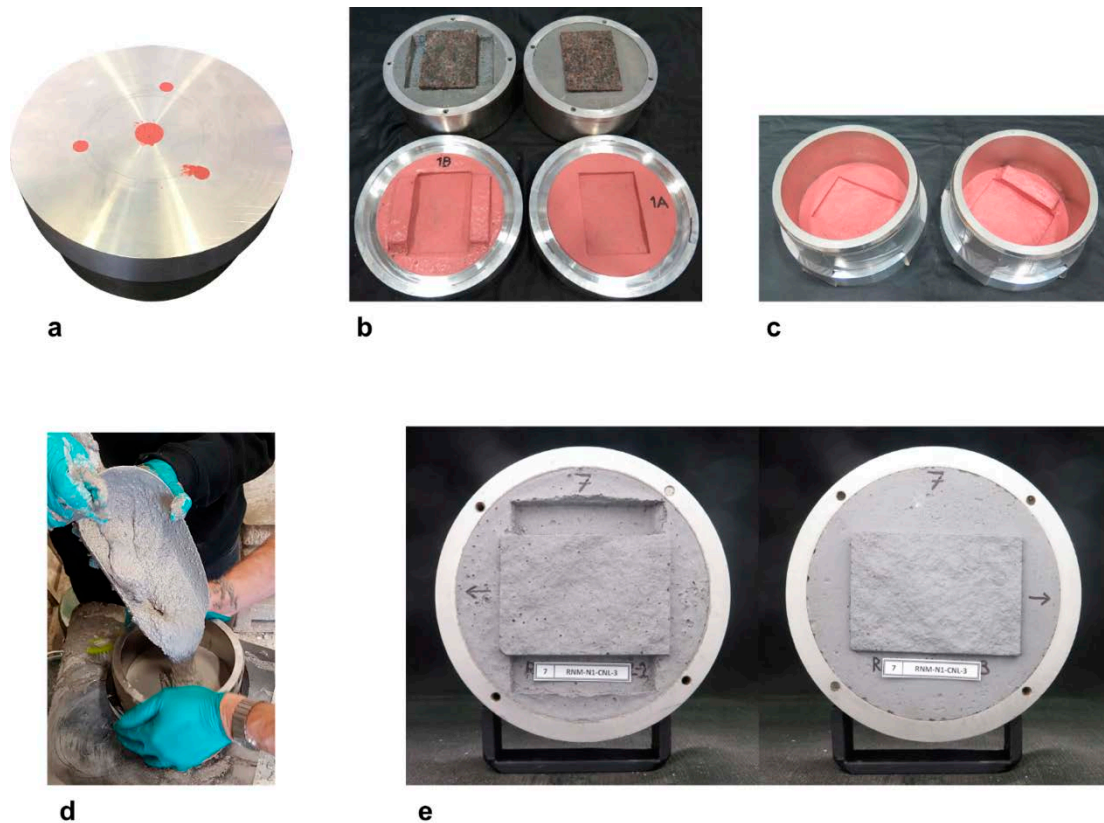
***Figure 3-30.*** *a. Aluminium cover fixed to the specimen holder containing the rock fracture specimen and filled with silicone constituting the mould after curing; b. Silicone moulds integrated in the covers and the corresponding rock fracture specimens; c. Specimen holders fit to aluminium covers containing silicone moulds; d. Casting of a replica fracture specimen; e. Lower rock fracture replica (left) and upper rock fracture replica (right). Larsson et al. (2023a)*

### Naturally mated replicas

A specimen holder was fitted to the aluminium cover containing the silicone mould (Figure 3-30c). Ducorit®D4 concrete was mixed for 2 min in a pan-mixer and then water was added with mixing proportions 1:0.079 (cement : water by mass). The concrete was mixed for 10–15 min until appropriate flowability was obtained with the addition of 3–5 % water when required. The specimen holder containing the mould was placed on a vibration table, and the concrete was poured into the specimen holder leaving 10 mm unfilled from the top of the holder (Figure 3-30d). The top of the specimen holder was covered with plastic foil after which the concrete was cured under standard laboratory conditions for 2–5 days. The plastic foil was removed, and the surface was finished with Quik-Rok ® concrete as described in Section 3.6.2. Finally, the aluminium cover was removed from the specimen holder. The above-described procedure was applied to both the lower and the upper rock fracture specimens and is described in Figure 3-31.
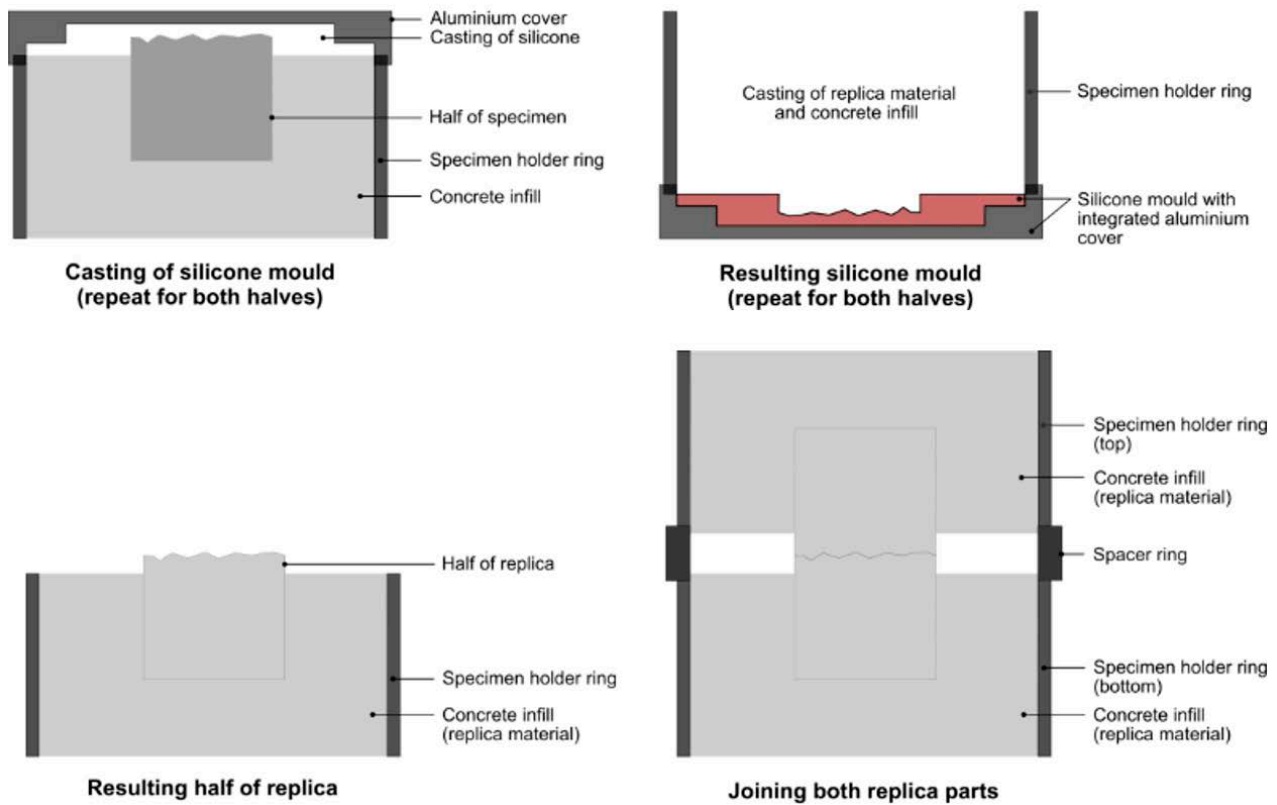
**Figure 3-31.** *Production process for naturally mated replicas.*

### Fully mated replicas

The first step in the manufacturing process of fully mated replicas was to produce a replica of the lower rock fracture surface. Then, silicone was poured into the grouting area encapsulating the fracture followed by 24 hours of curing to create a prescribed space of 10 mm symmetrically above and below the fracture surface specimen. After curing, a release agent was applied on the lower replica fracture surface and on the silicone infill. Finally, the upper replica fracture surface was created as a negative imprint of the lower fracture surface by mounting a spacer ring and a specimen holder followed by casting using Ducorit®D4. Lastly, after curing, the halves were separated. The process is illustrated by Figure 3-32.
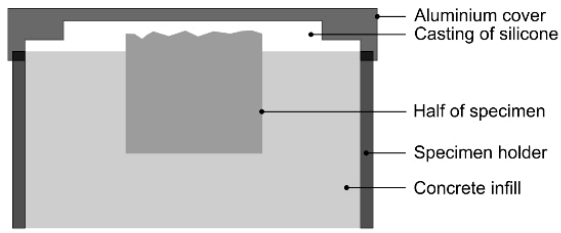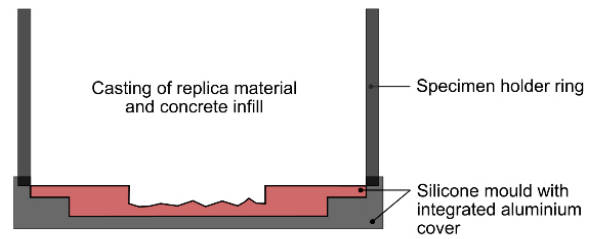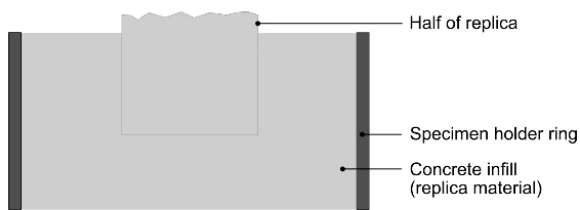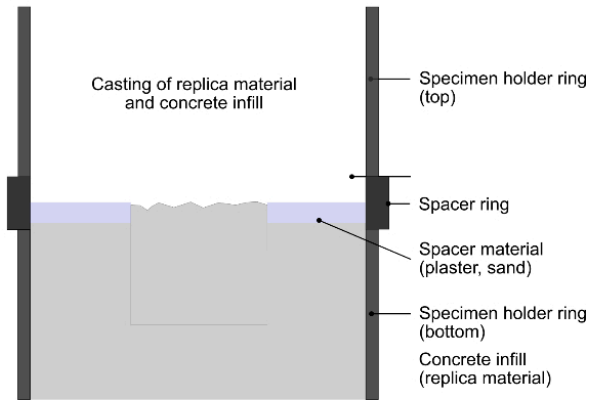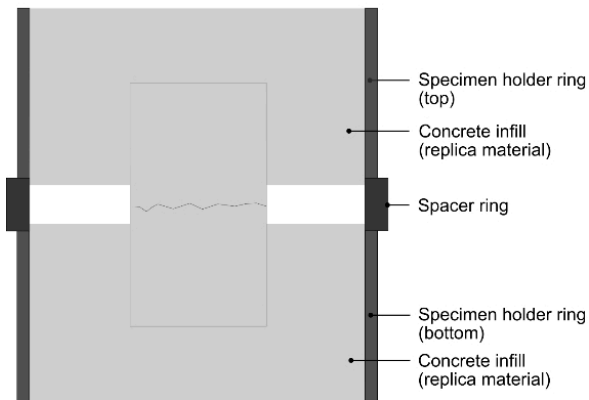
**Figure 3-32.** *Production process for fully mated replicas.*

## 3.7 Steel specimens

After the design and development of the large-scale direct shear test equipment within this project (see Section 5.1) some try-out tests and fine tuning of the system were required. For that purpose, a 500 mm × 300 mm steel specimen with a mean height of each specimen half of 175 mm was manufactured.

The steel specimen consisted of two halves with a planar inclined surface (dipping about 4°) simulating a perfectly smooth fracture. This steel specimen was later on used for determining the system stiffness in the normal loading direction. Similarly, two steel specimens, representative of the medium- and small-size specimens were also used for same purposes. For tests at medium size (those representative of rock specimens measuring 70 mm × 100 mm), an existing steel specimen (two halves) with dimensions 100 mm × 100 mm and about 120 mm height was used (Jacobsson, 2016). For the smallest ones, a specimen (two halves) with dimensions 35 mm × 60 mm and a mean height of each specimen half of 50 mm was resorted to. The inclination angles of the fractures were about 1.8° for the 100 mm × 100 mm specimen, and circa 10° for the 35 mm × 60 mm specimen.

Concerning the grouting of the steel specimens, it was conducted in a similar way as described in Table 3-5, but with the fracture plane inclined to the intended value.

# 4 Characterisation of material and fracture properties

In this section, a description of the mechanical characterisation of granite and replica materials through different tests (compression, tension, basic friction and shrinkage) is provided. The fracture characterisation process is also addressed. Since some tests are common in the characterisation of both materials and for the sake of brevity, a general explanation is provided only in Section 4.1.

The mechanical characterisation of the intact rock material and concrete is further described in Flansbjer et al. (2024) and the tilt tests are on smooth rock and concrete surfaces (Alejano and Pérez-Rey 2025). The scanning of fracture surfaces for the rock and replica specimen are further described in Flansbjer et al. (2024), Jacobsson et al. (2024b) and Jacobsson et al. (2024c).

## 4.1 Mechanical characterisation of granite material

The granite material was characterised by means of different mechanical tests, which can be categorised into three groups: compression, tensile, and friction (basic frictional characterisation from planar (saw-cut) rock surfaces). The associated mechanical and frictional properties, together with the testing methods, are presented in Table 4-1.

**Table 4-1. List of applied tests and expected outputs for granite material.**

| Category | Method | Output/results |
|---|---|---|
| Compression | Uniaxial compressive strength test (Ø54/135 mm) (ASTM D7012-04 (Method D) (ASTM 2004) | Uniaxial compressive strength, UCS<br>Modulus of elasticity, $E$<br>Poisson's ratio, $v$ |
| | Schmidt hammer test (Basu and Aydin 2004, Aydin 2014) | Schmidt hammer rebound hardness (L-type: $R_L$; N-type: $R_N$)<br>Joint Compressive Strength, JCS |
| Tension | Direct tensile strength test (Ø54/135 mm) (ASTM D2936-08, 2008) (ASTM 2008) | Direct tensile strength, DTS |
| | Brazilian test (Ø54/27 mm) (ASTM D3967-16, 2016) (ASTM 2016) | Brazilian (indirect) tensile strength, BTS (ITS) |
| Friction | Tilt test (Alejano et al. 2018) | Basic friction angle, $\phi_b$ |

### 4.1.1 Uniaxial compressive strength test

A uniaxial compressive strength (UCS) test consists in applying a uniaxial compressive load to the top surface of a cylindrical specimen to characterize the compressive properties (e.g. UCS, modulus of elasticity and Poisson's ratio) along with the failure behaviour (e.g. spalling potential).

The UCS tests were conducted using a GCTS servo-hydraulic machine with a stiff load frame (load cell rated up to 1.5 MN and accuracy within 1 %). The stiffness of the various components of the loading chain in the load frame has been optimised to obtain a high total stiffness. Inductive displacement transducers (range ± 2.50 mm and relative error < 0.6 % for axial deformation and < 1.3 % for circumferential deformation) were used as instrumentation for axial and circumferential deformation measurements (Figure 4-1). The sensors, the controller, and the servo valve are rapidly responding components, which prevent the specimen from being crushed after peak stress.
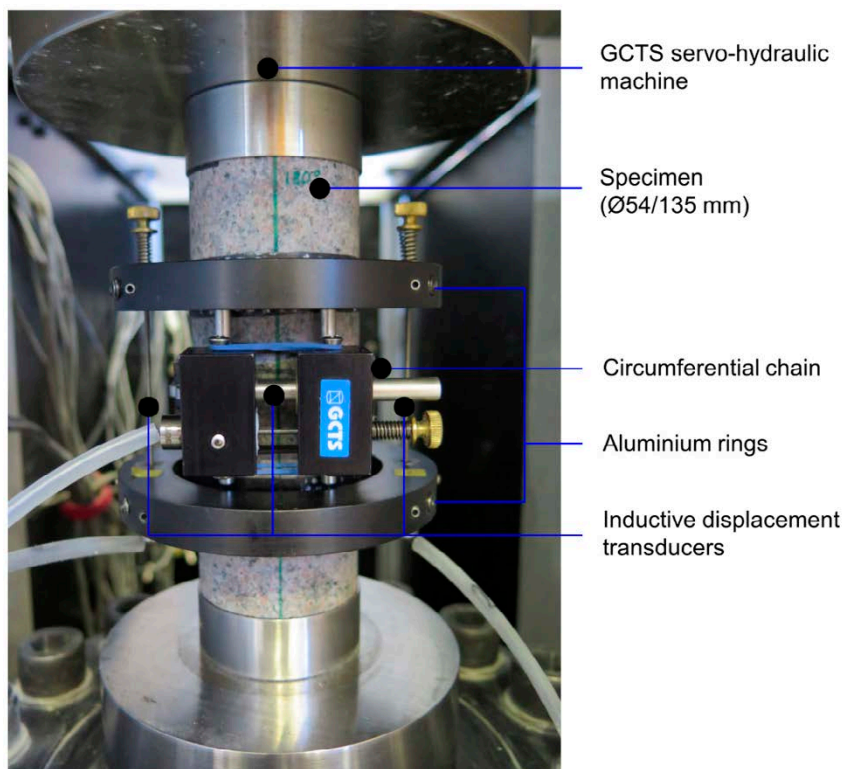
**Figure 4-1.** *Set up for UCS test in granite material.*

The UCS was determined in accordance with ASTM D7012-04, Method D (ASTM 2004), and so was the stress-strain relationship in compression. The UCS was defined as the peak stress and the ultimate strain, $\varepsilon_{cu}$, was defined as the corresponding strain. The elastic properties, i.e. modulus of elasticity, $E$, and Poisson's ratio, $v$, were evaluated as the secant modulus between a lower, $\sigma_l$ (5 MPa) and an upper stress (UCS/3) levels. The axial strain, $\varepsilon_a$, was calculated as the ratio of mean axial deformation and gauge length (distance between rings), while the radial strain, $\varepsilon_r$, was calculated from the circumferential deformation measurements. Poisson's ratio, $v$, was determined as the ratio of radial to axial strain.

Results from the uniaxial compression tests pertaining to the granite material are summarised in Table 4-2. Photos of the front and backsides of the specimens before and after testing as well as specimen specific results can be found in (Flansbjer et al. 2024).

**Table 4-2. List of rock specimens, dimensions and results, for UCS test.**

| Direction (or position) | Specimen ID | Diameter [mm] | Height [mm] | UCS [MPa] | Young's modulus [GPa] | Poisson's ratio [-] |
|---|---|---|---|---|---|---|
| Parallel to shear direction (P1) | D54P2 | 54.2 | 135.7 | 269.4 | 72.9 | 0.321 |
| | D54P3 | 54.2 | 134.9 | 269.9 | 74.0 | 0.326 |
| | D54P4 | 54.2 | 134.9 | 273.7 | 72.1 | 0.308 |
| | D54P5 | 54.2 | 134.9 | 266.2 | 73.0 | 0.317 |
| | D54P8 | 54.2 | 134.9 | 276.5 | 73.4 | 0.313 |
| | Average (std dev) | - | - | 271.1 (4.0) | 73.1 (0.7) | 0.32 (0.01) |
| Normal to shear direction (N) | D54N3 | 54.2 | 135.3 | 269.8 | 74.6 | 0.324 |
| | D54N4 | 54.2 | 135.5 | 264.1 | 71.7 | 0.303 |
| | D54N7 | 54.2 | 135.8 | 268.4 | 73.0 | 0.307 |
| | D54N8 | 54.2 | 135.8 | 267.8 | 73.0 | 0.314 |
| | D54N10 | 54.2 | 135.7 | 269.4 | 72.4 | 0.313 |
| | Average (std dev) | - | - | 267.9 (2.3) | 72.9 (1.1) | 0.31 (0.01) |

The average UCS amounted to 271.1 MPa, (with a standard deviation σ = 4.0 MPa) and 267.9 MPa (with a standard deviation σ = 2.3 MPa) for the P1 and N-series, respectively. Note that these resulting UCS values fall within the expected strength range as the granitic rock encountered in the Forsmark area (Glamheden et al. 2007). Furthermore, the average Young's moduli lie within a similar range to what is typically expected for this type of granite material: 73.1 GPa (with a standard deviation σ = 0.7 GPa) for P1-series, and 72.9 GPa (with a standard deviation σ = 1.1 GPa) for N-series. The average Poisson's ratios amounted to 0.32 (with standard deviation σ = 0.01) and to 0.31 (with standard deviation σ = 0.01) for the P1- and N-series, respectively, which are within a typical range of values for granite: 0.1 to 0.33, according to Gercek (2007).

### 4.1.2  Schmidt hammer test

The Schmidt hammer (SH) test, also referred to as the *rebound* or *impact hammer* test (Basu and Aydin 2004), is widely recognised as a non-destructive technique extensively employed to assess rock quality based on surface rebound hardness. The SH rebound hardness value (denoted as $R_L$ or $R_N$ for L- and N-type Schmidt hammer, correspondingly) is determined from this test, and it is a frequently used index in rock mechanics for correlations with the joint compressive strength (JCS), uniaxial compressive strength (UCS) or Young's modulus ($E$) (Aydin 2014). The measurements were conducted with two types of Schmidt hammer: an L-type Schmidt hammer model *Proceq L-9 6067*, belonging to the Division of Soil and Rock Mechanics at KTH (Stockholm, Sweden), and an N-type *Matest S.p.A Model C380* belonging to RISE (Borås, Sweden).

In what refers to granite material, and by using the L-type Schmidt hammer, four sets of measurements were carried out on natural rock-fracture surfaces pertaining to three direct-shear-test specimens (120 measurements in total) and on an intact planar rock surface of specimen 19.6.3.2 (40 measurements). Average $R_L$ values are summarised in Table 4-3, together with JCS results as indirectly determined from Equations 4-1 to 4-3.

$$JCS = 0.00016 \cdot R_L^{3.47} \qquad \text{(Dearman and Irfan 1978)} \qquad (4\text{-}1)$$

$$JCS = 1.45 \cdot e^{(0.07 \cdot R_L)} \qquad \text{(Aydin and Basu 2005)} \qquad (4\text{-}2)$$

$$JCS = 10^{(0.00088 \cdot R_L \cdot \gamma_m + 1.01)} \qquad \text{(Barton and Choubey 1977)} \qquad (4\text{-}3)$$

**Table 4-3. Average $R_L$ values for Schmidt hammer tests performed on an intact rock block surface and on rock natural fractures.**

| Specimen | Block | Direction | Average $R_L$ (std dev) [no.] | JCS (Equation 4-1; 4-2; 4-3) [MPa] |
|---|---|---|---|---|
| 19.6.3.2 | – | Downward (+90°) | 69 (2) | 389; 185; 452 |
|  | – | Horizontal (0°) | 67 (2) | 342; 155; 393 |
| N2-CNL | Lower | Downward (+90°) | 42 (10) | 69; 28: 102 |
|  | Upper | Downward (+90°) | 45 (7) | 87; 34; 120 |
| N3-CNL | Lower | Downward (+90°) | 46 (11) | 94; 36; 126 |
|  | Upper | Downward (+90°) | 45 (9) | 84; 33; 117 |
| N4-CNL | Lower | Downward (+90°) | 46 (11) | 96; 37; 129 |
|  | Upper | Downward (+90°) | 48 (10) | 105; 40; 138 |

Also for the granite material, the N-type Schmidt hammer was employed for determining the average $R_N$ values and JCS estimates from two rock fractures from two specimens, namely, N2-L-CNS (15.2.2.3) – lower part, and TI3-L-CNS (19.6.3.3) – upper part. The average results $R_N$ values are presented in Table 4-4, together with the JCS, indirectly determined based on Equations 4-4 and 4-5.

$$JCS = 0.00045 \cdot (R_N \cdot \rho)^{2.46} \qquad \text{(Kahraman 1996)} \qquad (4\text{-}4)$$

$$JCS = 0.92 \cdot e^{(0.07 \cdot R_N)} \qquad \text{(Aydin and Basu 2005)} \qquad (4\text{-}5)$$

**Table 4-4. Average R$_N$ values for N-type Schmidt hammer tests performed on a rock natural and tensile-induced fracture.**

| Specimen | Block | Direction | Average R$_N$ (std dev) [no.] | JCS (Equation 4-4; 4-5) [MPa] |
|----------|-------|-----------|-------------------------------|-------------------------------|
| N2-L-CNS | Lower | Downward (+90°) | 58.1 (6.7) | 118.5; 53.7 |
| TI3-L-CNS | Upper | Downward (+90°) | 47.9 (6.5) | 73.7; 26.3 |

The JCS results presented in Table 4-3 (L-type Schmidt hammer) and Table 4-4 (N-type Schmidt hammer) show some variability, partly associated with the different types of empirical correlations used, that cover limited strength values. The differences observed between the results for N2-L-CNS and TI3-L-CNS rock fractures presented in Table 4-4 might be associated with the fact that the tensile-induce rock fractures tend to be rougher than the natural ones, so part of the energy transferred by the Schmidt hammer is used in the fracturing of asperities or grains, leading to lower R$_N$ values.

### 4.1.3 Direct tensile test

The direct tensile test consists in applying uniaxial tension at the ends of a cylindrical specimen until it breaks. It is performed according to the methodology presented in ASTM D2936-08 (ASTM 2008). The specimen ends are glued to two plates and inserted into the tension machine. Two hinges and chains at both ends are used to prevent torque and bending of the specimen during testing (Figure 4-2).

Direct tensile strength results relating to the granite material are summarised in Table 4-5. For the P1-series, the average maximal load was 20.91 kN with standard deviation of 4.66 kN and average direct tensile strength was 9.06 MPa with standard deviation of 0.87 MPa. For the N-series, the average maximal load was 24.59 kN with standard deviation of 5.13 kN and average direct tensile strength was 10.66 MPa with standard deviation of 0.97 MPa. Photos of the front and backsides of the specimens before and after testing as well as specimen specific results can be found in Flansbjer et al. (2024).
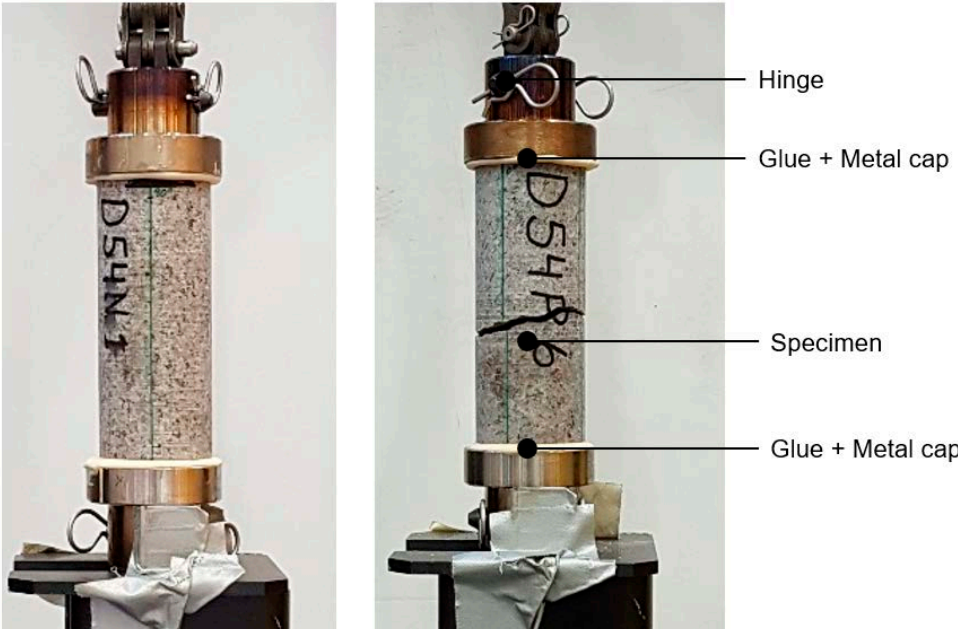


***Figure 4-2.*** *Direct tensile strength test setup (left-hand side) and observed tensile failure (right-hand side) for a rock material specimen.*

**Table 4-5. List of rock specimens, dimensions and results, DTS test.**

| Direction | Specimen ID | Diameter [mm] | Height [mm] | Maximum load [kN] | DTS [MPa] |
|---|---|---|---|---|---|
| Parallel shear direction (P1) | D54P1 | 54.2 | 135.7 | 17.42 | 7.55 |
| | D54P6 | 54.2 | 135.0 | 21.93 | 9.50 |
| | D54P7 | 54.2 | 135.0 | 21.57 | 9.35 |
| | D54P9 | 54.2 | 134.9 | 19.83 | 8.59 |
| | D54P10 | 54.2 | 134.9 | 23.82 | 10.32 |
| | Average (std dev) | - | - | 20.91 (4.66) | 9.06 (0.87) |
| Normal to shear direction (N) | D54N1 | 54.2 | 135.3 | 25.04 | 10.85 |
| | D54N2 | 54.2 | 135.3 | 20.63 | 8.94 |
| | D54N5 | 54.2 | 135.4 | 25.28 | 10.96 |
| | D54N6 | 54.2 | 135.4 | 27.63 | 11.98 |
| | D54N9 | 54.2 | 135.8 | 24.36 | 10.56 |
| | Average (std dev) | - | - | 24.59 (5.13) | 10.66 (0.97) |

### 4.1.4 Brazilian test

The Brazilian test is an indirect-tension test consisting in applying diametric compression to induce tensile stresses in the specimen. It is performed according to the methodology presented in ASTM D3967-16 (2016). During testing, a line load is applied to the top of the specimen which introduces uniform tensile stress across the loaded diameter (see Figure 4-3)
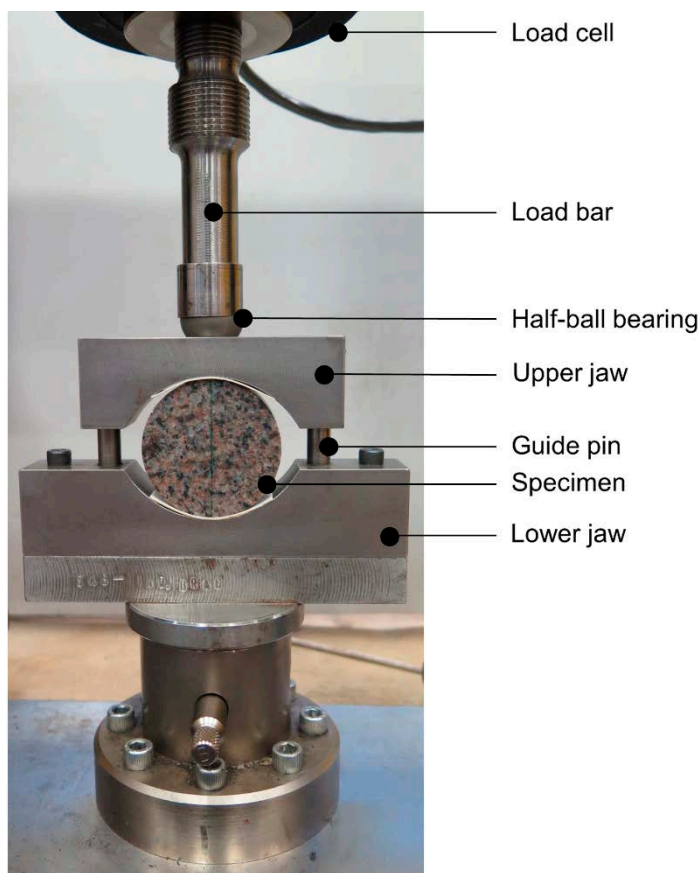


*Figure 4-3.* Set up for Brazilian test on a granite specimen.

The splitting tensile strength results from the Brazilian tests pertaining to the granite material are summarised in Table 4-6.

For the P1-series, the average splitting tensile strength is 14.55 MPa with standard deviation of 0.66 MPa. For the N-series, the average Brazilian (indirect) tensile strength (BTS) is 13.29 MPa with standard deviation of 1.44 MPa. For the P2-series, the average BTS is 13.85 MPa with standard deviation of 0.46 MPa. Photos of the front and backsides of the specimens before and after testing as well as specimen specific results can be found in Flansbjer et al. (2024).

**Table 4-6. List of rock specimens, dimensions and results, Brazilian test.**

| Direction | Specimen ID | Thickness [mm] | Diameter [mm] | BTS [MPa] | Comment |
|---|---|---|---|---|---|
| Parallel shear direction (P1) | BRP111 | 26.0 | 54.2 | 15.90 | |
| | BRP112 | 26.2 | 54.2 | 15.13 | |
| | BRP121 | 25.6 | 54.2 | 14.75 | |
| | BRP123 | 26.0 | 54.2 | 13.39 | |
| | BRP124 | 25.1 | 54.2 | 13.21 | |
| | BRP131 | 26.1 | 54.2 | 13.90 | |
| | BRP133 | 26.0 | 54.2 | 15.27 | |
| | BRP134 | 25.6 | 54.2 | 14.49 | |
| | BRP135 | 24.8 | 54.2 | 15.11 | |
| | BRP136 | 24.8 | 54.2 | 14.33 | |
| | Average (std dev) | - | - | 14.55 (0.66) | |
| Normal to shear direction (N) | BRN11 | 26.0 | 54.2 | 13.34 | |
| | BRN21 | 26.1 | 54.2 | 12.28 | |
| | BRN22 | 25.3 | 54.2 | 13.08 | |
| | BRN23 | 25.6 | 54.2 | 15.40 | |
| | BRN31 | 25.9 | 54.2 | 11.81 | |
| | BRN32 | 25.8 | 54.2 | 11.72 | |
| | BRN33 | 25.6 | 54.2 | 15.10 | |
| | BRN41 | 26.0 | 54.2 | 13.09 | Small cracking at 5.8 MPa and 10.5 MPa |
| | BRN42 | 25.7 | 54.2 | 12.91 | |
| | BRN43 | 26.3 | 54.2 | 14.19 | Small cracking at 5.9 MPa and 12.2 MPa |
| | Average (std dev) | - | - | 13.29 (1.44) | |
| Perpendicular to shear direction (P2) | BRP211 | 26.1 | 54.2 | 13.61 | |
| | BRP212 | 25.5 | 54.2 | 13.65 | |
| | BRP213 | 24.6 | 54.2 | 12.11 | |
| | BRP221 | 26.1 | 54.2 | 14.14 | |
| | BRP222 | 25.9 | 54.2 | 14.15 | |
| | BRP223 | 24.9 | 54.2 | 14.73 | |
| | BRP241 | 25.5 | 54.2 | 13.52 | |
| | BRP251 | 24.8 | 54.2 | 14.04 | |
| | BRP252 | 25.6 | 54.2 | 14.28 | Small cracking at 6.2 MPa and 11.2 MPa |
| | BRP253 | 25.4 | 54.2 | 14.25 | |
| | Average (std dev) | - | - | 13.85 (0.46) | |

### 4.1.5  Tilt test

The basic friction angle of planar (saw-cut) surfaces of granite material was determined through tilt tests on slab-like (80 mm × 70 mm × 20 mm) specimens under different testing conditions (*dry*, *saturated* and *submerged* according to Table 4-7 and illustrated by Figure 4-4. The ISRM Suggested Method (Alejano et al. 2018) was followed as a general methodology for these tests. A micro-scale roughness characterisation was also performed on some granite and replica material specimens to study the evolution of topographic-surface parameters, focusing on roughness (ISO 2012). These parameters were obtained through 3D focus-variation microscopy analyses, at four different testing stages (original surface directly after saw-cutting, and after 15, 30, and 50 tests). Microroughness was analysed in terms of parameters *Sa* and *Sq.* The presence of peaks or valleys on the surface was analysed through the skewness (*Ssk*), and the sharpness of the micro-asperities through the kurtosis coefficient (*Sku*), also obtained at the four stages. This experimental program was entirely carried out in the rock mechanics laboratory at the University of Vigo (Spain) (Alejano and Pérez-Rey 2025). In relation to the micro-scale roughness characterisation, no clear trends could be observed in any of the computed parameters with respect to the frictional behaviour, even though a decay on the frictional response with large (accumulated sliding distance, 50 repetitions) series of tests was evidenced (Figure 4-5).

**Table 4-7. Description of the three testing conditions for tilt-tests.**

| Testing condition | Description |
|---|---|
| Dry | Tilt-tests were carried out with specimens kept in an oven at 60 °C for 24 h before being tested (Figure 4-4a) |
| Saturated | Tilt-tests were conducted on specimens that were kept immersed in water at room temperature (18–22 °C) for 7 days before being tested. The excess water on testing surfaces was removed with a soak cloth before each test repetition, in order to keep the saturation conditions and remove water from specimen surfaces (Figure 4-4b) |
| Submerged | Tilt-tests were carried out with the specimens submerged in water within a methacrylate container while tilted (Figure 4-4c, d) |
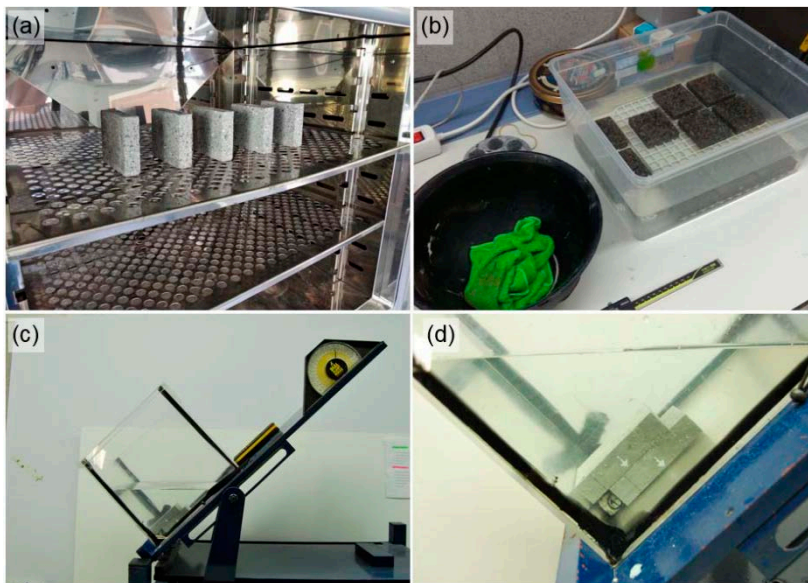


*Figure 4-4.* *Illustrative pictures for the tilt-tests carried out: (a) specimens in the oven for carrying out dry tilt tests; (b) specimens kept submerged in water for carrying out saturated tilt tests; (c) set of containers and specimens for carrying out submerged tilt tests and (d) detail of a submerged tilt test with concrete specimens.*
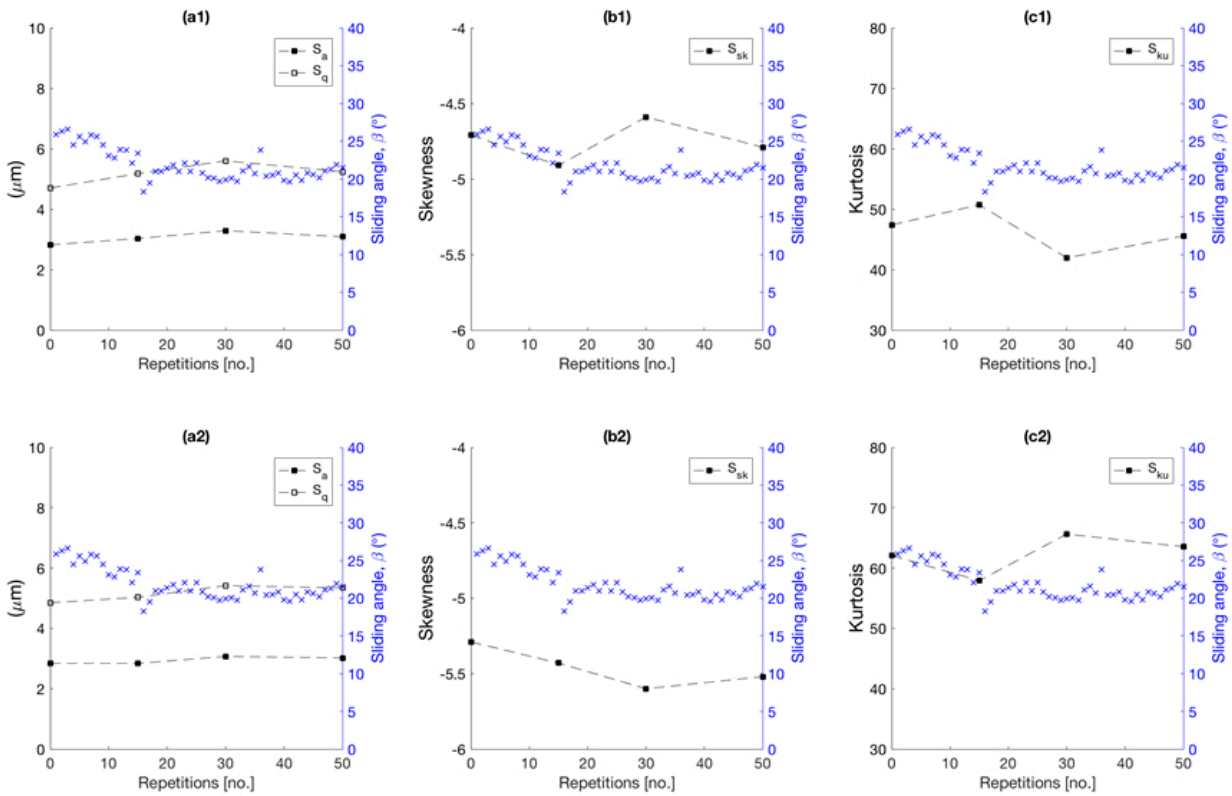
**Figure 4-5.** *Evolution of the surface-texture parameters and sliding angle with the number of repetitions for each granite-material specimen surfaces. From (a1) to (c1): results for top-specimen surface; from (a2) to (c2): results for bottom-specimen surface.*

**Table 4-8. Basic friction angle for granite material. Result expressed for each series as the median of 5 values, and for each testing condition (proposed value) as the average. Standard deviations are also indicated.**

| Test conditions | Series | Basic friction angle, $\phi_b$ (median $\beta_i$=1,…5), [°] | Proposed basic friction angle, $\phi_b$ [°] | Standard deviations of group, [°] |
|---|---|---|---|---|
| Dry | GD(1)- | 22.2 | 23.9 | 1.82 |
| | GD(1)- | 24.4 | | |
| | GD(1)- | 23.3 | | |
| | GD(1)- | 26.1 | | |
| | GD(1)- | 24.4 | | |
| | GD(2)- | 23.8 | | |
| | GD(2)- | 23.7 | | |
| | GD(2)- | 25.4 | | |
| | GD(2)- | 22.4 | | |
| | GD(2)- | 23.6 | | |
| Saturated | GST-1 | 40.9 | 38.1 | 5.73 |
| | GST-2 | 35.7 | | |
| | GST-3 | 33.7 | | |
| | GST-4 | 37.3 | | |
| | GST-5 | 43.0 | | |
| Submerged | GS-1 | 34.1 | 31.0 | 5.42 |
| | GS-2 | 24.2 | | |
| | GS-3 | 36.2 | | |
| | GS-4 | 34.3 | | |
| | GS-5 | 26.2 | | |

## 4.2 Mechanical characterisation of replica material

The material used for manufacturing the replicas was also characterised through various mechanical and frictional properties of planar saw-cut surfaces, as determined from different test methods, which can be categorised, in this case, into four groups: compression, tension, friction and shrinkage tests. In this list, the three first associated properties and testing methods have already been described for the granite and can be reviewed in Table 4-1. Shrinkage tests were performed in concrete slabs and in accordance with the Swedish Standard SS 137215 (SIS 2000). This test allows determining material shrinkage [‰] vs. time [days].

### 4.2.1 Uniaxial compression test

The method for uniaxial compression tests has been previously described (see Section 4.1.1) and is illustrated by Figure 4-1. In the case of replica material, concrete cylinders were initially cast with dimensions of Ø54/200 mm in plastic cylindrical moulds and were sawn to their final length of 135 mm. The specimens were demoulded and stored in a climate room for 7 days (20 °C, RH 50 %) and then stored in the laboratory until testing. The uniaxial compression test results relating to the replica material are summarised in Table 4-9.

**Table 4-9. Summary of results for uniaxial compressive strength tests on replica material.**

| Curing conditions | Additional water content [%] | Test age [days] | No. spec. | Avg. compressive strength [MPa] | Avg. Young's modulus [GPa] | Avg. Poisson's ratio [-] |
|---|---|---|---|---|---|---|
| 7 days 20 °C, RH50 % | +3−5 | 7 | 4 | 159.0 (7.5) | 54.2 (1.4) | 0.244 (0.004) |
| 7 days 20 °C, RH50 % + in laboratory | | 14 | 4 | 176.3 (8.1) | 59.9 (0.9) | 0.258 (0.005) |
| | | 21 | 4 | 195.2 (4.3) | 64.0 (2.6) | 0.264 (0.009) |
| | | 28 | 4 | 197.6 (2.4) | 63.8 (0.5) | 0.260 (0.004) |
| | | 71 | 4 | 205.8 (1.8) | 65.0 (1.2) | 0.262 (0.020) |
| | +8 | 28 | 3 | 179.6 (5.8) | - | - |
| | +13 | 28 | 3 | 181.1 (0.7) | - | - |
| | +9 | 28 | 3 | 205.6 (7.6) | - | - |

### 4.2.2 Schmidt hammer test

In a similar way as performed for the granite specimens, 120 $R_L$ values were retrieved from Schmidt hammer tests on surfaces of three pairs of blocks corresponding to shear-test replica specimens. Average $R_L$ values are summarised in Table 4-10, together with JCS results as determined from Equations 4-1 to 4-3 (Section 4.1.2).

**Table 4-10. Average $R_L$ values for Schmidt hammer tests performed on replicated fractures.**

| Specimen | Block | Direction | Average $R_L$ (std dev) [no.] | JCS (Equation 4-1; 4-2; 4-3) [MPa] |
|---|---|---|---|---|
| **RNM-N1-CNL-5** | Lower | Downward (+90°) | 33 (5) | 31; 15; 63 |
| | Upper | | 35 (7) | 37; 17; 70 |
| **RPM-N1-CNS-6** | Lower | | 35 (7) | 36; 17; 69 |
| | Upper | | 33 (7) | 29; 14; 61 |
| **RNM-N1-CNL-6** | Lower | | 35 (5) | 36; 17; 69 |
| | Upper | | 33 (6) | 28; 14; 61 |

### 4.2.3 Direct tensile test

Direct tensile tests were also performed, in the way already explained in Section 4.1.3 and as illustrated by Figure 4-2 for granite, on cylindrical specimens made up of concrete with 28 and 59 days of curing. The test results pertaining to this material are summarised in Table 4-11.

**Table 4-11. Summary of results for Direct Tensile test (std dev in parentheses) (the + sign stands for an amount of water that exceeds the recommended level by the manufacturer).**

| Curing conditions | Additional water content [%] | Test age [days] | No. spec. | Avg. tensile strength [MPa] |
|---|---|---|---|---|
| 7 days, 20 °C, RH 50 % + laboratory | +5 % | 28 | 1 | 9.0 (-) |
| | | 59 | 2 | 10.7 |
| | +12 % | 28 | 6 | 8.9 (0.4) |

### 4.2.4 Brazilian test

As in the previous cases, concrete cylinders were initially cast with dimensions of Ø54/200 mm in plastic cylindrical moulds and were sawn into disks having a thickness of 27 mm. The specimens were demoulded and stored in a climate room for 7 days (20 °C, RH 50 %) and then stored in the laboratory until testing in a similar setup as for granite specimens (Figure 4-3). Indirect tensile tests were conducted on specimens cured for 7, 14, 21, 28 and 70 days. Test results are summarised in Table 4-12.

**Table 4-12. Summary of results for Brazilian test (std dev in parentheses) (the + sign stands for an amount of water that exceeds the recommended level by the manufacturer).**

| Curing conditions | Additional water content [%] | Test age [days] | No. spec. | Avg. splitting tensile strength [MPa] |
|---|---|---|---|---|
| 7 days, 20 °C, RH 50 % | +5 % | 7 | 5 | 11.0 (0.5) |
| 7 days, 20 °C, RH 50 % + laboratory | | 14 | 5 | 12.6 (0.5) |
| | | 21 | 5 | 13.5 (0.6) |
| | | 28 | 5 | 13.3 (0.9) |
| | | 70 | 5 | 14.7 (1.3) |

### 4.2.5 Tilt test

The basic friction angle for planar surfaces of replica material was also determined for the three testing scenarios in a similar way as already explained in Section 4.1.5. The main results from tilt tests are presented in Table 4-13 for the three testing conditions. The standard deviation per group of tests is also provided.

In what relates to the micro-scale roughness characterisation, as presented in Figure 4-6, no clear trends could be observed in any of the computed parameters with respect to the frictional behaviour of replica surfaces. A decay on the frictional response with large (accumulated sliding distance, after 50 test repetitions) series of tests was evident, maybe less marked than in the case of granite material.

### 4.2.6 Drying shrinkage test

A comparison of the drying shrinkage for the replica material versus time for both investigated scenarios, namely "Water" and "Climate room", is presented in Figure 4-7.

As it can be observed from Figure 4-7 that between 20–56 days the rate of shrinkage minimizes such that the trend becomes a plateau. After 56 days, the shrinkage for the differing scenarios, "Water" and "Climate room", amounted to 0.71 ‰ and 0.88 ‰, respectively. For example, shrinkage for 100 mm × 0.71 ‰ = 0.071 mm; or 100 mm × 0.88 ‰ = 0.088 mm.

**Table 4-13. Basic friction angle for saw-cut planar surfaces of replica material. Result expressed for each series as the median of 5 values, and for each testing condition (proposed value) as the average. Standard deviations are also indicated.**

| Test conditions | Series | Basic friction angle, $\phi_b$ (median $\beta_{i=1,...,5}$) [°] | Proposed basic friction angle, $\phi_b$ [°] | Standard deviations of group, [°] |
|---|---|---|---|---|
| Dry | CD(1)-1 | 33.9 | 27.9 | 3.29 |
| | CD(1)-2 | 27.1 | | |
| | CD(1)-3 | 26.8 | | |
| | CD(1)-4 | 30.2 | | |
| | CD(1)-5 | 26.1 | | |
| | CD(2)-1 | 26.7 | | 2.80 |
| | CD(2)-2 | 27.6 | | |
| | CD(2)-3 | 30.2 | | |
| | CD(2)-4 | 27.3 | | |
| | CD(2)-5 | 23.4 | | |
| Saturated | CST-1 | 38.4 | 39.2 | 6.03 |
| | CST-2 | 43.8 | | |
| | CST-3 | 39.7 | | |
| | CST-4 | 39.6 | | |
| | CST-5 | 34.6 | | |
| Submerged | CS-1 | 39.0 | 36.2 | 2.96 |
| | CS-2 | 36.2 | | |
| | CS-3 | 36.1 | | |
| | CS-4 | 33.4 | | |
| | CS-5 | 36.2 | | |



***Figure 4-6.*** *Evolution of the surface-texture parameters and sliding angle with the number of repetitions for each replica-material specimen surfaces. From (a1) to (c1): results for top-specimen surface; from (a2) to (c2): results for bottom-specimen surface.*
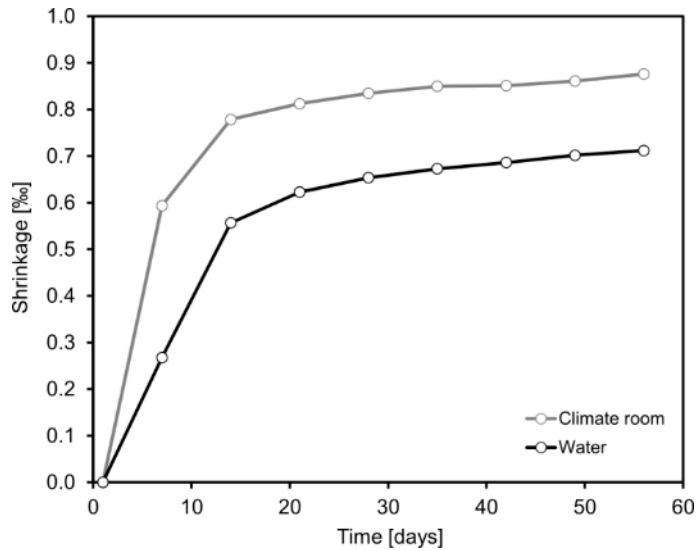
***Figure 4-7.*** *Shrinkage results for replica material.*

## 4.3 3D fracture geometry scanning

In this section, the characterisation of fracture geometry through 3D scanning techniques is presented. The section is divided into two subsections, in accordance with the two techniques used, since the large-size specimens were scanned with a 3D laser technique, while the smaller (medium- to small-sized specimens) were scanned employing blue LED structured light technology. Brief descriptions of the equipment, test procedure, analyses, interpretation, and results are provided herein for both cases. The information presented herein applies both for rock and replica fracture fractures, since the applied techniques were the same for both material surfaces.

### 4.3.1 Large-size specimens

#### *Equipment*

With respect to the large fracture area, a 3D laser scanning technique was employed, preferred over other techniques, e.g., structured blue light. The system tracking the laser, Leica Absolute Tracker AT960, enables both tactile scanning using a probe and contactless scanning in a single setup. In this work, a hand-held Leica Absolute Scanner LAS was used. The tactile probe and the laser scanner work in the same instrument related coordinate system, adding no offset. The laser tracker is tracking a prism from a static setup by the means of angular encoders and interferometric distance measurements. The position of the scanner is measured directly by the position of the prism. The rotation of the scanner is monitored by the camera integrated in the laser tracker following diodes on the laser scanner or probe housing. In all, this enables measurements of six degrees of freedom. The post-processing of the point clouds was accomplished in SpatialAnalyzer® (SA) and in Leica Cyclone 3DR by means of removal of outliers and artefacts. Technical data of the 3D scanning system is summarised in Table 4-14.

**Table 4-14. Technical data of the 3D scanning system.**

| Leica Absolute Tracker AT960 | | Leica T-probe | | Leica Absolute scanner LAS | |
|---|---|---|---|---|---|
| Property | Stated value | Property | Stated value | Property | Stated value |
| Stated angle mean percentage error | ± 15 µm + 6 µm/m | Stated accuracy | 0.035 mm | Maximal sampling rate | 150 000 pts/sec |
| Stated distance mean percentage error | ± 10 µm | | | Maximal line frequency | 100 Hz |
| | | | | Minimum point density | 0.013 mm |
| | | | | Measurement uncertainty of sphere radius | ± 50 µm |

*Test procedure*

The 3D scans were carried out in a single measurement consisting of two main steps. In the first step the geometry of each individual shear box was aligned to the 3D nominal CAD (computer-aided design) model of the shear box. This was achieved by tactile measurements using the T-probe on all accessible surfaces of the casting box. The measurement points were well-distributed over the surfaces. By a best-fit of all points in relation to the nominal CAD model the primary alignment was completed (Figure 4-8).

In the second step, the fracture was scanned using the laser scanner. Scanning was carried out aiming for a complete coverage. For some specimens with more specific features, some areas were scanned from several positions. This resulted in point clouds of up to 35 million points (Figure 4-9).

After scanning, the point clouds were post-processed by filtering of outliers. The filtered point cloud was then used to build up an initial triangular mesh. The initial meshes have in most cases been refined by removal of artefacts. The final meshes were verified against the raw point cloud to ensure consistency in the creation of the meshes. An average point spacing (resolution) of 0.2 mm was aimed for. The final surface models are saved in STL (stereolithography) format composed of triangular planes. The position of the fracture surfaces in relation to the casting box were determined by the tactile probe and the laser scanner working in the same instrument related coordinate system. The lower and the upper parts of the fracture surfaces of each rock fracture specimen are saved in the same coordinate system with the relative position determined by nominal position of 40 mm between the lower and the upper casting boxes. A summary of all the steps performed in this stage is presented in Table 4-15.



*Figure 4-8. Tactile measurements using the T-probe for alignment of the casting box to the nominal CAD model.*

**Figure 4-9.** *Contactless 3D scanning of a fracture surface using the Leica Absolute Scanner LAS with the Leica Absolute Tracker AT960 in the background.*

**Table 4-15. Activities during geometry scanning.**

| Step | Activity |
|------|----------|
| 1 | Positioning of the lower and the upper casting boxes on wooden pallets with the fracture surface facing upwards |
| 2 | Rigging of the Leica 3D scanning system |
| 3 | Tactile measurements of the casting boxes using a T-probe |
| 4 | 3D scanning of the fracture surfaces using a hand-held scanner |
| 5 | Filtering of outliers from the point clouds of the fracture surfaces followed by generation of initial triangular meshes |
| 6 | Refinement of the initial triangular meshes by removal of artefacts obtaining the final meshes |
| 7 | Verification of the final meshes by comparisons with the raw point cloud |
| 8 | Primary alignment of the casting boxes by a best-fit post-processing procedure between the coordinate points from the tactile measurements and the nominal CAD model |
| 9 | Secondary alignment of the 3D scanned fracture surfaces relatively to the casting boxes |
| 10 | Transformation of the lower and the upper fracture surfaces to the same coordinate system with the relative position determined by the nominal CAD model |
| 11 | Saving of the final surface models in STL format |

### Results

The results from the 3D scanning consisted of triangular meshes of the lower and the upper fracture surfaces of each specimen retrieved before and after direct shear testing. Each fracture surface is saved in separate file in STL format. For each specimen, all scans are in the same coordinate system corresponding to a nominal separation of 40 mm between the top surfaces of the casting boxes. An example is shown in Figure 4-10. In the direct shear tests, the upper part was fixed while the lower part was displaced in the positive y direction.

The STL files can be imported to any software in which surface comparisons can be made, e.g. GOM Inspect Pro (GOM, 2018). By pairwise comparisons of the same fracture surface before and after direct shear testing, the wear can be evaluated. For some specimens, large pieces of the fracture surface come loose during shearing. In these cases, the loose pieces also were scanned and saved in separate files. The precision of the position of the loose pieces is not high enough for quantitative wear analysis. The aperture at exposure of the initial normal stress can be evaluated after calibration with the digitised image from contact pressure measurements by calculation of the distances between the coordinate points of the lower and the upper fracture surfaces.
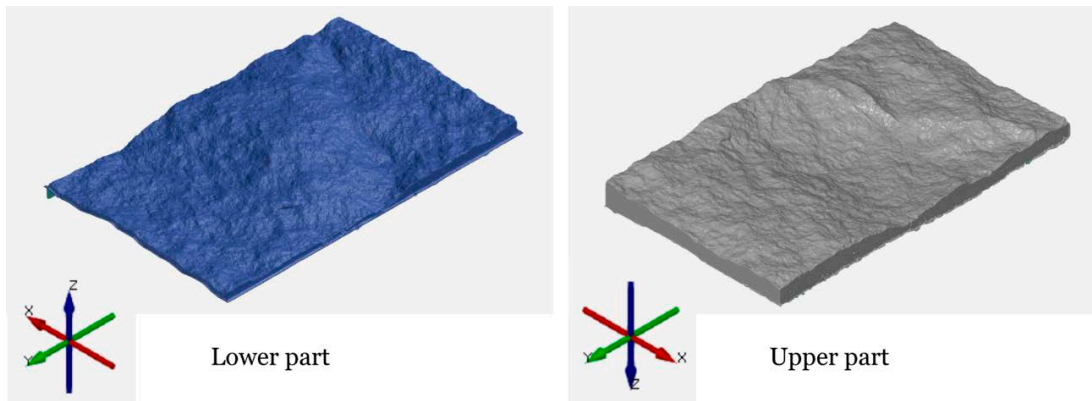
*Figure 4-10. Example of resulting scans saved as STL files with their relative orientation indicated by the coordinate systems.*

### 4.3.2 Medium- and small-size specimens

*Equipment*

For medium- and small-size fracture specimens, all fracture surfaces, grouting areas and top surfaces of the specimen holders were 3D scanned employing blue LED structured light technology using an *Artec Spider* scanner from *Artec 3D*. The blue LED structured light technology means that a series of overlapping frames was captured during hand-held scanning. A frame is a digital image of an instant. The scanner was equipped with a texture camera capturing each 10th frame as a photo. To obtain a 3D model, the scanning data must be post-processed by spatial alignment of the frames and removal of overlapping areas. This was accomplished with the Artec Studio software (versions 2011–2013) to create a textured 3D-model with the help of the photos from the texture camera. This method is the same as the one used on the replica specimens described in Larsson et al. (2023a). By repeating the scanning procedure on the same sample, Larsson et al. (2023a) concluded that an accuracy of 12.5 µm was possible to obtain. This accuracy is slightly better than the one obtained for the large-scale samples (15 µm) using the Leica Absolute Scanner (LAS) as described in the previous section.

*Test procedure*

The scanning was accomplished by slowly turning the specimen placed on a turning table to assure that enough overlapping frames were captured (Figure 4-11).



*Figure 4-11. Scanning the fracture surface (not cast in formwork) on a turning table using an Artec Spider scanner.*

To ensure reproducibility, the scans of all specimens were executed according to the same scanning pattern schematically illustrated in Figure 4-12. With the direction of the scanner indicated Step 1 consisted of scanning the outer region of the specimen, which is described by the area between the two dashed circles. The same procedure was repeated in Step 2, but with the scanner held at a smaller angle to the vertical axis to capture the central parts in addition to the outer edge of the fracture. In Step 3, the vertical walls encompassing the fracture were captured. Lastly, Steps 4 and 5 consisted of scanning the fracture at an angle perpendicular to the plane of the fracture.

The scanning process resulted in a series of overlapping frames. In the subsequent post-processing 3D models were created by spatial alignment of the frames and removal of overlapping areas. This was done in the software Artec Studio (versions 2011–2013). All available post-processing routines in the creation of a 3D model are described in Figure 4-13. The Autopilot option was not used. During scanning, a preliminary automatic run rough registration of the frames was made. This is a preliminary alignment of the relative position of the frames performed by the software in the scanner automatically. Since the scanning of a specimen was performed in one session, the option *Align* was not employed. With the aim to maintain the original position of the scanning point cloud, only *Global* registration and Fusion were employed. In the case there was a need for noise elimination, i.e. outlier removal, this process was executed in the software *3Dreshaper* (2019). The reason for this was to keep control of the required modifications on the point cloud. Noise elimination was only applied in areas outside the fracture surface, which had been subjected to reflections from the structured light in a way causing disturbing artefacts.

Within the *Global* registration routine, a Fine registration was made, which adjusts the position of the frames. The procedure *Geometry* and *Texture* was employed. This means that the algorithm made use of the texture, e.g. the difference in colour between different areas of the fracture, in the positioning of the frames relatively to each other. Moreover, the Loop closure option was used. This algorithm compensates for cumulative errors, preventing the frames to drift when aligned. In the *Global* registration routine, a simultaneous optimisation of all frame positions was made using a single coordinate system. Here a *Key frame* ratio equal to 0.2–0.4 was utilised. This ratio determines how many surfaces are treated as *Key frames* in the registration process. The last parameter used in the *Global* registration routine was *Feature Search Radius*. This parameter controls how sparse the features are located, and can be set 3–5 mm. In this work the default value 5 mm was used. *Max error* is an indicator on the registration quality and should be < 0.6. In this work, it was aimed to achieve 0.2.
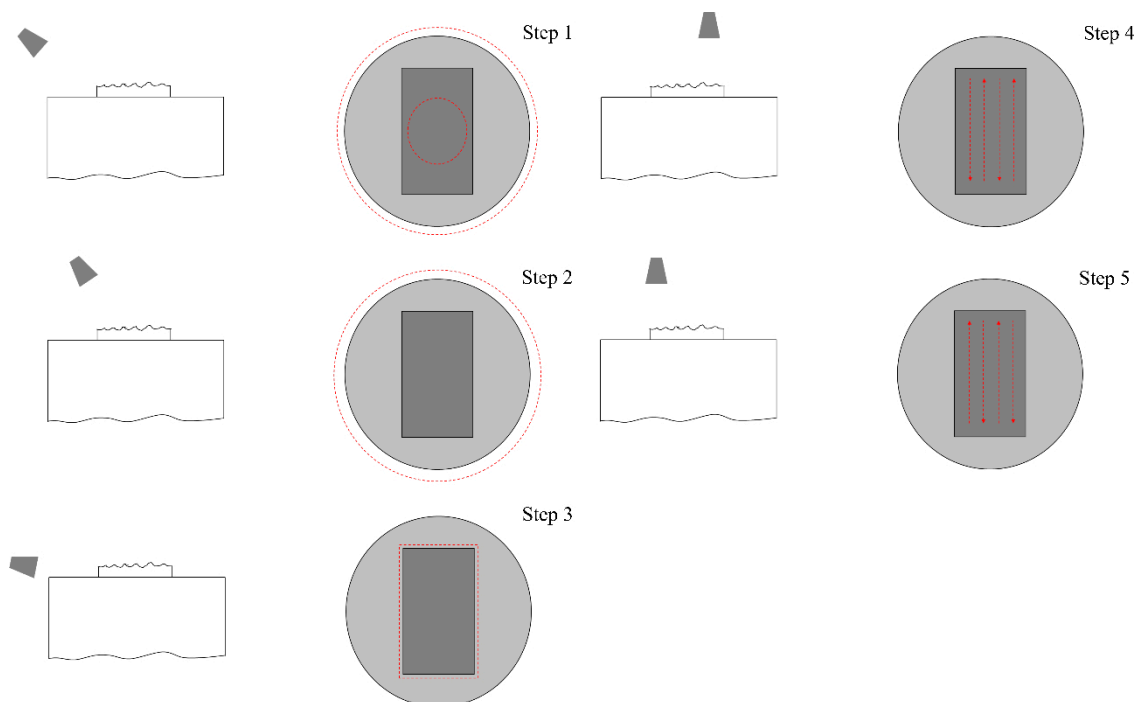


***Figure 4-12.** Schematic illustrations of the scanning pattern.*
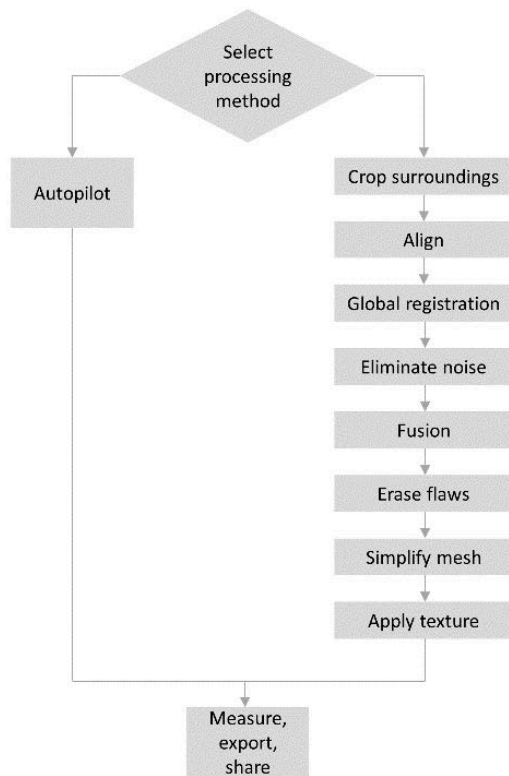
***Figure 4-13.*** *Available process steps to create a 3D model of frames from the scanning. Autopilot option was not used in this work. [Image source: Artec Studio 13 User's Guide/Manual (2017)].*

In the Fusion routine the point clouds were converted to surfaces. Here the Sharp fusion setting was employed, which facilitates capture of details at the expense of increased model size. A resolution, corresponding to the average scanning point spacing, of 0.2 mm was strived for.

The lower and the upper parts of the fracture surfaces of each rock fracture specimen are saved in the same coordinate system with the relative position determined by the lower and the upper fracture surfaces just being in contact. With reference to Figure 4-14 the alignment procedure between the lower and the upper specimen halves was executed as follows. The lower part is master. A primary alignment was made with respect to the Gaussian best-fit planes of the top surfaces of the specimen holders, and a secondary alignment with respect to parallelism of the intersection lines between the Gaussian best-fit planes of the top surfaces of the specimen holders and the Gaussian best-fit planes of the long sides of the fracture surfaces. Finally, a tertiary alignment was made through a concentricity fit with respect to the cylindrical shape of the specimen holders. The final surface models are saved in STL (stereolithography) format composed of triangular planes. The main steps performed in this section are summarised in Table 4-16.

**Table 4-16. Activities during geometry scanning.**

| Step | Activity |
|------|----------|
| 1 | Positioning of the specimen on the turning table |
| 2 | Execution of the scanning in accordance with the specified pattern |
| 3 | Post processing according to the described Global registration routine |
| 4 | Post processing according to the described Fusion routine |
| 5 | Transformation of the lower and the upper fracture surfaces to the same coordinate system with their relative position according to the alignment procedure |
| 6 | Saving of the final surface models in STL format |
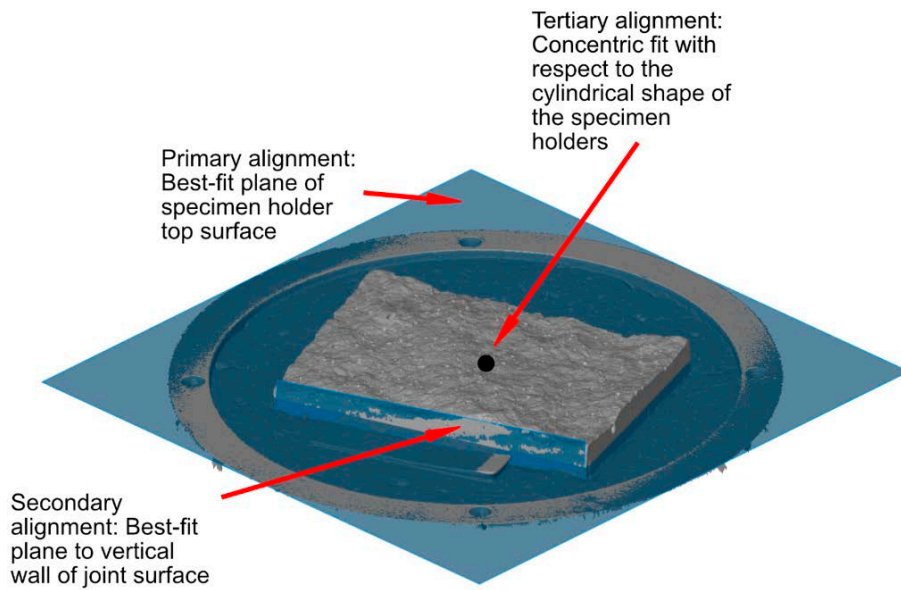
*Figure 4-14. The alignment between the lower and the upper fracture surfaces (Larsson et al. 2023a).*

### Results

The results from the 3D scanning consists of triangular meshes of the lower and the upper fracture surfaces of each specimen before and after direct shear testing. Each fracture surface is saved in a separate file in STL format. For each specimen, all scans are in the same coordinate system with the lower and the upper halves positioned in the z-direction to just be in contact. An example is shown in Figure 4-15. In the direct shear tests, the upper part was fixed while the lower part was displaced in the positive y-direction.

The STL files can be imported to any software in which surface comparisons can be made, e.g. GOM Inspect Pro (GOM, 2018). By pairwise comparisons of the same fracture surface before and after direct shear testing the wear can be evaluated. The aperture at exposure of the initial normal stress can be evaluated after calibration with the digitised image from contact pressure measurements by calculation of the distances between the coordinate points of the lower and the upper fracture surfaces.
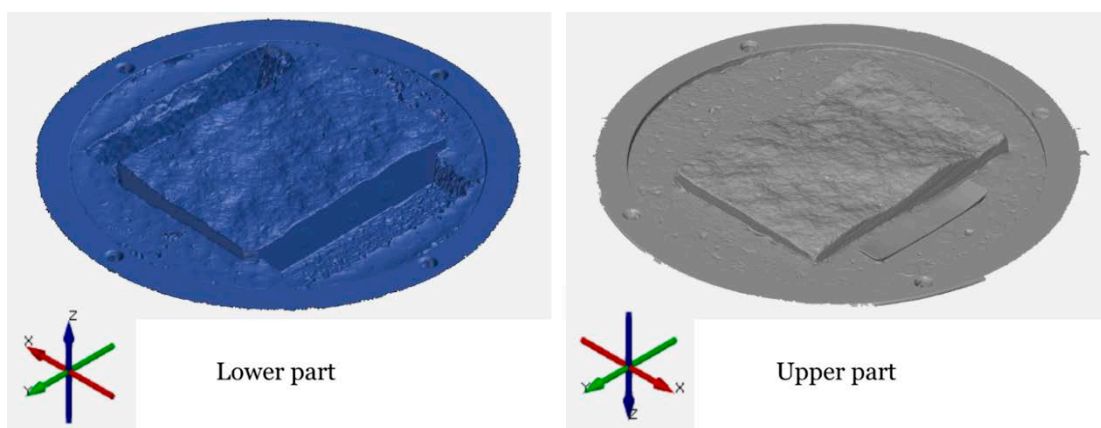


*Figure 4-15. Example of resulting scans of a 70 mm × 100 mm specimen saved as STL files with their relative orientation indicated by the coordinate systems.*

## 4.4 Contact pressure measurements

### 4.4.1 Equipment

The Fujifilm Pressure Distribution Mapping System for Prescale of type FPD-8010E was applied to measure and analyse the contact area and the contact pressure distribution between the fracture surfaces before direct shear testing. This was done with the aim to be able to follow up actual areas in contact of the fracture samples. A few specimens were also measured after direct shear testing. The system includes a software, scanner and Prescale film. A low-pressure (LW) film, composed of a two-sheet configuration with a pressure detection range 2.5–10 MPa was used. Each sheet has an approximate thickness of 90 μm. The Prescale film functions such that it becomes red coloured at locations in contact where the pressure is applied, as shown in Figure 4-16. The actual colour intensity corresponds to a given pressure value; it is to say that the colour density changes according to pressure level.

The colourised film is then digitized in the dedicated scanner and saved in a file containing information that can be processed in the software included in the FPD-8010E pressure measurement system. The software has a user interface which offers various possibilities of graphical representations of the contact pressure distribution. Text files containing quantified data, as contact area ratio and contact pressure distribution, can be exported from the software.
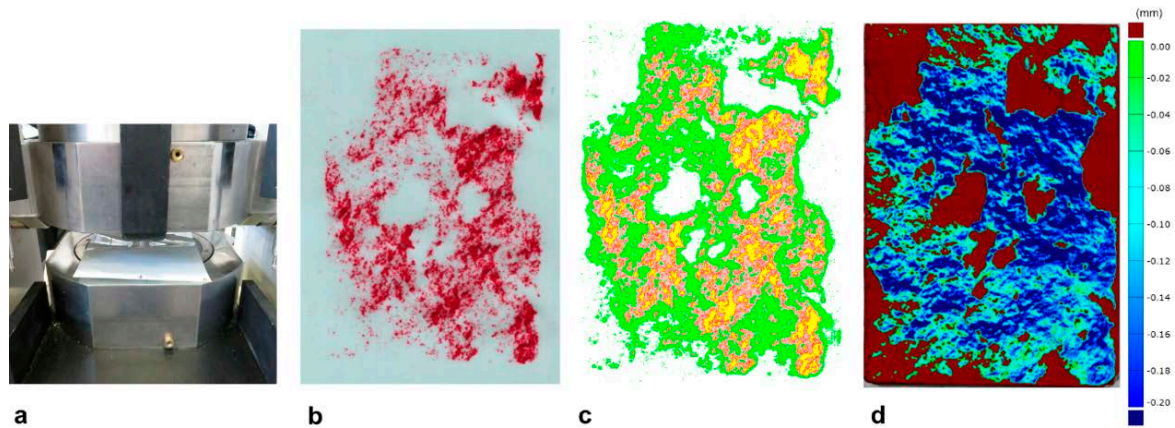
### 4.4.2 Test procedure

The contact-pressure measurement procedure consisted of two phases. The first phase was the contact-pressure measurement. The second phase corresponded to the post-processing of the contact-pressure measurement. As a first step in the first phase, the A and C sheets were removed from their packages and cut into an appropriate size for the given fracture size. For the LW film, with the matt sides of the A and C sheets facing each other the sheets were fixed to each other with pieces of tape along the edges. Then, with the specimen mounted in the shear test equipment, the film was inserted on the lower fracture surface, for the LW film, with the glossy side of the C sheet facing upwards (Figure 4-17a). After the film had been subjected to 5 MPa, applied at a rate of 2.5 MPa/min and maintained for 2 min, the areas in contact were colourised (Figure 4-17b). This step finished the first phase.

The first step in the post-processing phase was calibration of the scanner. This was accomplished by scanning a calibration sheet. After successful calibration the colourised film was placed in the scanner, for the LW film, with the glossy side of the C-sheet facing downwards. After completion of the scanning the dedicated software calculated the contact pressure distribution, which can be visualised in the form of a digitised image (Figure 4-17c) and saved into a file. Subsequently, the digitised images can be used for calibration of the 3D scanning data by translation and rotation of the upper parts in relation to the lower parts in the normal loading direction and around the axes, respectively, until a match between the measured colour maps and the scanning data was obtained (Figure 4-17d). From the calibrated scanning data, for example the aperture distributions can be calculated. A summary of the activities for contact-pressure distribution measurements is provided in Table 4-17.
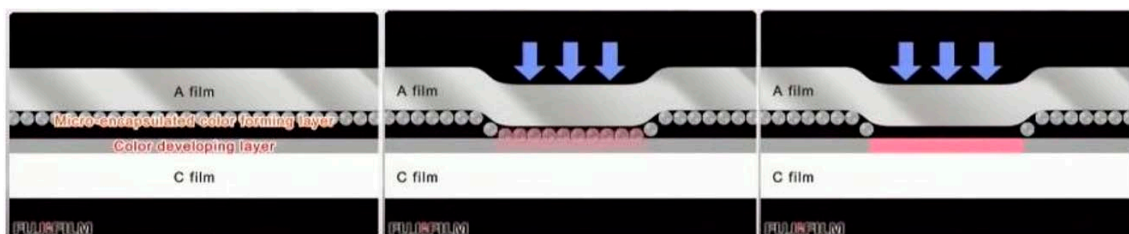


*Figure 4-16. Interaction between A- and C-films for the two-sheet type. Image source: (Fujifilm Corporation 2019).*

**Figure 4-17.** *The contact pressure measurement procedure (from Larsson et al. 2023a). a) Contact pressure measurement with the pressure measurement film positioned on the lower specimen in the shear test equipment prior to normal loading test. b) Pressure measurement film after normal loading test with areas in contact in red with the intensity corresponding to a certain pressure value. c) The colourised film after digitisation in which green areas indicate pressures under, red within and yellow above the pressure detection range 2.5–10 MPa. d) The corresponding calibrated scanning data to obtain the contact area at 5 MPa as basis for derivation of the aperture distribution. The legend indicates the distance between the coordinate points of the lower and upper part in the normal loading direction, i.e. the aperture. Zero indicate areas just in contact and negative values indicate areas deformed under the contact pressure.*

**Table 4-17. Activities during contact pressure distribution measurements.**

| Step | Activity |
|---|---|
| 1 | Cutting of the sheets into appropriate size followed by fixing the sheets to each other with tape |
| 2 | Insertion of the film on the lower fracture surface in the shear test equipment |
| 3 | Subjection of the film to normal loading to obtain the areas in contact colourised |
| 4 | Calibration of the scanner |
| 5 | Scanning of the colourised film obtaining the contact pressure distribution |
| 6 | Saving of output in terms of digitised images and files containing digital contact pressure data |

### 4.4.3 Results

The results from the contact pressure measurements are documented in five file types. All data from the scans of the colourised films are available in files named "Specimen_identity_LW_5MPa.fpd". These files can only be read by the software included in the *Fujifilm FPD-8010E* pressure distribution mapping system.

For large-size specimen fractures, images of the colourised films are saved in files named "Specimen_identity_serial_number_LW_5MPa_po0.bmp". The serial numbers 1 to 3 are there since three films were required to cover the fracture area for this type of fractures (Figure 4-18). The images are oriented with the left side in the shear direction. The images represent a view looking at the lower fracture surface. The upper fracture surface was fixed during shearing with the lower fracture surface moving in the shear direction. In most cases, the left sides are marked with an arrow pointing in the shear direction or the specimen designation.

In the third type images of the digitised colourised films are saved as "Specimen_identity_LW_5MPa_po0.png" or as "Specimen_identity_LW_5MPa_po0.bmp". The images of the digitised colourised films are aligned with the images of the colourised films. An example is shown in Figure 4-19.

**Figure 4-18.** *An example of images, saved in \*.bmp format, of the colourised films for a large-size specimen fracture.*
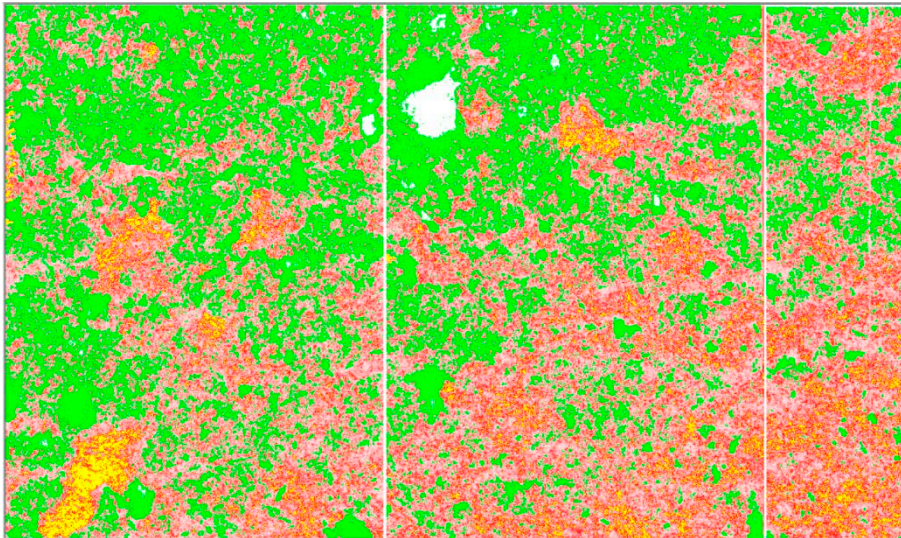


**Figure 4-19.** *The image of the digitised colourised films shown in Figure 4-18.*

The fourth file type contains the pressure data in a $560 \times 560$ matrix in which the position of the elements represents the corresponding position on the fracture surface oriented as the digitised images. The files are named "Specimen_identity_LW_5MPa_560x560.txt". Some cases require the elements to change places by flipping them about a y axis located in the middle of the matrix to agree with the digitised images. Those files are named "Specimen_identity_LW_5MPa_560x560_flip_about_yaxis_before_use.txt".

The fifth file type is designated "Specimen_identity_LW_5MPa_sum.txt". These files contain summaries about the contact pressures and areas. A MATLAB code named "Cont_press" reads the \*_sum.txt files and generate a graphical output shown in Figure 4-20. A more comprehensive presentation of the results from the contact pressure measurements are presented in Jacobsson et al. 2024a and Jacobsson et al. 2024b for the small to intermediate and the large-scale samples, respectively.
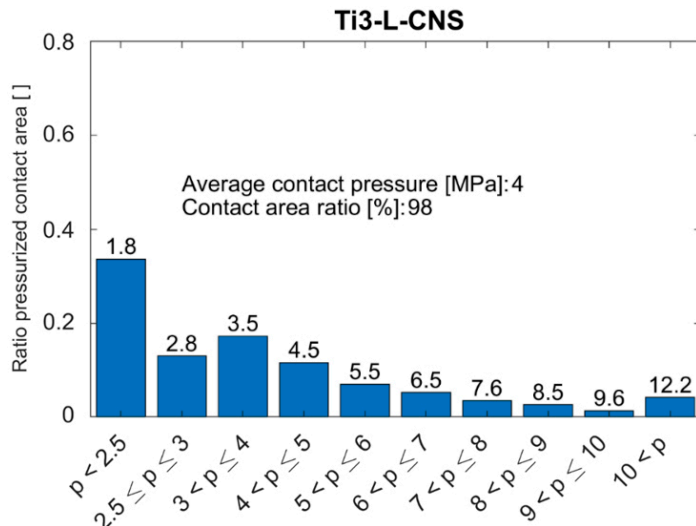
*Figure 4-20. An example of the graphical output from the MATLAB code "Cont_press" reading the \*_sum. txt files.*

### 4.4.4 Interpretation

The resulting digitised contact pressure distributions are saved as *.fpd files, which is a dedicated format of the software in the FPD-8010E pressure measurement system. For each specimen two types of output files have been exported from the FPD-8010E pressure measurement system. The files are in *.txt format and can be imported to other software, e.g. MATLAB, for additional analyses.

The files of the first type are named "Specimen_identity_LW_5MPa_560x560.txt". These files contain the pressure data as a $560 \times 560$ matrix in which the position of the elements represents the corresponding position on the fracture surface. The value of the elements contains the pressure value of the specific position in question. All files, regardless of the size of the scanned Prescale film, are of this size. This means that an averaging of the original data has been executed and that the averaging varies with respect to the size of the Prescale film (the specimen size). The averaging is done automatically in the FPD-8010E program. In the export from the FPD-8010E the 1/1(A) setting was used, which means that no further compression of the $560 \times 560$ data was made. The files of the second type are named "Specimen_identity_LW_5MPa_sum.txt". These files contain summaries of the digitised contact pressure distributions. An example of the content of the files is shown in Figure 4-21.

```
Whole Area Measurement

Sample Name     N1-L-CNS          Prescale Effective Rate(%)     46.5
Examination Date & Time 2022-03-08 00:00      Pressed Area(mm2)      130165.0
Measurement Date & Time 2022-03-15 09:40      Ave Pressure(MPa)      3.65
Prescale Type   LW      Max Pressure(MPa)     12.75
Pressure Type   Continuous      Load(N) 475103
Resolution      0.125   Measured Area(mm2)     143782.0
Scan Count      3
Temperature(°C) 22
Humidity(%)     45


Pressure Range (MPa)    Pressed Area(mm2)     Ave Pressure(MPa)     Max Pressure(MPa)
p <  2.50        62173.0 1.50    2.45
2.50 <= p <= 3.00       12219.0 2.75    3.00
3.00 <  p <= 4.00       15666.0 3.50    4.00
4.00 <  p <= 5.00       10759.0 4.45    5.00
5.00 <  p <= 6.00       7086.0 5.45    6.00
6.00 <  p <= 7.00       5652.0 6.50    7.00
7.00 <  p <= 8.00       4024.0 7.55    8.00
8.00 <  p <= 9.00       3280.0 8.50    8.90
9.00 <  p <= 10.00      1801.0 9.55    9.80
10.00 <  p      7504.0 12.30   12.75
```

*Figure 4-21. Example of the content of a "Specimen_identity_LW_5MPa_sum.txt" file.*

The interpretation of the content is as follows:

- Effective Rate: This is the proportion within the pressure detection range of the Prescale film. It is the red section (within the detection range) of the total surface area reproduced in red, yellow, and green on the digitised images (yellow is the part above the upper limit, red within the range (2.5–10 MPa, for LW-type film), and the green is the part below the lower limit. The white areas correspond to no contact pressure). Note that the Effective Rate is not equal to Pressed Area/ Measured Area.

- Measured Area: This displays the surface area of the area subject to processing by the FPD-8010E system. It is the area specified and scanned with the scanner.

- Pressed Area: The size of the coloured area, including red, yellow and green areas.

- Ave Pressure: The average pressure over the coloured area, including red, yellow and green areas.

- Max Pressure: The maximum pressure over the coloured area, including red, yellow and green areas.

- Load: The load applied over the colourised area, including red, yellow and green areas, calculated as the product of the Pressed Area and the Ave Pressure.

Note that care should be taken when using the load and pressure values. The reason is that the detection range of the film is 2.5 to 10 MPa. The pressures in areas in contact but with values out of the range are uncertain or unknown. Therefore, discrepancies appear between the applied 5 MPa and the average pressures from the "*Specimen_identity*_LW_5MPa_sum.txt" files. Of the same reason discrepancies appear between the applied normal load and the loads in the files. In addition, the actual fracture areas differ from the measured areas, which are the scanned areas in the contact pressure measurements. Errors are introduced when clipping the areas to be scanned from the films, which deviates from the actual fracture areas. Within the detection range the measured pressures apply. The contact pressure measurement data is also useful for evaluations with respect to contact area ratio and contact pressure distribution. The data from the contact pressure measurements could also be used to identify and analyse differences between fractures in terms of the spatial variation in aperture/contacts. However, when these measurements are interpreted, it should be noted that the pressure measurement film has a thickness of 92 micrometer. This thickness is not neglectable compared to the aperture for a well mated fracture and could result in that the area in contact are to some extent overestimated.

## 4.5 Replica characterisation

The geometrical characterisation and verification of the applied replica method's replicability were done by surface scanning and contact-pressure measurement assessments. The initial replica test program consisted in a parametric study on replica samples. The main purpose of this study was to be able to determine if fracture replicas can adequately reproduce the behaviour of actual rock fractures with measurements 70 mm × 100 mm, when subjected to the same type of direct shear tests.

This test program encompassed a total of 15 specimens based on the small-scale rock specimen N1-M-CNL. In relation to the natural fracture, replicas were made using both natural match and perfect match approaches. It is to say that natural match entails the production of a replica mould and specimen for each individual fracture surface of the reference, while perfect match simply involves the replica mould and specimen production pertaining to one fracture surface.

In relation to the natural fracture reference, six replica specimens were produced with natural match, namely RNM-N1-CNL-(1-6), and nine with perfect match, namely RPM-N1-CNL-(1-3), RPM-N1-CNS-(1-6). The specimens were tested in a benchtop direct shear test machine (see Chapter 5). The replica specimens were tested in either CNL or CNS, which is indicated according to the prescribed Sample ID. A summary of the specimen specifications is presented in Table 4-18.

**Table 4-18. Specimen specifications for initial replica tests.**

| Sample ID | No. specimens | Dimensions B [mm] | L [mm] | Specimen type | Test conditions |
|---|---|---|---|---|---|
| RNM-N1-CNL-(1-6) | 6 | 70 | 100 | Replica, Natural match | CNL |
| RPM-N1-CNL-(1-3) | 3 | 70 | 100 | Replica, Perfect match | CNL |
| RPM-N1-CNS-(1-6) | 6 | 70 | 100 | Replica, Perfect match | CNS |

### 4.5.1 Surface comparisons

The scanning data (resulting STL files) obtained according to Section 4.3 was imported to a commercially available software, GOM Inspect Pro (GOM, 2018), in which the surface comparisons, in terms of vertical deviations between the replicas and the rock specimen, were calculated for each scanning point. This software is dedicated to inspecting measurements between nominal data (in the current case, the rock fracture specimen) and actual data (join replica). Before the deviations could be calculated, the replicas had to be aligned with the rock specimens. The alignment refers to the process of adjusting the coordinate points in scanning data of a replica to match the rock fracture specimen using reference elements such as planes, points, or lines, or by using best-fit operations on selected portions of the scanning data. GOM Inspect Pro (GOM, 2018) was also utilised to conduct surface comparisons in this study, as it contains all the necessary built-in routines. Only those influences originating from surface morphology were considered, as highlighted in red colour in Figure 4-22.

Three different moulds for the lower parts were manufactured (manufacturing date in parenthesis): 1B-5 (171122), 1B-6 (171123) and 1B-9 (171128). The corresponding data for the upper parts is: 1A-1 (171116), 1A-2 (171117) and 1A-3 (171120). The rock specimens were scanned after all moulds had been manufactured. The results from the surface comparisons between the lower part of the rock specimen N1-CNL and the replica RNM-N1-CNL-1 are shown in Figure 4-24, while the corresponding results for the upper parts are shown in Figure 4-25.

*Morphology*

Figure 4-23a and Figure 4-23b illustrate examples of 3D scanned replica and rock fracture surfaces, respectively. To isolate influences solely originating from morphology, the alignment process relied only on the coordinate points constituting the fracture surfaces and their perimeter, as highlighted in Figure 4-23c. In Figure 4-23d the aligned replica and rock fracture surfaces are shown. In Figure 4-23e, a resulting surface comparison regarding morphology is exemplified. These surface comparisons were conducted by measuring the distance from each coordinate point on the replica surface to its corresponding point on the rock fracture surface in the normal direction to the best-fit plane of the rock fracture surface. The best-fit planes were obtained by minimizing the residuals of the sum of squares of the coordinate points.
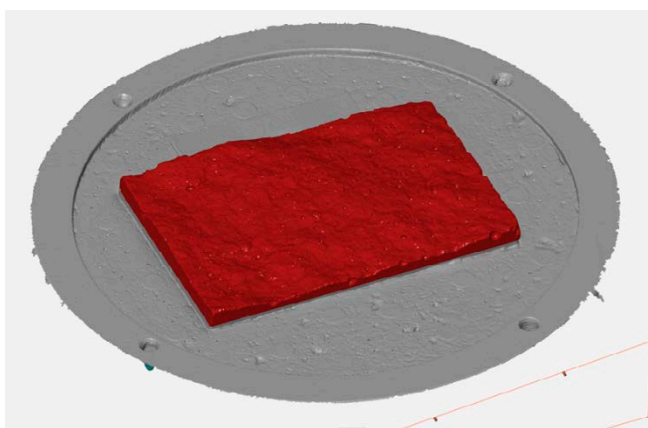


*Figure 4-22. Area of the fracture (highlighted in red colour) to which the best fit operations were applied to align the replicas with the rock specimen.*
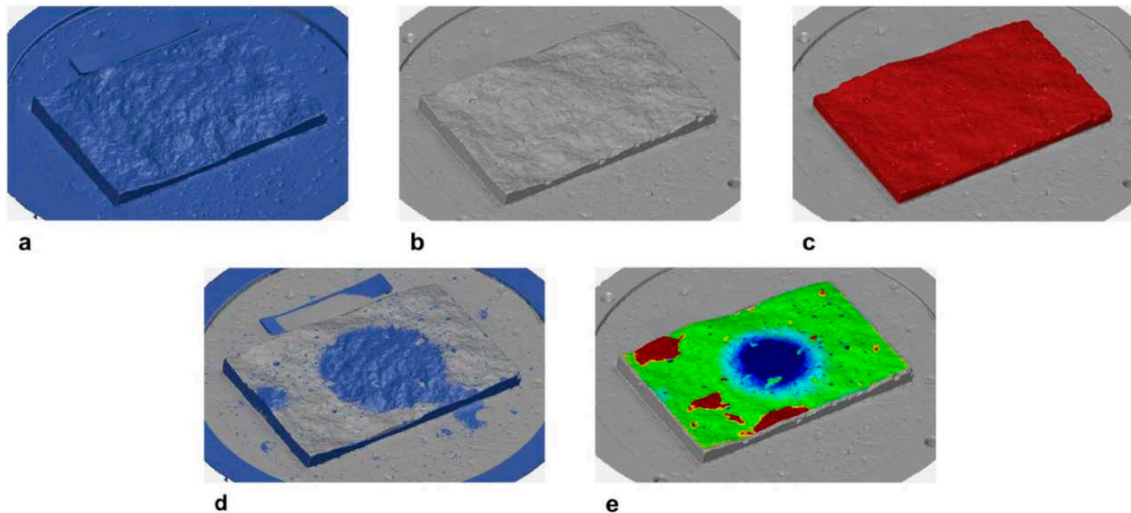
*Figure 4-23. a. 3D scanned replica fracture surface; b. 3D scanned rock fracture surface; c. The highlighted marking constituted by the fracture surface and its perimeter indicates the area containing the coordinate points that were used to align the rock fracture with the replicas using a least-square-fit before subsequent analysis of morphological deviations; d. Aligned replica and rock fracture surfaces; e. Graphical illustration of the resulting surface comparison (Larsson et al. 2023a) CC–BY 4.0 https://creativecommons.org/licenses/by/4.0).*

## 4.5.2 Quantitative surface comparison

Figure 4-24 and Figure 4-25 show the results from surface comparisons between the rock fracture and the replicas with respect to morphology of the lower and upper fracture surfaces, respectively. The results for each individual mould are shown on separate rows, and the manufacturing order is from the left to the right, i.e., the latest produced replicas rightmost as follows from Table 4-18. Even if not required for extraction of the geometric quality assurance parameters, the surface comparisons could be used to identify the type of shortcomings in the replica manufacturing process, which are of relevance to present with respect to the widespread usage of replicas. Four types of deviations could be identified: pores, fragments of positive deviations, circular negative deviations in the centre and positive deviations along the boundaries. It is also observed that these deviations, except the deviations originating from fragments (Mould 1A-1 and 1A-2) could be eliminated after adjustments in the manufacturing process.

The presence of pores can be seen in most of the replicas manufactured in the first batch, RNM-N1-CNL-1–3. The pores originate from air bubbles during concrete casting and were further reduced by stepwise casting with added vibration, in which first a thin layer was applied and thoroughly stirred to release the trapped air. In the replicas from the second batch, RNM-N1-CNL-4–6, there were no presence of pores, or the number of pores had been clearly reduced.

The replicas in Figure 4-24 manufactured from moulds 1A-1 and 1A-2 show local regions with large distinctive positive deviations. These originate from loose fragments coming off from the rock fracture surface during separation of the moulds after curing. The scans of the rock fracture surfaces were done after manufacturing of the last mould. From the chronology of the manufacturing order of the moulds in conjunction with the appearance of the surface comparisons (Figure 4-24), it follows that all fragments except from the fragment in the lower long side came off in the manufacturing of mould 1A-1. The fragment in the lower long side came off during manufacturing of mould 1A-2, which is confirmed by the last manufactured mould, 1A-3, not containing any deviations originating from fragments coming loose. The fragments were stuck in the moulds and peeled off before casting of the replicas, which explains the positive deviations in the replicas. This type of deviation was later eliminated by ensuring that all loose fragments were removed from the rock fracture surfaces prior to mould manufacturing. The fractures in the rock specimens were pre-conditioned by applying thin layer of silicone, which was then peeled off with the purpose to remove the loose material.
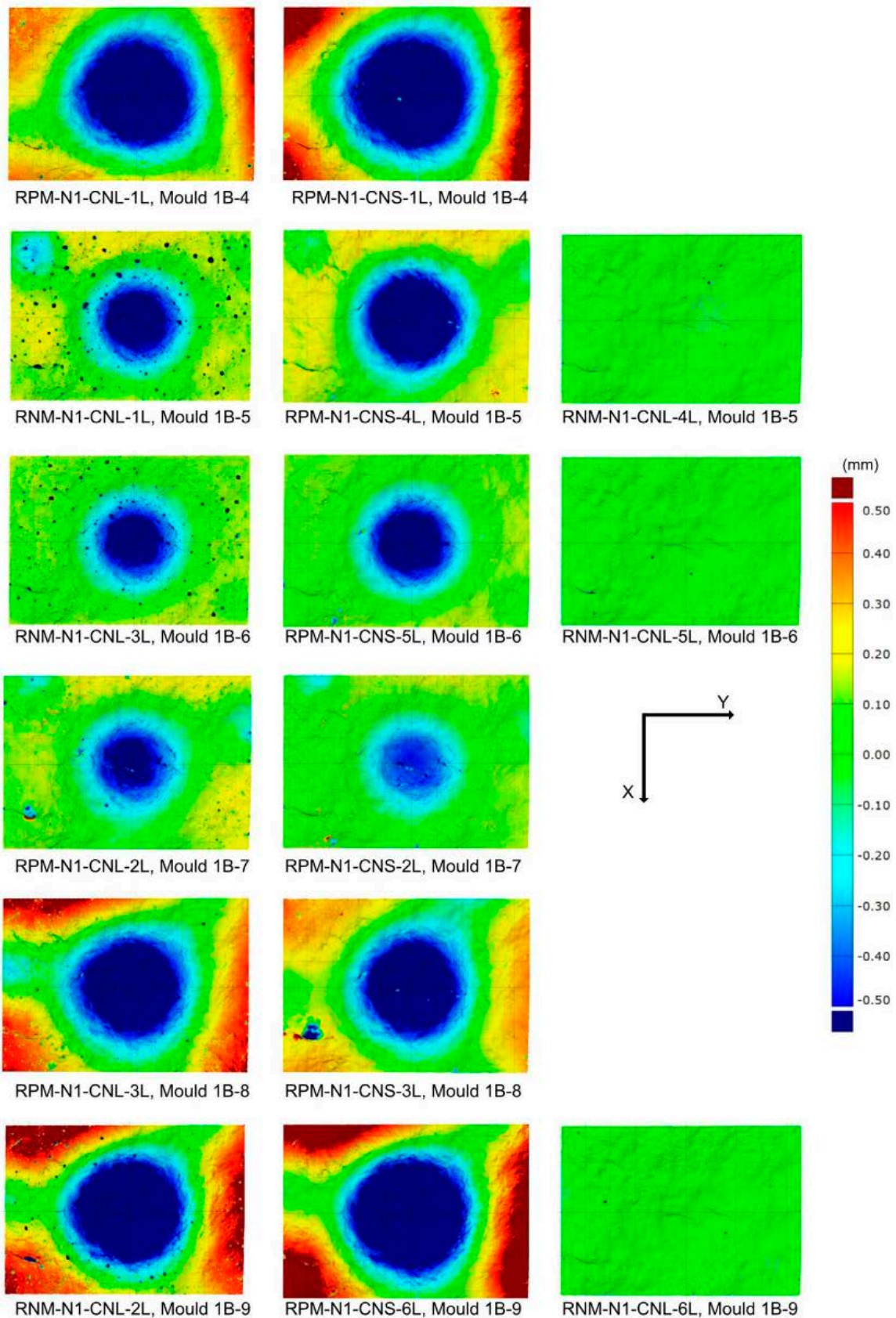
**Figure 4-24.** *Surface comparisons between the mother rock and the replicas with respect to morphology showing deviations in the lower fracture surface. The legend limits are ± 0.5 mm. Upper limit indicates positive deviations corresponding to areas on the replicas laying above the mother rock fracture surface. Larsson et al. (2023a)*

The circular negative depressions (Figure 4-23 and Figure 4-24) in the centre of replicas RNM-N1-CNL-1–3 were found to originate from the positioning knobs between the mould and the aluminium cover formed by the holes (risers) in the aluminium cover during curing of the moulds (Figure 3-30a). After removal of the mould from the aluminium cover, failing to reposition the mould before casting to the bottom of the cover resulted in a convex shape of the mould, which in turn yielded negative deviations (lower surfaces) in the replicas. The knobs were cut off before the casting campaign May 7th, 2018, which removed the depressions. Moreover, positive deviations along the boundaries most clearly seen in RNM-N1-CNL-2L, -3U; RPM-N1-CNL-1L, -3L and in RPM-N1-CNS-1L, -6L as a consequence of having pushed the areas along the boundaries of the moulds too hard towards the bottom of the aluminium cover during mounting in the attempt to reposition the knobs. New replicas, RNM-N1-CNL-4–6, were manufactured in a subsequent batch, in which the positioning knobs were removed from the moulds. The replication process is clearly improved as a result of this alteration in the silicone mould.

RNM-N1-CNL-5 was manufactured from moulds in which the issues with pores, material coming off from the rock specimen and positioning problems of mould in holder had been solved. The deviations with respect to the rock specimen is, both for the lower and the upper parts, within a few hundreds of millimetres, indicating that a very high accuracy can be obtained by employing the presented replica development method.
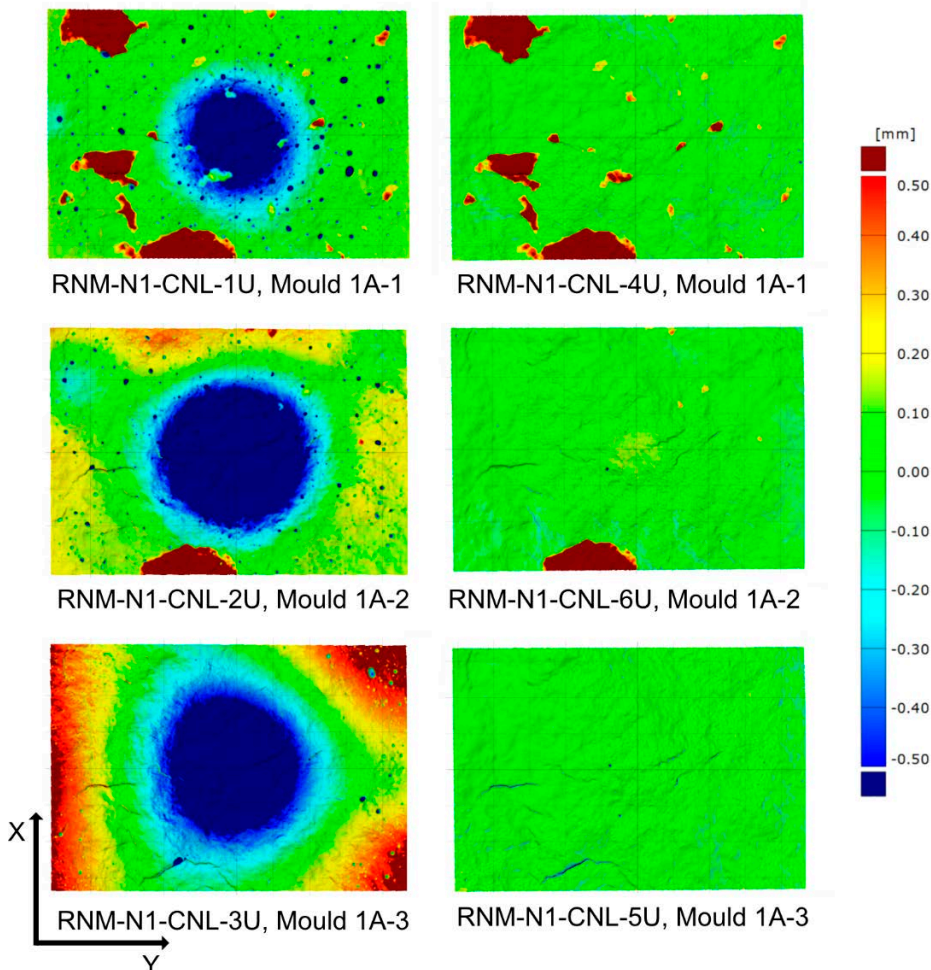


*Figure 4-25.* *Surface comparisons between the mother rock and the replicas with respect to morphology showing deviations in the upper fracture surface. The legend limits are ± 0.5 mm. Upper limit indicates positive deviations corresponding to areas on the replicas laying above the mother rock fracture surface. Larsson et al. (2023a)*

### 4.5.3 Quality assurance parameters

Possible geometric quality assurance parameters with respect to morphology are described in this subsection. The example of a surface comparison shown in Figure 4-23e is a representation of the deviations between two surfaces and not a physical surface. However, since the surface comparisons can be mathematically represented as surfaces it would be possible to investigate the ability of any of the existing surface roughness characterisation methods using statistics or fractals to also describe the deviations between two surfaces. Magsipoc et al. (2020) provide a summary of the most common methods. Firstly, the geometric quality assurance parameters should be derived prior to direct shear testing to evaluate if a replica is approved for direct shear testing, which means that the parameters should be as easy as possible to derive, while still being able to capture the deviations.

The extreme value of the deviation is not suitable measure to use because a single local significant feature, like a pore, would yield a disproportionately large impact and lead to misleading value of the quality to a surface with generally small deviations. Nor would it be suitable to use the mean of the deviations of the coordinate points, since two surfaces with different appearance still could have the same mean. The standard deviation of the deviations of the coordinate points, here denoted $\sigma_{mf}$, potentially could serve as a useful parameter since it reflects the distribution of the morphological deviations. $\sigma_{mf}$ is calculated by means of Equation 4-1:

$$\sigma_{mf} = \sqrt{\frac{1}{N}\sum_{i=1}^{N}(\zeta_i - \overline{\zeta})^2} \tag{4-6}$$

where N is the number of coordinate points, $\zeta_i$ is the deviation value along the evaluation direction for the i:th coordinate point and $\overline{\zeta}$ is the mean of the deviations along the evaluation direction.

Figure 4-26 and Figure 4-27 show $\sigma_{mf}$ with miniatures from the surface comparisons in Figure 4-24 and Figure 4-25. In Figure 4-27, RNM-N1-CNL-3U and -2U could be interpreted to be in reverse order, but the extreme areas in RNM-N1-CNL-2U are of larger magnitude ($-1.65/1.65$) than in -3U ($-1/0.6$), which in both cases are outside the limits of the legend and therefore not displayed. The coordinate points of the replicas deviate significantly from the rock fracture in the areas with the foregoing identified different types of deviations. The impact of these deviations is clearly seen in Figure 4-26 and Figure 4-27. The larger the deviations are, as seen from visual inspection of the surface comparisons, the higher value of $\sigma_{mf}$, which indicates the potential of $\sigma_{mf}$ to capture morphological deviations between rock and replica fractures. Consequently, $\sigma_{mf}$ is a parameter that is simple to derive and easy to interpret and is therefore suggested as the geometric quality assurance parameter to capture morphological deviations. The results show that it is possible to manufacture replicas with $\sigma_{mf} < 0.06$ mm.

It is potentially possible to estimate the impact of each deviation type (pores, circular negative deviations in the centre, fragments of positive deviations and positive deviations along the boundaries) on the geometric quality assurance parameters by adjustment of the mesh (the STL files containing the triangular planes). This can be done by using a mesh editing software by, for each deviation type at a time, adjusting the mesh to the nominal position and then evaluating the impact on the geometric quality assurance parameters. For example, the impact of the missing fragment in RNM-N1-CNL-6U on $\sigma_{mf}$ is clearly distinguishable from Figure 4-27 by comparison with RNM-N1-CNL-5U.
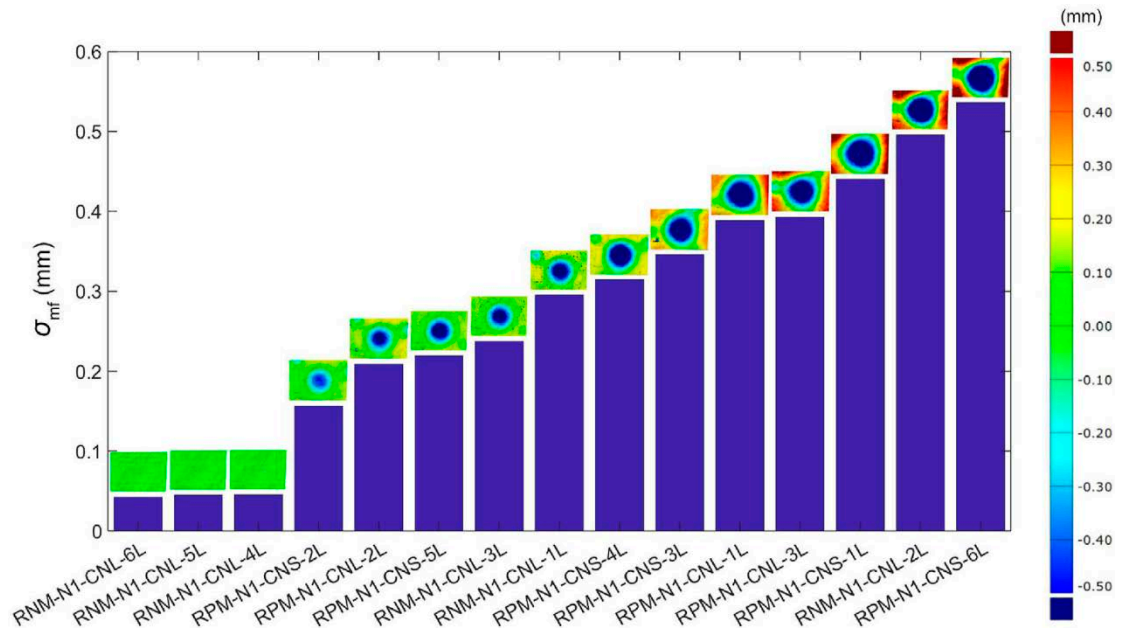
*Figure 4-26.* *Miniatures of surface comparisons with respect to morphology between the lower fracture surface of the mother rock and the replicas along with bars showing σ_mf (from Larsson et al. 2023a).*
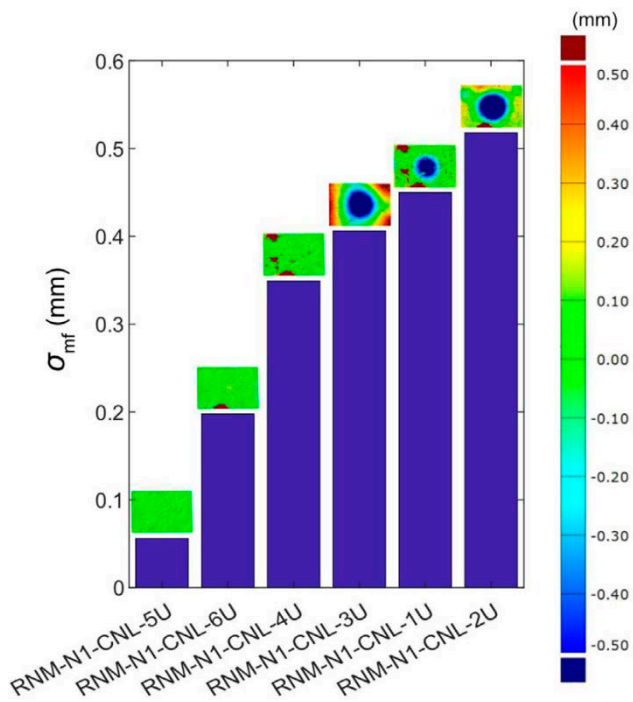


*Figure 4-27.* *Miniatures of surface comparisons with respect to morphology between the upper fracture surface of the mother rock and the replicas along with bars showing σ_mf (Larsson et al. 2023a).*

# 5 Shear test equipment and description of tests

The equipment, testing processes and measured data contained in this section is further described in Flansbjer et al. (2024), Jacobsson et al. (2024b) and Jacobsson et al (2024c).

## 5.1 Development of a large-scale shear test machine

From a review of existing laboratory equipment and as discussed in previous sections, the design and manufacturing of a large-scale shear test machine was necessary to allow for conducting representative direct shear tests in accordance with the requirements of the POST project. A description of the equipment co-developed by RISE, SKB, NWMO and KTH for testing large-scale rock fractures is presented herein and further detailed elsewhere (Jacobsson et al. 2021) (Jacobsson et al. 2023).

This new equipment benefited from an existing 20 MN four-column reaction loading frame located at RISE Research Institutes of Sweden structural laboratory in Borås (Sweden), and its design was based on RISE's prior experience with direct shear tests on crystalline rock fractures (Jacobsson and Flansbjer 2005, Jacobsson et al. 2012) and on the ISRM general recommendations for direct shear tests (ISRM 2007, Muralha et al. 2014). The equipment was designed to be able to perform direct shear tests on specimens up to $400 \times 600$ mm – as retrieved efficiently from deep tunnels by conventional core drilling (300–400 mm diameter) with the fracture plane oriented along the core as in Jacobsson (2016), or alternatively from wire cutting to extract rock blocks – both under high normal stress and stiffness conditions. A novel component of this equipment is the capability to perform direct fracture deformation measurements, both under normal and shear loading, through an optical measurement system based on the Digital Image Correlation (DIC) technique.

### 5.1.1 Normal and shear loading frames

The load in the normal direction is exerted through a 20 MN 4-column testing frame via a spherical joint, as already mentioned. The shear module (Figure 5-1) consists of a lower and upper shear box, a rear block and a load actuator and a bottom plate. The lower shear box is mounted on linear roller bearings to ensure a linear displacement with no rotation. The friction coefficient (rolling resistance) in the linear bearings given by the manufacturer is 0.001 (0.1 %) at a high compressive load. The friction coefficient decreases with increasing compressive force. The upper shear box is kept fixed in position and is attached to a rear block via two bars, one on each side of the upper shear box. The shear actuator is mounted on the rear block. This arrangement constitutes the shear force reaction frame. The largest allowed force in the normal and shear directions are 5 MN and the maximum shear displacement is 70 mm.

The vertical force is measured by oil pressure transducers with an accuracy within 2 %. The horizontal (shear) force is measured by an electrical load cell with an accuracy within 1 %. The load actuators are hydraulic cylinders which are controlled by the control system. The position of the actuators is measured by LVDTs. The force and displacement transducers make it possible to have the actuators in either displacement or force control mode.

Among the design criteria, one requirement was to maintain rock fractures undisturbed (i.e., keep them in their original contact position) during grouting operations of the specimens in the specimen-holders and while mounting specimen holders in the shear boxes. To comply with this limitation, precision-made specimen holders and shear boxes, and the use of linked positioning systems (Figure 5-2) were used during these stages. The specimens are grouted in holders, which are two rectangular boxes with one side open that can be precisely fixated relative to each other using spacers and guide pins. The boxes are manufactured with tight tolerances to minimize geometrical deviations when they are mounted in the shear boxes. Moreover, the system with spacers and guide pins makes it possible to case and fixate a specimen with an undisturbed fracture in the specimen holders. The fracture can then be opened and reassembled to exactly the same initial position. The fractures are then, by definition, disturbed but retrieved to an equivalent undisturbed position. The fracture opening breaks existing rock bridges. The procedure for fixating the specimens in the specimen holder is described in Section 3.3.

Another design requirement implied a high system stiffness (to allow for less stored elastic energy in the test setup) so good controllability of experiments could be obtained in the shear direction, i.e. reducing stress variation at the post-peak stick-slip deformation process and maintaining correct value of normal stiffness in the case of CNS loading condition. To reduce friction in the system during shearing, high-capacity roller bearings were used.
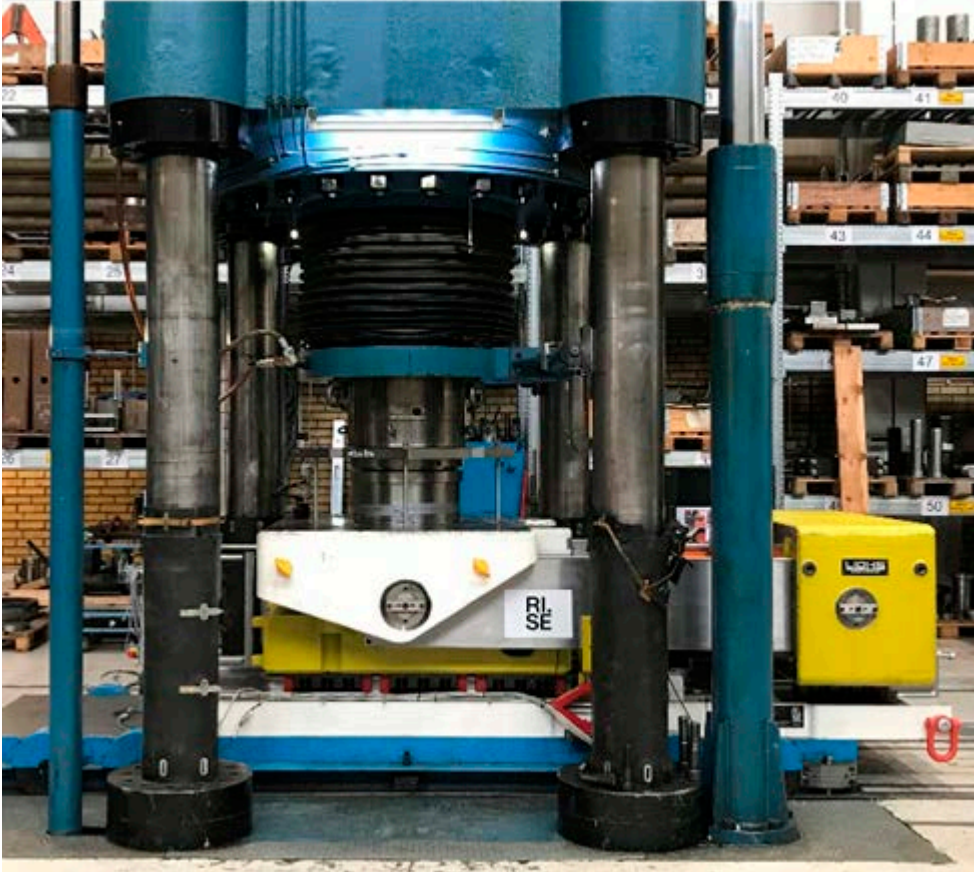


*Figure 5-1. Shear module (yellow/white) and lower part of the four-column load frame.*



*Figure 5-2. Specimen holder standing on a table with the two halves in a fixed relative position.*

## 5.1.2 Displacement and deformation-measurement systems

Fracture displacement measurements can be performed with two systems: a novel optical direct, and a conventional indirect displacement measurement system. The optical direct displacement measurements can be made via a 2D digital image correlation (DIC) technique (Sutton et al. 2009), on images taken by $2\,448 \times 2\,048$ pixels CCD (machine vision) cameras on surface areas (c. $55 \times 45$ mm) on the specimen containing the fracture and subjected to a speckle pattern. The displacement field at four areas – two on the left and two on the right side in the front and rear ends in relation to the shear direction – can be determined. The local normal and shear displacements can also be determined by a 2D virtual extensometer, with an equivalent gauge length between 10–15 mm measuring between two subset points ($25 \times 25$ pixels), positioned at each side of the fracture, and yielding a resolution of approximately 0.3 μm for both normal and shear displacement components.

The relative displacement between the upper and lower shear boxes is measured by LVDTs, placed at four locations in the normal direction to provide information relative to dilatancy, and at two locations in the shear direction giving the shear displacement (Figure 5-3). Roll and pitch measurements can also be obtained with these systems. The LVDTs for the non-local measurements have a measurement range of 100 mm with approximately 1.5 μm resolution in the shear direction and 50 mm with approximately 0.8 μm resolution in the normal direction and an accuracy within 1 %.

The cameras together with lighting, are fixated to the upper shear box, in the gap between the lower and upper box at a working distance (wd) of approximately 100 mm, see Figure 5-4. The cameras are positioned so the x- and y-axis of the image are parallel and perpendicular to the theoretical fracture plane in the machine, respectively. The physical pixel size at each of the four measurement areas is determined by a calibration scale prior test.

To use the non-local measurements to determine the actual fracture displacements yields a lower accuracy since the deformations in the system needs to be subtracted (Jacobsson & Flansbjer 2005). This operation introduces an additional uncertainty. In practice, it means that non-local measurements are severely inaccurate in the small displacement range when fracture stiffnesses are determined but serves well to determine the fracture displacements outside this range. Hence, the local fracture displacement measurements should only be used to determine the fracture stiffnesses.

The gauge length was chosen based on the local geometry of the fracture. The relative error after calibration compared to a mechanical calibrator was within 1.0 %.

The data from the force transducers and LVDTs are sampled by a data acquisition system (DAC). A separate DAC system is used for the DIC measurements since it will control the cameras and store the image files plus data from the force and displacement transducers (LVDTs).
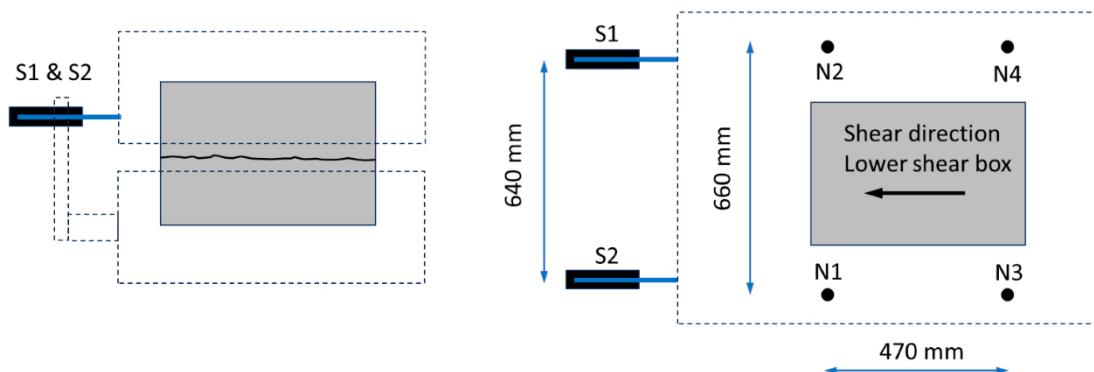


***Figure 5-3.*** *Schematic overview of notations and positions for LVDTs used for the non-local deformation measurements of relative shear box displacements. Left: shear direction (side view); Right: normal direction (top view).*
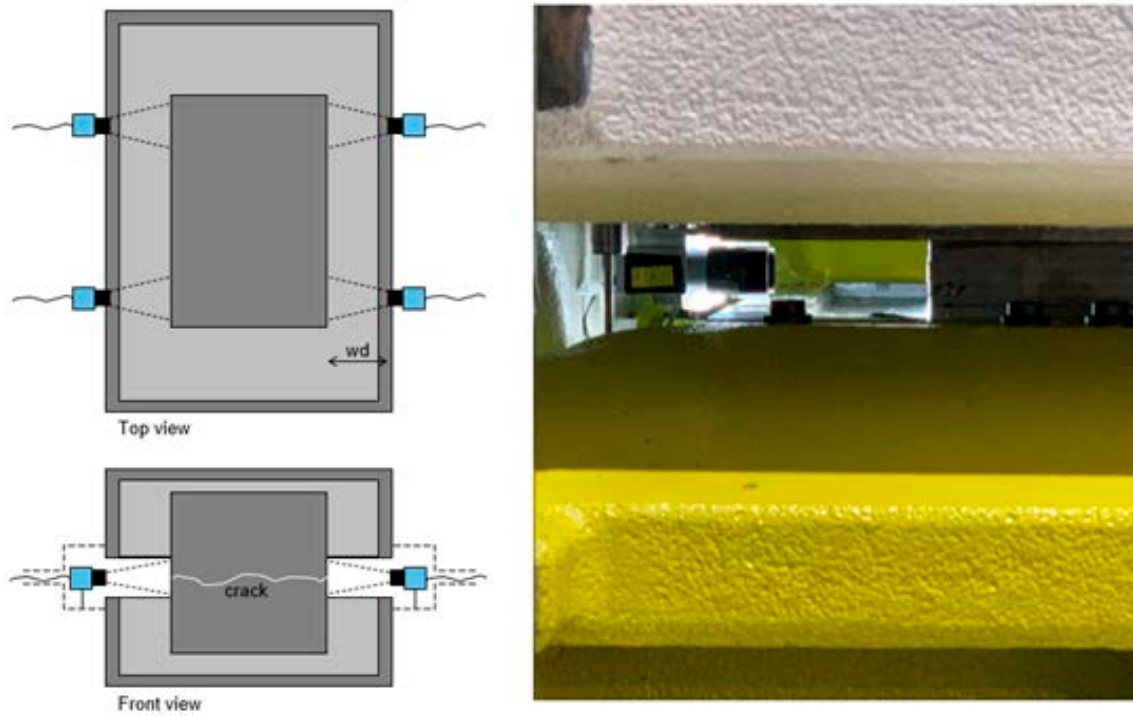
*Figure 5-4. Position of the machine vision cameras used for local deformation measurement system.*
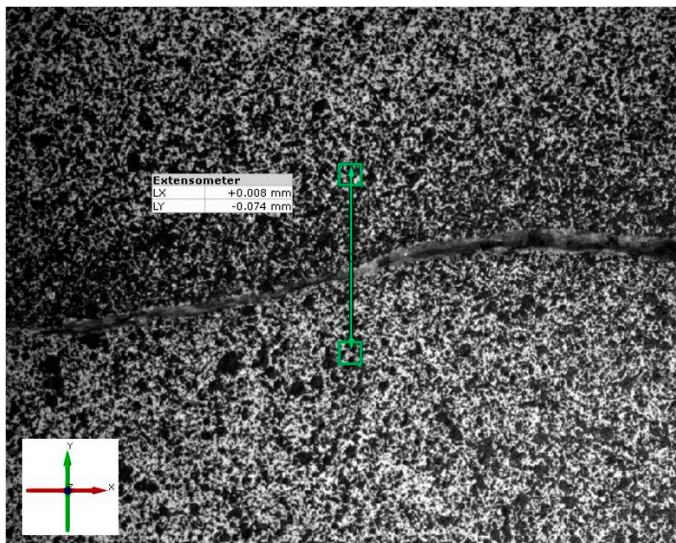


*Figure 5-5. Local direct measurement of fracture displacements by virtual 2D extensometer with the DIC-based measurement method.*

### 5.1.3 Stiffness correction during direct shear tests under CNS loading conditions

Shearing under constant normal stiffness condition (CNS) means that the normal stress $\sigma_N$ depends linearly on the dilation of the fracture, i.e. $\delta_{N,fr}$ for a given idealised rock stiffness $k_N$ (Equation 5-1)

$$\sigma_N = \sigma_{N,0} + \Delta\sigma_N = \sigma_{N,0} + k_N \delta_{N,fr} \tag{5-1}$$

where $\sigma_{N,0}$ is the normal stress before any shearing has taken place and $\Delta\sigma_N$ is the normal stress increment associated with the fracture deformation ($\delta_{N,fr}$). The measured normal displacement by the non-local deformation measurement system $\delta_{N,tot}$ during a loading defined as the summation of fracture deformation $\delta_{N,fr}$ and system deformations $\delta_{N,sys}$ (Equation 5-2).

$$\delta_{N,tot} = \delta_{N,fr} + \delta_{N,sys} \tag{5-2}$$

This means that the fracture dilation cannot be directly estimated from the non-local deformation measurements since some of the deformations during a stress increase will be absorbed as deformations within the system components. The size of the deformations absorbed by the system depends on the system stiffness. Assuming that the system has a linear elastic response with a stiffness $k_{N,sys}$ then (Equation 5-3):

$$\delta_{N,sys} = \frac{\Delta\sigma_N}{k_{N,sys}} \tag{5-3}$$

The system stiffness can be estimated by testing a solid specimen with no fracture deformations $\delta_{N,fr} = 0$ i.e. $\delta_{N,tot} = \delta_{N,sys}$. Then (Equation 5-4):

$$k_{N,sys} = \frac{\Delta\sigma_N}{\delta_{N,tot}} \tag{5-4}$$

Assume now that a certain rock mass stiffness $k_N$ is going to be enforced on a rock specimen during testing then the applied normal stiffness given to the testing system (Equation 5-5)

$$k_{N,eff} = \frac{\Delta\sigma_N}{\delta_{N,tot}} \tag{5-5}$$

must be larger to compensate for the deformations absorbed by the test setup (Larsson and Flansbjer 2020), i.e. (Equation 5-6),

$$k_{N,eff} = k_N \left(1 - \frac{k_N}{k_{N,sys}}\right)^{-1} \tag{5-6}$$

which is obtained by combining Equations 5-1 to 5-5.

Experiments were conducted to determine the system normal stiffness, $k_{N,sys}$ according to (Equation 5-4). The normal stiffness was measured using the steel specimen that was subjected to normal loading cycles. Three loading cycles were conducted, 75–750 kN, 75–1 800 kN and 75–4 500 kN. The normal secant stiffness was evaluated in two different intervals, 85–745 kN and 750–3 925 kN. The loading curves and the secant evaluations are shown in Figure 5-6 and Figure 5-7.
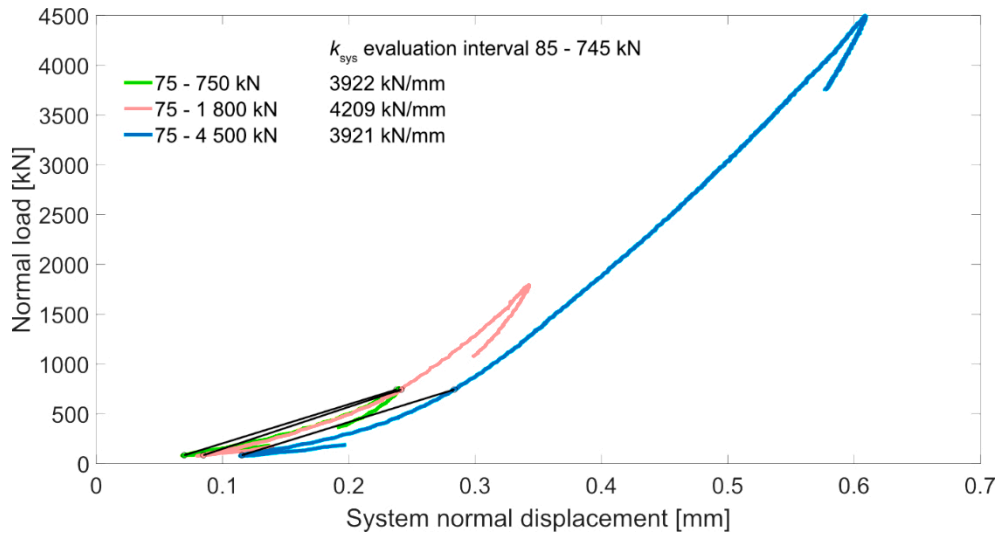
***Figure 5-6.*** *Normal loading response and evaluated secant stiffnesses for three load ranges (© (Larsson, 2021) CC–BY 3.0 https://creativecommons.org/licenses/by/3.0/).*
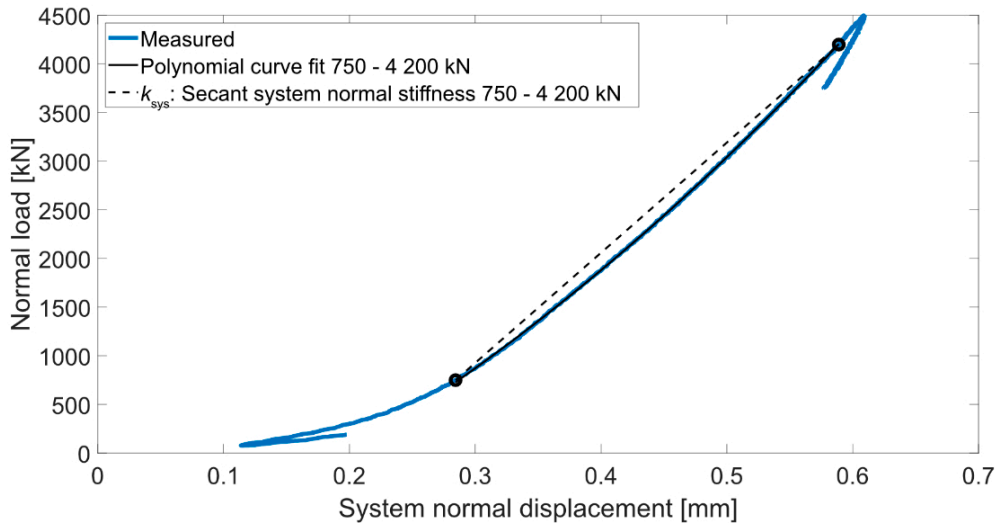


***Figure 5-7.*** *Normal loading response and evaluated secant stiffness for one load range (© (Larsson 2021) CC–BY 3.0 https://creativecommons.org/licenses/by/3.0/).*

The measured stiffness in the loading range representative for the experiments was found to be 11.326 kN/mm and recalculated to stress given an area of 300 mm × 500 mm yields $k_{N,sys}$ = 75.51 MPa/mm. In the given experiments, the simulated normal stiffness of the rock mass is 10 MPa/mm, which yields that applying $k_{N,eff}$ = 11.53 MPa/mm during the experiments will give the desired simulated rock mass stiffness. The reader is referred to (Larsson 2021) for further details regarding an uncertainty estimation of the linear stiffness approximation of the system stiffness given by the computed secant.

## 5.2 Shear test machine for medium- to small-size specimens

### 5.2.1 Loading frame

The normal loading and shear tests were performed in a servo hydraulic testing machine aimed for shear tests, see Figure 5-8. The machine is supplied with two shear boxes, one upper and one lower. The upper box can be moved vertically and the lower box horizontally. Two actuators, one acting vertically and one acting horizontally, are used to apply the forces in the two directions (degrees of freedoms). Two linear bearings are guiding the lower box to obtain a controlled linear movement. The maximum stroke is 100 mm in the vertical direction and ± 50 mm in the shear direction.

The maximum vertical (normal) force that can be applied is 300 kN and the maximum load in the horizontal (shear) direction is ± 300 kN. Electrical load cells are used to measure the forces in normal ($F_N$) and shear directions ($F_S$), respectively. The accuracy of the load measurements is within 1 %. The machine is connected to a digital controller with a computer interface for setting up and running tests. It also contains a sampling unit where the test data is recorded.

### 5.2.2 Displacement and deformation measurement systems

Two types of systems are used for displacement measurements. The first type is the ordinary conventional system based on LVDTs which measures relative displacements between the upper and lower shear box. The measurements contain the fracture displacements plus the deformations in all components and material away from the fracture (rock material, concrete, steel holders and shear boxes). This is denoted a *non-local* fracture displacement measurement.



*Figure 5-8. Equipment for direct shear tests and digital controller unit.*

The vertical relative displacement between the shear boxes, $\delta_{N,LVDT}$, is measured by four LVDTs, $\delta_{N,LVDT1}, \ldots, \delta_{N,LVDT4}$, positioned in a square pattern around the specimen, one in each corner. Each of the LVDTs has a measurement range of 5 mm and a relative error less than 1 %.

The relative displacement between the shear boxes in the horizontal (shear) direction, $\delta_{S,LVDT}$, is measured by one LVDT, which has a 25 mm range and a relative error less than 1 %.

The second system type measures the fracture displacement directly on the specimen surface at two locations across the fracture, one on each side at the specimen centre, using a non-contact optical method by a 2D digital image correlation (DIC) technique (Sutton et al. 2009). This is a novel way to measure the *local* fracture displacements. The measurements are done using machine vision CMOS cameras on surface areas (c 15 mm × 13 mm) of the specimen containing the fracture. Since, the cameras cannot access the side of the specimens due to the machine frame, the cameras are instead oriented in the shear direction and the light path is going through a 45 degrees prism to deflect the light path 90 degrees towards each side of the specimen. A picture of the measurement configuration is shown in Figure 5-9. The natural grain pattern at the specimen surface is used to get a reference for the facets (group of pixels) which are used for the determination of the displacement field (the usual speckle pattern was not created on the specimen surface). The physical pixel size was approximately 6 μm and was determined at each of the two measurement areas by a calibration scale prior to the test. The local relative displacement in normal, $\delta_{N,DIC1}$ and $\delta_{N,DIC2}$ and shear direction, $\delta_{S,DIC1}$ and $\delta_{S,DIC2}$, were determined by a 2D virtual extensometer, with an equivalent gauge length between 3–5 mm measuring between two subset points (41 × 41 pixels), positioned at each side (side 1 and 2) of the fracture, yielding a resolution of approximately 0.1 μm for both normal and shear displacement components. The gauge length was chosen based on the local geometry of the fracture. The relative error after calibration compared to a mechanical calibrator was within 1.2 %.

The data from the force transducers and LVDTs are sampled by a data acquisition system (DAC). A separate DAC system is used for the DIC measurements since it will control the cameras and store the image files plus data from the force and displacement transducers (LVDTs).

The local (DIC-based) deformation measurement system was added after the initial tests on rock specimens and all replica specimens of a natural rock fracture were tested. Hence, the local deformation measurement system was in place at the test of all specimens in the small scale plus three rock specimens with tensile induced fractures.
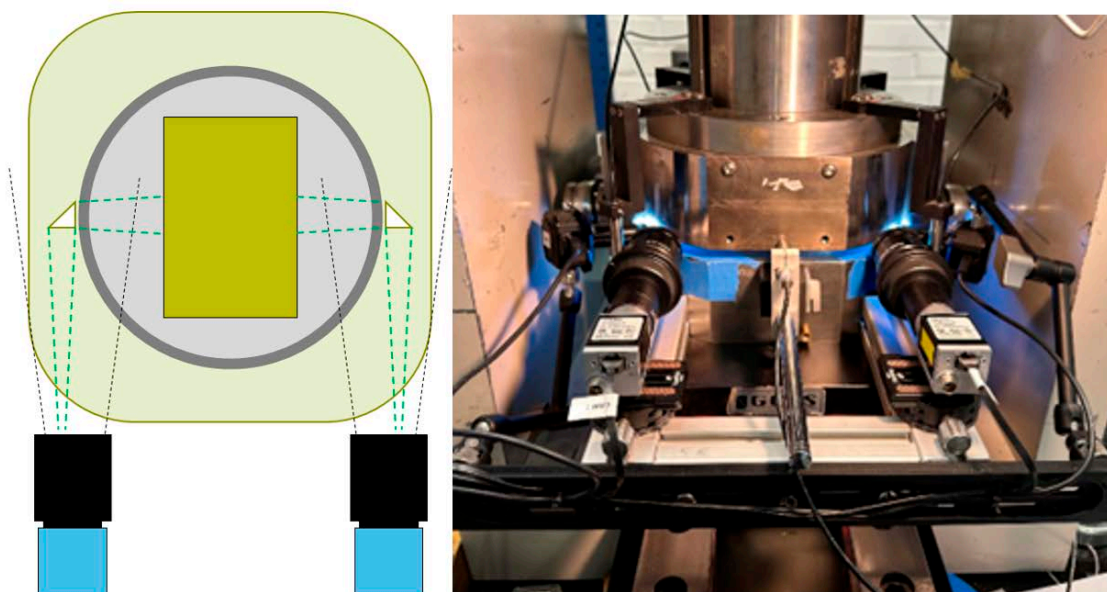


***Figure 5-9.** Placement of cameras and prisms for the non-local measurements based on DIC. The green dashed lines illustrated the light path used for the measurements.*

### 5.2.3 Stiffness correction during CNS loading conditions

The formulation for stiffness correction during tests on medium- and small-size fractures under CNS loading conditions was similar to same as that presented in Section 5.1.3 (Equations 5-1 to 5-6).

Experiments were conducted to determine the system normal stiffness $k_{N,sys}$ according to (Equation 5-4). The normal stiffness was measured using the two steel specimens, 35 mm × 60 mm, and 100 mm × 100 mm, that were subjected to normal loading cycles and evaluated in the intervals 5–13 MPa and 5–10 MPa yielding the stiffness values $k_{N,sys}$ = 153 MPa/mm (35 mm × 60 mm) and $k_{N,sys}$ = 61.9 MPa/mm (100 mm × 100 mm).

The normal stiffness of the rock mass was estimated to be 10 MPa/mm based on the elastic properties of the rock mass at Forsmark, and this stiffness was simulated as a constant value in the laboratory shear tests on the fracture samples. Hence, by applying $k_{N,eff}$ = 10.7 MPa/mm (35 mm × 60 mm) and $k_{N,eff}$ = 11.9 MPa/mm (70 mm × 100 mm) will give the desired simulated normal stiffness of the rock mass.

## 5.3 Normal loading and direct shear test

### 5.3.1 Normal loading test

#### General description

The prepared and characterised specimens are installed in the testing machine with the two specimen halves matched to each other. The shear position control is set to zero, and the shear displacement control is kept active during the following normal loading cycles. After mounting and checking all sensors, the contact pressure measurement is carried out followed by the normal loading test. Four load cycles 0.5–12 MPa with a normal loading and unloading rate of 10 MPa/min are carried out whereby the normal loading test is completed. An overview of the activities during the normal loading test is shown in the step-by-step description in Table 5-1.

**Table 5-1. Activities during the normal loading test.**

| Step | Activity |
|------|----------|
| 1 | Mount the lower specimen holder containing one half of the specimen in the test machine |
| 2 | Place the AE-sensors towards the specimen side and check the signal (only 70 mm × 100 mm specimens) |
| 3 | Mount the upper specimen holder containing the other specimen half in the test machine |
| 4 | Conduct the contact pressure distribution measurement (Section 4.4) |
| 5 | Check all LVDTs and the optical measurement system |
| 6 | Perform the normal loading tests with four load cycles up to 12 MPa. Zero the channels for the normal deformation measurement before the test at 0.5 MPa normal stress. The specified loading/unloading rate is 10 MPa/min. |
| 7 | Store the test results on the computer network |

#### Interpretation

The results of the normal loading tests with direct deformation measurement are represented by normal stress-normal deformation relations (see, i.e., Figure 6-1).

The fracture deformation in the normal direction, $\delta_N$, is defined as the average value

$$\delta_N = \frac{\delta_{N,1} + \delta_{N,2} + \delta_{N,3} + \delta_{N,4}}{4}$$

where parallel measurements were made using both the non-local indirect deformation measurements by LVDTs and by the local direct deformation measurements by DIC at four measurement positions. The DIC measurements were made over a gauge length approximately varying between 15–25 mm.

The normal stress $\sigma_N$ is defined as

$$\sigma_N = \frac{F_N}{A}$$

where $F_N$ is the normal force acting on the fracture and $A = L \cdot W$ is the area of the fracture.

The secant normal stiffness $K_N$ was determined at two states, namely: as the secant evaluated between 0.5 MPa (unloaded state) and 12 MPa (full loading), denoted $K_{N05}$, and between 4 MPa and 12 MPa, denoted $K_{N4}$, belonging to the loading path during the fourth load cycle by local direct deformation measurements by DIC, i.e. $K_N = \frac{\Delta \sigma_N}{\delta_{N,DIC}}$.

## 5.3.2 Direct shear test

### *General description*

The direct shear test was carried out directly after the normal loading test. The specimen is first subjected to a normal stress of 0.5 MPa, where after the sensors are set to zero. The normal loading is increased to specified initial normal stress at a loading rate of 10 MPa/min. On the next step, the shear displacement is imposed at a rate of 0.5 mm/min under either CNL or CNS condition. The prescribed CNS value is 10 MPa/mm, but a value of 11.5 MPa/mm is inserted in the control system that compensate for the system deformations in the normal direction (Section 5.2.3). The shear loading is stopped when the shear displacement is 6 mm (35 mm × 60 mm), 10 mm (70 mm × 100 mm), or 50 mm (300 mm × 500 mm). The normal and shear displacements were recorded by both the non-local (LVDTs) and local (optical) deformation measurement system. An overview of the activities during the shear test is shown in the step-by-step description in Table 5-2.

**Table 5-2. Activities during the direct shear test.**

| Step | Activity |
|------|----------|
| 1 | Apply a normal stress of 0.5 MPa and zero the deformation channels |
| 2 | Increase the normal stress to 5 MPa at a loading rate of 5 MPa/min |
| 3 | Apply a shear deformation with a rate of 0.5 mm/min and shear until the shear displacement reaches, for large-size fractures (300 mm × 500 mm), 50 mm or the normal stress reaches approximately 33 MPa; for medium-size fractures (70 mm × 100 mm), 10 mm, and for small-size fractures(35 mm × 60 mm): 6 mm. |
| 4 | For large-size fractures, unload the normal stress maintaining the position of the shear box. For medium- and small-size fractures, unload the shear stress, and then unload the normal stress. For the large-size fractures, to maintain stability in the control system, the shear stress could not be unloaded under normal stress. |
| 5 | Reset the displacement to zero |
| 6 | Take out the specimens from the test machine |
| 7 | Take digital photos of each specimen |
| 8 | Scan the fracture surfaces |
| 9 | Store the test results on the computer network |

### *Interpretation*

In the shear tests, the shear deformation $\delta_S$ is represented by the relative displacement across the fracture between the upper and lower part of the specimen and is defined as the average value

$$\delta_{S,LVDT} = \frac{\delta_{S,LVDT1} + \delta_{S,LVDT2}}{2}$$

and

$$\delta_{S,DIC} = \frac{\delta_{S,DIC1} + \delta_{S,DIC2} + \delta_{S,DIC3} + \delta_{S,DIC4}}{4}$$

where $\delta_{S,DIC1}, \ldots, \delta_{S,DIC4}$ are displacements recorded by the DIC measurement system at the four measurement locations and $\delta_{S,LVDT1}$ and $\delta_{S,LVDT2}$ are the measured values from the two LVDTs. The normal deformation $\delta_N$ is defined as in the normal loading test.

The normal stress $\sigma_N$ and shear stress $\sigma_S$ are defined as

$$\sigma_N = \frac{F_N}{A} \text{ and } \sigma_S = \frac{F_S}{A}$$

where $F_N$ is the normal force and $F_S$ is the shear force acting on the fracture and

$$A(\delta_{S,LVDT}) = (L - \delta_{S,LVDT})W$$

is the actual fracture area for a given shear displacement where $W$ is the width of the specimen.

The secant shear stiffness $K_S$ is determined as the secant evaluated for a shear stress $\sigma_S$ between 1 and 5 MPa.

The shear stress at fully mobilised shear slip $\sigma_{S,s}$ is determined as the shear stress value when a clear plateau in the shear stress versus displacement curve is reached. In most cases this is clearly seen as it coincides with a clear peak. In a few cases during the CNS tests, it is followed with an increase of shear stress at further shearing. In those cases, the plateau is defined as the portion with almost constant shear stress and just prior to shear stress oscillations due to a clear stick-slip behaviour which starts at about 0.3–0.4 mm shear displacement ($\delta_{S,DIC}$).

The peak shear strength $\sigma_{S,p}$ is defined only for the CNL specimens as the maximum value during the whole shear cycle.

The residual shear strength $\sigma_{S,r}$ is determined at the last 5 mm of the shear displacement of the shear cycle. The measured shear stress is fluctuating up and down caused by a progressing stick-slip response that occurs during the shear process due to a limited shear stiffness in the test system and uneven fracture surfaces in the fractures (Figure 5-10).

The actual shear strength in the fracture is characterised by the stress when the slip re-starts which equals to the stress at sub-peak points before the stress drops. The residual stress value is approximated as the mean value of the stress at sub-peak points over an evaluation distance. The evaluation principle is illustrated in Figure 5-11.

The secant dilation angle $\psi$ is determined for the three fracture sizes as the slope $\delta_{N,LVDT}/\delta_{S,LVDT}$ evaluated for a shear displacement interval (residual stage), $\delta_{S,LVDT}$ 1–4 mm for the small and medium size fractures, and 1–8 mm for the large rock fractures
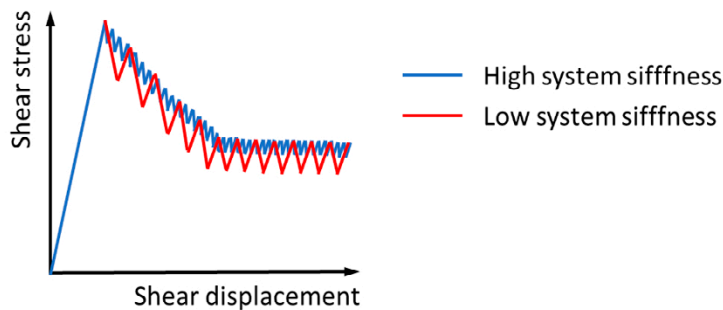


**Figure 5-10.** *Effect of a high and low system stiffness in the shear direction on the shear response of a CNL test.*
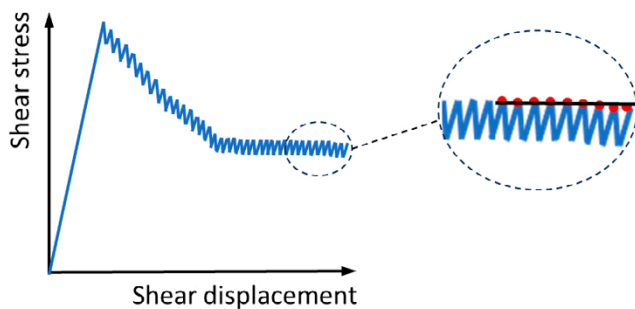


**Figure 5-11.** *Principle for the evaluation of the residual shear stress $\sigma_{S,r}$ (black line in the close-up) on a CNL test. Red points visualize the sub-peak points.*

# 6 Results from normal loading and direct shear tests

The results from the normal loading and direct shear tests on replicas and rock fractures contained in this Section are based on Flansbjer et al. (2024), Jacobsson et al. (2024b) and Jacobsson et al. (2024c). The three reports contain additional material such as more detailed presentation of the results.

## 6.1 Normal loading tests

Normal loading tests consisted in compressing the fractures. This yielded a progressive closure (decreasing fracture aperture), which partly reversed during unloading. The procedure is described in Section 5.3.1.

The goal was to measure the normal stiffness of the fractures with the two fracture surfaces in a matched position such that the asperities, constituting the roughness of the fracture surfaces, fits into each other as good as possible. In practice, there are several factors that control the behaviour of two fracture surfaces in contact, such as the actual fracture surface geometry and rock material properties itself, but also induced experimental imperfections. For a newly created tensile rock fracture, there will still be small geometrical differences between the two surfaces such that they do not perfectly fit to each other. It can be due to some residual stress within the rock material that are released (de-stressed) or that micro-cracks were developed at the fracture surfaces when the fracture was opened. When the fracture is closed, these imperfections in mismatch of a tensile induced fracture will result in a poorer match of the whole surface and additional contacts between small-scale asperities. The contact forces at these contact points (normal and frictional) will yield a resistance for the fracture to close, resulting in a slightly less stiff fracture compared to a perfectly matched one. For a natural fracture, with a poorer match than a tensile induced fracture, the contact points will be fewer and larger, resulting in a lower stiffness compared to the tensile induced fracture.

There are, in addition, imperfections given by the experimental procedure yielding an initial state with slightly disturbed positions of the fracture surfaces relative to each other caused by undesired translations and rotations. Depending on their magnitude, the fractures can, to a varying degree, find their way back to each other to obtain perfect fit. Finally, the asperities may be damaged by the contact pressure measurements and there may be some tiny debris left on the fracture surfaces, in spite of careful cleaning to remove loose debris. All these imperfections will add on to a non-linear behaviour and a frictional induced hysteresis during the loading and reloading cycles.

Results for normal stiffness calculations can be found both for natural and tensile-induced fractures, for large-size specimens in Table 6-1, for medium-size specimens in Table 6-2, and for small-size specimens in Table 6-3. Additionally, results for normal loading tests on replicas are presented in a separate Section 6.2.1 and represented in Figure 6-4.

### 6.1.1 Large-size rock specimens

Concerning the normal loading tests performed on large-size rock fractures, all displayed a stress displacement behaviour in the normal direction, which showed a fair-to-good matching. An example of a test performed on specimen N1-L-CNS is shown by Figure 6-1, with differences in the normal displacement that can be seen for the two measuring systems used (non-local or local). In general terms, any or a very small shear-induced displacements ($\leq 0.09$ mm) were observed during the normal loading experiments, which yielded a small shear stress ($< 0.2$ MPa). For further detailed information regarding specific normal loading tests on large-size fractures, the reader is referred to (Jacobsson et al. 2024).

Normal stiffness results that according to Section 5.3.1 are $K_{N05}$ and $K_{N4}$, are presented in Table 6-1 as retrieved from local measurements (DIC) on the normal loading tests on large-size fractures.
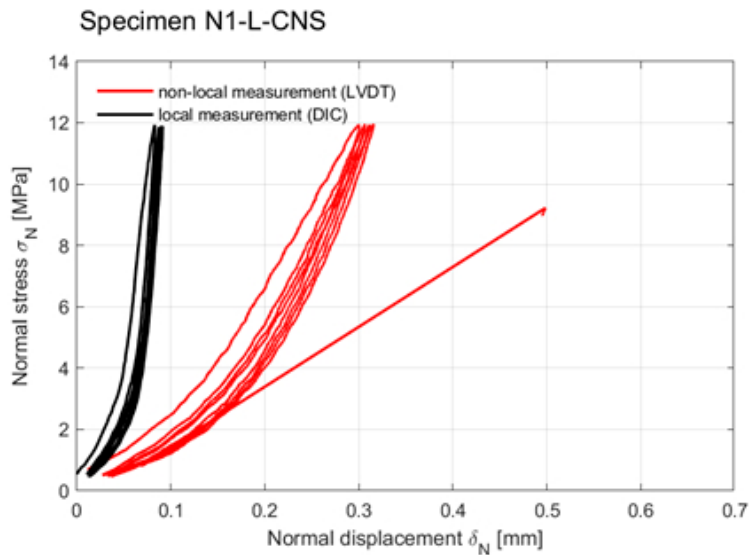
**Figure 6-1.** *Normal stress versus normal displacement for a fracture with an initial good (perfect) matching.*

**Table 6-1. Normal stiffness values for large-size fractures as retrieved from normal loading tests (results obtained from local deformation measurements (DIC)).**

| Specimen ID | $\sigma_{N0}$ [MPa] | $k_N$ [MPa/ mm] | $K_{N05}$ [MPa/mm] | $K_{N4}$ [MPa/mm] |
|---|---|---|---|---|
| N1-L-CNS | 5 | 10 | 152 | 321 |
| N2-L-CNS | 5 | 10 | 170 | 312 |
| N3-L-CNS | 5 | 10 | 185 | 364 |
| TI1-L-CNL | 5 | 0 | 168 | 393 |
| TI2-L-CNL | 5 | 0 | 240 | 495 |
| TI3-L-CNL | 5 | 0 | 240 | 548 |
| N1-L-CNL | 5 | 0 | 370 | 637 |

### 6.1.2  Medium-size rock specimens

In what refers to the medium-size rock specimens, local fracture displacement measurements were only conducted on three specimens (TI2-M-CNL, TI3-M-CNL and TI4-M-CNS). The normal stress-displacement response indicates that the matching was good with a response similar to the small-size specimen test presented in Figure 6-2. The shear displacement was not measured on all specimens during the loading stage. The missing measurements are on specimens TI6-M-CNS, N1-M-CNL, N2-M-CNL, N3-M-CNL, N4-M-CNL and N6-M-CNL. All specimens with measured shear displacements showed only a very small shear displacement during the normal loading stage. Consequently, there was no induced shear stress during the normal loading stage except for specimen N6-M-CNL, which showed an induced shear stress up to 0.4 MPa. Unfortunately, this specimen was one of those with missing shear displacement measurements.

The normal stiffness was measured on three specimens with tensile induced fractures in the $70 \times 100$ mm size and showed high stiffnesses, ca. 1 600, 1 600 and 3 200 MPa/mm. For further detailed information regarding specific normal loading tests on medium-size fractures, the reader is referred to Jacobsson et al. (2024b).

### 6.1.3  Small-size rock specimens

Regarding the small-size rock specimens, two graphs (presented in Figure 6-2 and Figure 6-3) were selected from the test series of the small-scale specimens to illustrate different behaviours. The results from the tests of N6-S-CNS (Figure 6-2) show an initially good (perfect) matched fracture yielding an instant increase of normal stress when the fracture is compressed (increased normal displacement). There is an initial non-linearity which gradually vanishes yielding an apparent stress-displacement

linear response at higher stress. The fracture stiffness is high. On the other hand, Figure 6-3 shows the results from the tests of N10-S-CNL which corresponds to a poorly matched fracture. The hysteresis is larger for this test during the loading-unloading cycles than the perfectly matched surfaces shown in Figure 6-2. The gradual settlement is also larger. In this case, the fracture stiffness is low. For further detailed information regarding specific normal loading tests on small-size fractures, the reader is referred to Jacobsson et al. (2024b).

The measured secant normal stiffness in the interval 4–12 MPa ($K_{N4}$) showed a large variation for the 35 × 60 mm specimens with natural fractures. The stiffness was approximately in the range 100–1 500 MPa/mm with five of 12 specimens in the range 800–1 500 MPa/mm. The variation was also large for the corresponding specimens in the same size with tensile induced fractures. The stiffness was approximately in the range 350–1 100 MPa/mm with 6 of 12 specimens in the range 800–1 100 MPa/mm.

A summary of results for normal stiffness for medium- and small-size fractures is provided in Table 6-2 and Table 6-3.
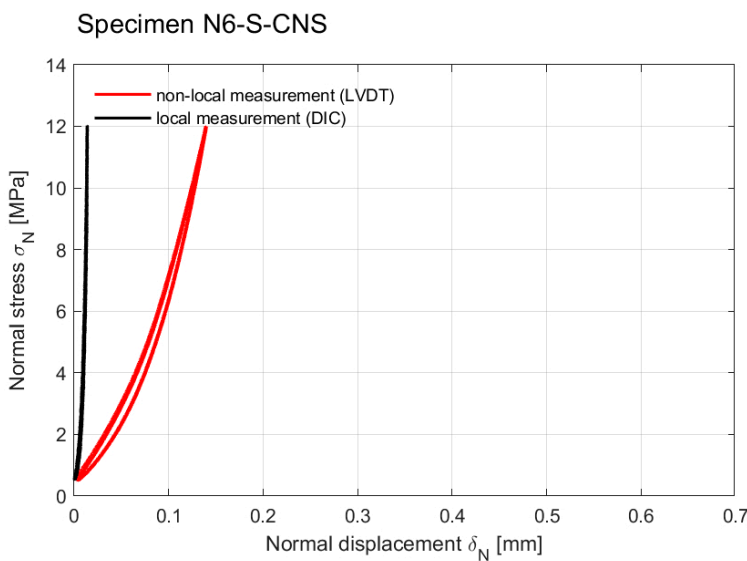


*Figure 6-2.* *Normal stress versus normal displacement for a small-size fracture with an initial good (perfect) matching.*
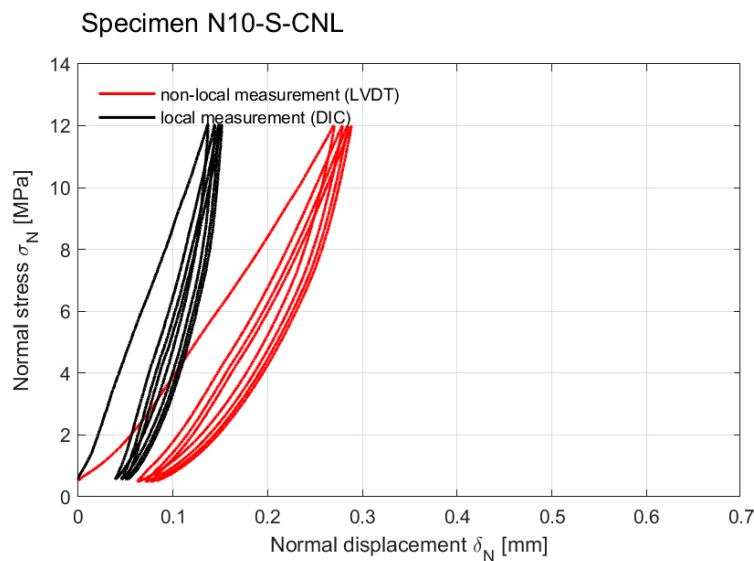


*Figure 6-3.* *Normal stress versus normal displacement plot for a small-size fracture with natural (poor) matching, low normal stiffness and a large hysteresis.*

**Table 6-2. Normal stiffness values for medium-size fractures as retrieved from normal loading tests (results obtained from local deformation measurements (DIC).**

| Specimen ID | $\sigma_{N0}$ [MPa] | $k_N$ [MPa/ mm] | $K_{N05}$ [MPa/mm] | $K_{N4}$ [MPa/mm] |
|---|---|---|---|---|
| TI2-M-CNL | 5 | 0 | 1 270 | 3 160 |
| TI3-M-CNL | 5 | 0 | 796 | 1 630 |
| TI4-M-CNS | 5 | 10 | 635 | 1 590 |

**Table 6-3. Normal stiffness values for small-size fractures as retrieved from normal loading tests (results obtained from local deformation measurements (DIC).**

| Specimen ID | $\sigma_{N0}$ (MPa) | $k_N$ [MPa/ mm] | $K_{N05}$ [MPa/mm] | $K_{N4}$ [MPa/mm] |
|---|---|---|---|---|
| N1-S-CNS | 5 | 10 | 507 | 820 |
| N2-S-CNS | 5 | 10 | 581 | 925 |
| N3-S-CNS | 5 | 10 | 372 | 728 |
| N4-S-CNS | 5 | 10 | 631 | 1 040 |
| N5-S-CNS | 5 | 10 | 561 | 1 140 |
| N6-S-CNS | 5 | 10 | 872 | 1 730 |
| N7-S-CNL | 5 | 0 | 249 | 364 |
| N8-S-CNL | 5 | 0 | 254 | 392 |
| N9-S-CNL | 5 | 0 | 378 | 573 |
| N10-S-CNL | 5 | 0 | 113 | 123 |
| N11-S-CNL | 5 | 0 | 534 | 999 |
| N12-S-CNL | 5 | 0 | 384 | 764 |

### 6.1.4 Replicas

Normal loading tests were also conducted on replica fractures until a 5 MPa normal stress level was attained. Results for tests on RPM-N1-CNL-(1-3), RNM-N1-CNL-(1-3), and RNM-n1-CNL-(4-6) are presented in Figure 6-4, together with result for rock fracture N1-CNL.
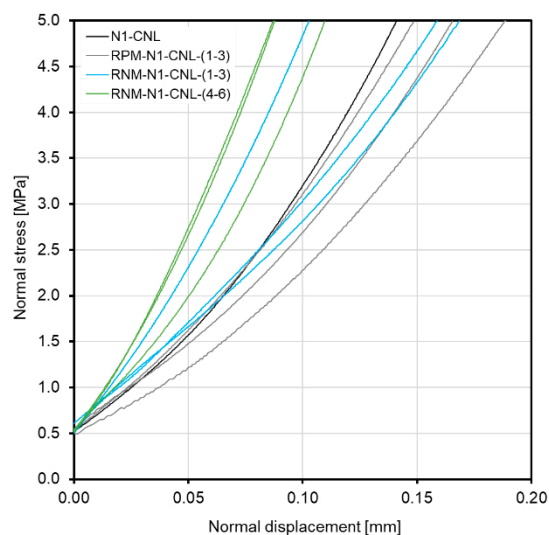


*Figure 6-4. Normal stress versus normal displacement for N1-CNL and replica fractures tested under CNL conditions.*

## 6.2 Direct shear tests

The direct shear tests were done with an initial normal loading of $\sigma_{N0}$ = 5 MPa. The simulated rock mass stiffness $k_N$ was 0 MPa/mm during the CNL tests, and 10 MPa/mm during the CNS tests. In this section, results from direct shear tests performed on rock specimen fractures with the three different sizes (large, medium and small) are presented for both natural and tensile-induced fractures, for the two types of test boundary conditions (CNL and CNS). The results from the shear tests are presented in figures showing how shear stress vs. shear displacements and normal displacements vs. shear displacements develops during the tests, and the results are summarized in tables for the three sample sizes and the replicas. For additional results, such as the development of normal stresses during the CNS tests, see the internal reports from RISE (Jacobsson et al. 2024a, b; Flansbjer et al. 2024).

### 6.2.1 Large-size rock specimens

***Results for tests under CNL conditions***

Four (4) direct shear tests were performed on large-size fractures (300 mm × 500 mm), as initially described in Table 2-1, under CNL conditions. Within this group, one test was performed on a natural fracture (N1-L-CNL), and three tests were conducted on tensile-induced fractures, namely, TI1-L-CNL, TI2-L-CNL and TI3-L-CNL. Shear stress and normal displacement are both plotted versus shear displacement for these four tests in Figure 6-5 and Figure 6-6.

In Figure 6-5, the observed shear stress at fully developed shear slip was 5.95 MPa for the natural fracture and in the range of 9.9 to 10.5 MPa for the tensile-induced fractures. From Figure 6-6, it can be observed that the dilation was almost constant during the whole shear range for both fracture types, yielding a value of about 4.7 mm for the natural fracture at about 47 mm of shear displacement, and between 2.5 to 4.0 mm for tensile-induced fractures for shear displacements in the range of 20 to 37 mm. Negative values in the vertical axis correspond to fracture opening (upward vertical displacements). Secant dilation angles were determined according to Section 5.3.2, with values 6.74° (natural fracture), and 12.3°, 14.4°, and 10.5° (tensile-induced fracture).
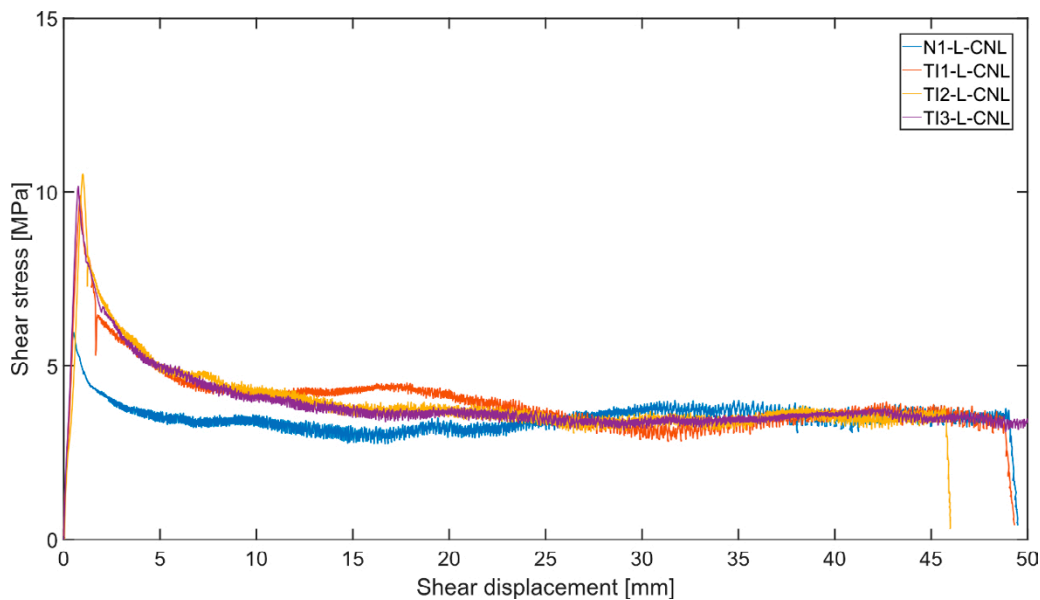


***Figure 6-5.*** *Shear stress results plotted versus shear displacement, for the natural (N) and tensile-induced (TI) large-size fractures tested under CNL conditions (displacement results retrieved from non-local LVDT measurements).*
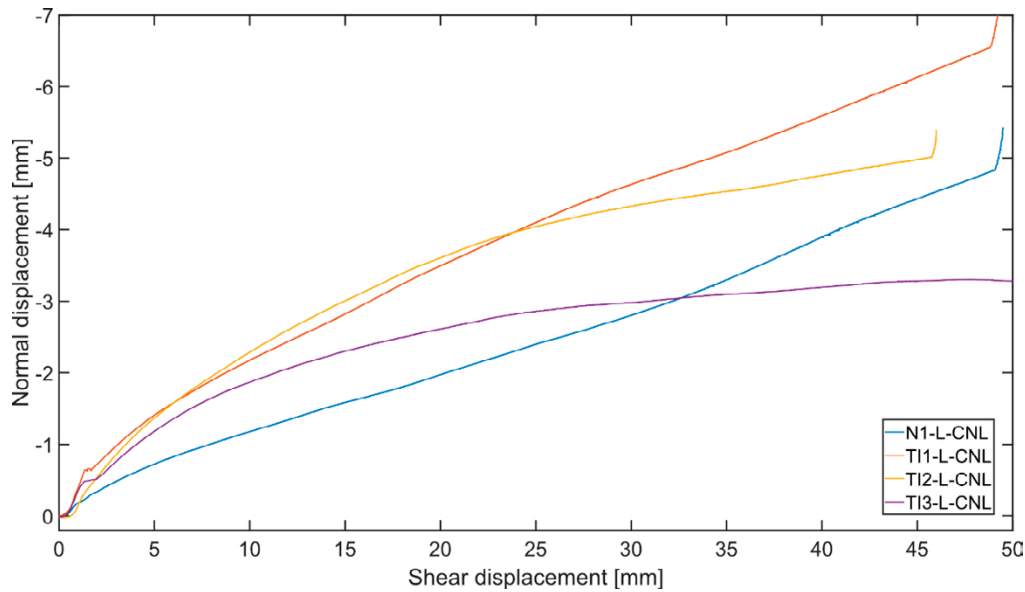
**Figure 6-6.** *Normal displacement plotted versus shear displacement, for the natural (N) and tensile-induced (TI) large-size fractures tested under CNL conditions (displacement results retrieved from non-local LVDT measurements).*

During shear, it was observed that a large piece of the specimen was teared off the rear end of one of the specimen halves (in relation to the shear direction) during the test on specimen TI1-L-CNL at the peak shear strength. The wedge formed piece of rock was in contact with the grouting material at the upper and lower shear boxes seen as scratch marks on the concrete surfaces. It is not known which effect this had on the measurements. A reinforcement of the rear end of the specimens was made on the subsequent specimens reducing the tensile breakages. Regarding the residual shear strength, it was in the range of about 3.6 to 3.8 MPa for both natural and tensile-induced fracture types.

A summary of the results from these tests can be found in Table 6-4, following the nomenclature specified in Section 5.3.2.

**Table 6-4. Summary of results from direct shear tests on large-size natural and tensile-induced fractures under CNL conditions.**

| Specimen ID | $\sigma_{N0}$ [MPa] | $K_s$ [MPa/mm] | $\sigma_{S,s}$ [MPa] | $\sigma_{S,p}$ [MPa] | $\sigma_{S,r}$ [MPa] | $\Psi$ [deg] |
|---|---|---|---|---|---|---|
| N1-L-CNL | 5 | 71.8 | 5.95 | 5.95 | 3.77 | 6.74 |
| TI1-L-CNL | 5 | 195 | 9.90 | 9.90 | 3.81 | 12.3 |
| TI2-L-CNL | 5 | 153 | 10.5 | 10.5 | 3.71 | 14.4 |
| TI3-L-CNL | 5 | 206 | 10.2 | 10.2 | 3.62 | 10.5 |

### *Results for tests under CNS conditions*

Six (6) direct shear tests were performed on large-size fractures (300 mm × 500 mm), as initially described in Table 2-1, under CNS conditions. Within this group, three tests were performed on natural fractures (N1-L-CNS, N2-L-CNS, and N3-L-CNS), and three on tensile-induced fractures (TI1-L-CNS, TI2-L-CNS, and TI3-L-CNS). Shear stress is plotted versus shear displacement for these six tests in Figure 6-7. In the case of tests with natural fractures, the shear stress at fully developed shear slip was between 6.6 and 7.9 MPa, and for the tests with tensile-induced fractures, it was in the range of 13.4 to 16.5 MPa.
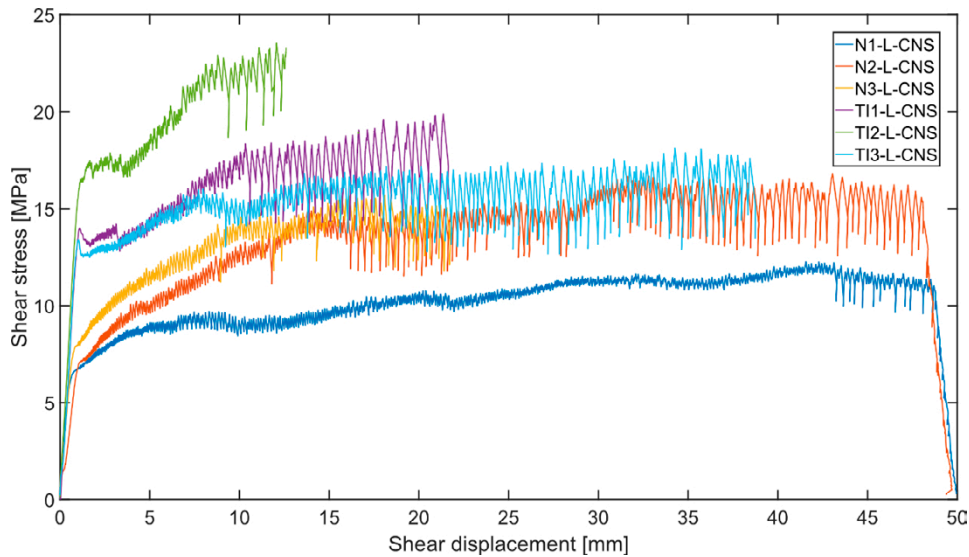
**Figure 6-7.** *Shear stress results plotted versus shear displacement, for the natural (N) and tensile-induced (TI) large-size fractures tested under CNS conditions (displacement results from non-local LVDT measurements). Note that some tests were stopped before reaching the target shear displacement (50 mm) because the limit normal stress of about 33 MPa was reached.*

Regarding dilation behaviour observed for natural fractures (Figure 6-8, specimens N1-L-CNS, N2-L-CNS, and N3-L-CNS), this was similar for the three specimens during the first 2–5 mm shear displacement, but the dilation rate decreased due to an increased normal stress to keep a constant stiffness and was almost zero from 20–25 mm shear displacement and onwards, reaching values in the range of 1 to 2 mm for specimens N1-L-CNS and N2-L-CNS.

The presented dilation value by the LVDTs is underestimated, when compared with that based on local DIC measurements by approximately 0.20–0.25 mm at a normal stress of 20 MPa and 0.30–0.35 mm at a normal stress of 30 MPa during the CNS experiments. The dilation yielded an increase of the normal stress from 5 MPa up to approximately 18.5, 27 and 30 MPa for the three natural fractures. The increased normal stress yielded an increase of the shear stress up to 12–17 MPa.

For tests on tensile-induced fractures, the dilation was up to 2.4 mm (with a correction for system deformations according to Section 5.1.3, up to 2.70–2.75 mm) as presented in Figure 6-8. This yielded an increase of the normal stress up to 33 MPa (normal force up to 4.7 MN) and still increasing. It was therefore decided to abort the tests before the final value of 50 mm shear displacement was reached in order not to overload the shear box device. The shear stress was between 17–23 MPa for the three specimens when the shearing was aborted (Figure 6-7).

Table 6-5 provides a summary of the results from direct shear tests on large-size natural and tensile-induced fractures under CNS conditions.

**Table 6-5. Summary of results from direct shear tests on large-size natural and tensile-induced fractures under CNS conditions.**

| Specimen ID | $\sigma_{N0}$ [MPa] | $K_S$ [MPa/ mm] | $\sigma_{S,s}$ [MPa] | $\sigma_{S,p}$ [MPa] | $\sigma_{S,r}$ [MPa] | $\Psi$ [deg] |
|---|---|---|---|---|---|---|
| N1-L-CNS | 5 | 43.1 | 6.63 | - | - | 5.91 |
| N2-L-CNS | 5 | 35.2 | 7.17 | - | - | 8.29 |
| N3-L-CNS | 5 | 88.9 | 7.93 | - | - | 9.15 |
| TI1-L-CNS | 5 | 174 | 14.0 | - | - | 9.47 |
| TI2-L-CNS | 5 | 109 | 16.5 | - | - | 11.6 |
| TI3-L-CNS | 5 | 179 | 13.4 | - | - | 9.34 |
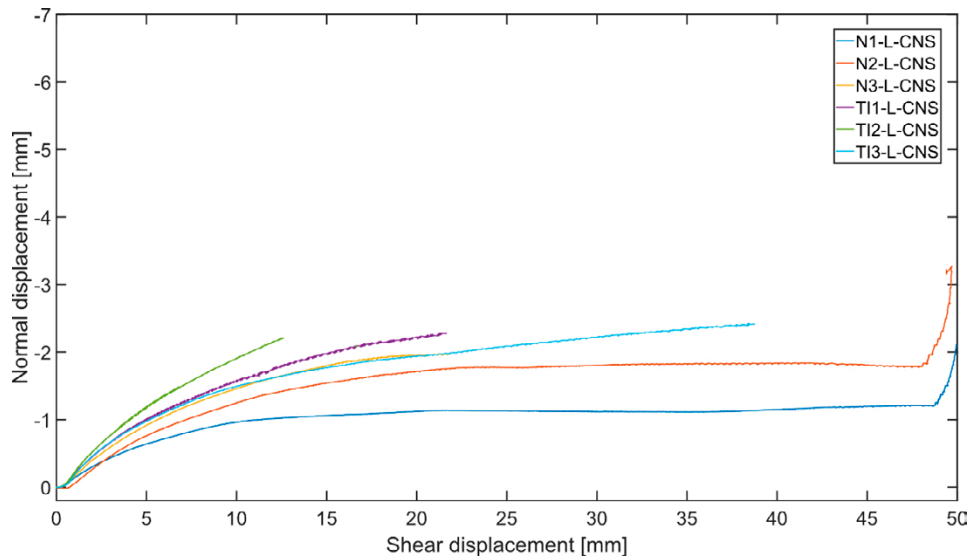
**Figure 6-8.** *Normal displacement plotted versus shear displacement, for the natural (N) and tensile-induced (TI) large-size fractures tested under CNS conditions (displacement results retrieved from non-local LVDT measurements).*

### 6.2.2 Medium-size rock specimens

Regarding the medium-size rock specimens (70 mm × 100 mm), nine tests were conducted under CNL conditions: six on natural fractures under different normal stress ($\sigma_{N0}$ = 1 MPa for N3-M-CNL, $\sigma_{N0}$ = 2 MPa for N2-M-CNL, $\sigma_{N0}$ = 5 MPa for N1-, N6- and N7-M-CNL, and $\sigma_{N0}$ = 10 MPa for N4-M-CNL), and three on tensile induced fractures. It should be noted that local (DIC-based) measurements were not conducted for the natural medium sized fractures, neither under CNL nor under CNS. Results for these fractures with LVDT-based displacement measurements can instead be consulted in detail in Jacobsson et al. (2024b). The results in Jacobsson et al. (2024b) showed that the shear stress of the initial shearing was lower for CNL specimens with $\sigma_{N0}$ = 5 MPa, showing values in the range of 4.2–4.9 MPa. An exception was observed for specimen N7-M-CNL that had a larger peak shear stress at10.2 MPa. For the CNS specimens, the initial peak shear stress was approximately 5.8–6.7 MPa. The CNS specimens displayed a dilatancy-induced increase of the normal stress, which increased to a final value between approximately 10.5–14 MPa with residual shear stress of 7.2–9.0 MPa. The CNL specimens had a residual shear strength on the range of 2.8–3.7 MPa.

For medium-size tensile-induced rock fractures under CNL conditions, the shear stress is plotted against the shear displacement in Figure 6-9. Note the absence of results for TI1-M-CNL specimen since this test was carried out before DIC-based measurements were introduced in the project. The CNL specimens had all peak shear stresses, which were in the range of 11.5–13.5 MPa. The residual shear strength values for the tensile-induced CNL specimens were in the range of 4.7–5.4 MPa. In terms of dilation (Figure 6-10), both specimens (TI2-M-CNL and TI3-M-CNL) followed a similar, constantly increasing trend. Measurements for specimen TI3-M-CNL became distorted at 2.5 mm of shearing. Specimen TI2-M-CNL reached a maximum normal displacement value of about 2 mm at 7 mm of shearing. In terms of shear stiffness, all tested specimens had a peak shear stress almost instantly after the shear test started. The shear stiffness was high for the three specimens instrumented with local (DIC-based) fracture deformation measurements (843–1 170 MPa/mm).

Regarding the tests under CNS conditions, the shear stress during the initial shearing for these specimens was approximately 12–15 MPa. These specimens displayed a dilatancy-induced increase of the normal stress, which reached a final value in between 13–17.5 MPa. The residual shear stresses for the CNS specimens were in the range 8.8–12.7 MPa. Figure 6-11 shows shear stress against shear displacement for specimen TI4-M-CNS, showing also a peak shear strength value of about 13 MPa before the shear displacement starts. After the shear stress drops until 10 MPa approximately, the residual shear stress for this specimen is kept between 10–14 MPa. The measurements are distorted after a shear displacement of about 5 mm. The corresponding normal displacement plotted against the shear displacement is presented in Figure 6-12 for the same TI4-M-CNS specimen.
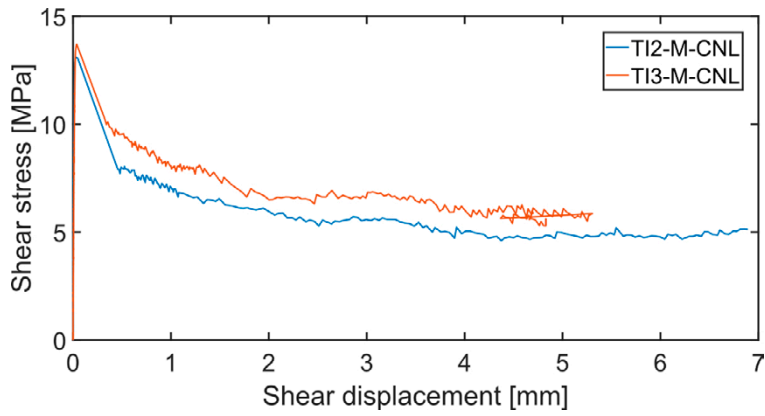
**Figure 6-9.** *Shear stress and normal displacement results plotted versus shear displacement, for tensile-induced (TI) medium-size fractures tested under CNL conditions (displacement results from local DIC measurements).*
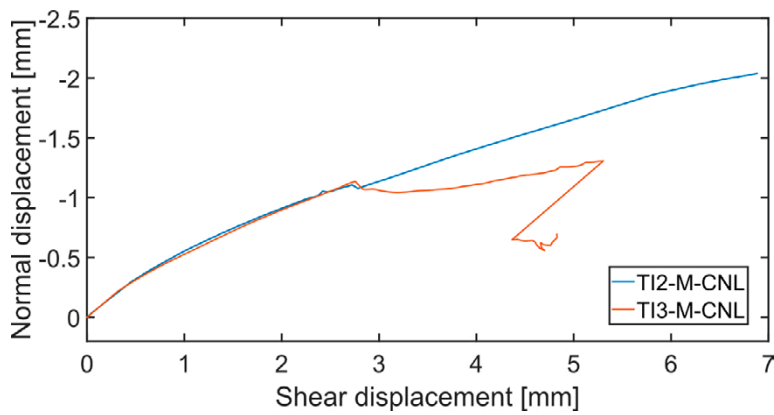


**Figure 6-10.** *Normal displacement results plotted versus shear displacement, for TI2-M-CNL and TI3-M-CNL fractures tested under CNL conditions (displacement results from local DIC measurements).*
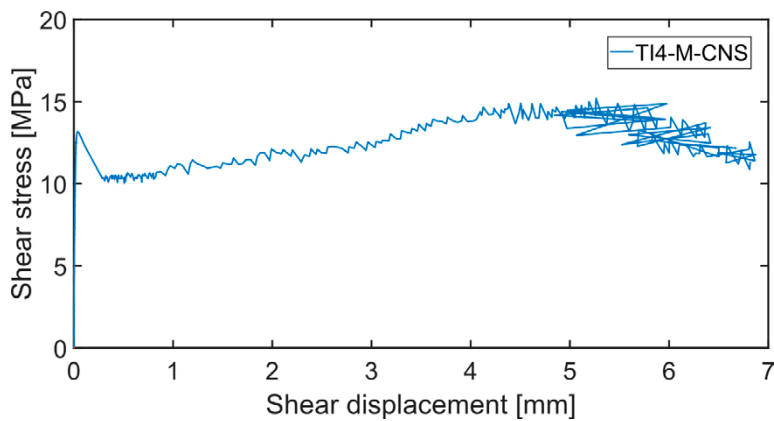


**Figure 6-11.** *Shear stress results plotted versus shear displacement, for TI4-M-CNS fracture tested under CNS conditions (displacement results from local DIC measurements).*
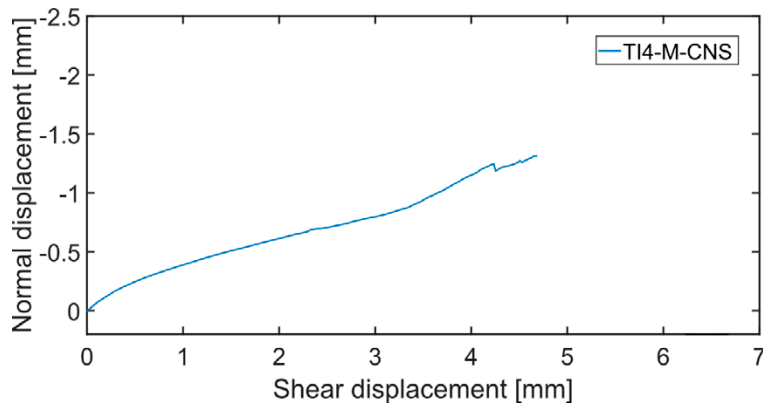
***Figure 6-12.*** *Normal displacement results plotted versus shear displacement for TI4-M-CNS fracture tested under CNS conditions (displacement results from local DIC measurements).*

A summary of results for both types of medium-size fractures under CNL and CNS conditions are presented in Table 6-6 and Table 6-7, together with residual dilation angle and some shear stiffness values for specimens TI2-, TI3-M-CNL, and for TI4-M-CNS.

**Table 6-6. Summary of results from direct shear tests on medium-size natural and tensile-induced fractures under CNL conditions.**

| Specimen ID | $\sigma_{N0}$ [MPa] | $K_s$ [MPa/mm] | $\sigma_{s,s}$ [MPa] | $\sigma_{s,p}$ [MPa] | $\sigma_{s,r}$ [MPa] | $\Psi_d$ [deg] |
|---|---|---|---|---|---|---|
| N1-M-CNL | 5 | - | 4.9 | 4.9 | 3.3 | 9.2 |
| N2-M-CNL | 2 | - | 2.5 | 2.5 | 1.5 | 13.2 |
| N3-M-CNL | 1 | - | 1.5 | 1.5 | 0.7 | 10.9 |
| N4-M-CNL | 10 | - | 10.0 | 10.0 | 6.9 | 6.4 |
| N6-M-CNL | 5 | - | 4.2 | 4.2 | 2.8 | 8.1 |
| N7-M-CNL | 5 | - | 10.2 | 10.2 | 3.7 | 9.1 |
| TI1-M-CNL | 5 | - | 11.6 | 11.6 | 4.7 | 16.5 |
| TI2-M-CNL | 5 | 1 160 | 13.0 | 13.0 | 4.8 | 14.6 |
| TI3-M-CNL | 5 | 875 | 13.7 | 13.7 | 5.4 | 16.1 |

**Table 6-7. Summary of results from direct shear tests on medium-size natural and tensile-induced fractures under CNS conditions.**

| Specimen ID | $\sigma_{N0}$ [MPa] | $K_s$ [MPa/mm] | $\sigma_{s,s}$ [MPa] | $\sigma_{s,p}$ [MPa] | $\sigma_{s,r}$ [MPa] | $\Psi_d$ [deg] |
|---|---|---|---|---|---|---|
| N5-M-CNS | 5 | - | 6.7 | 9.8 | 9.0 | 5.9 |
| N8-M-CNS | 5 | - | 6.8 | 9.2 | 8.0 | 5.7 |
| N9-M-CNS | 5 | - | 5.8 | 7.8 | 7.2 | 5.3 |
| TI4-M-CNS | 5 | 719 | 13.1 | 15.2 | 12.7 | 9.2 |
| TI5-M-CNS | 5 | - | 12.1 | 12.4 | 11.4 | 8.6 |
| TI6-M-CNS | 5 | - | 15.1 | 15.1 | 8.8 | 6.2 |

### 6.2.3 Small-size rock specimens

For small-size rock specimens (35 mm × 60 mm), the results of the direct shear tests on the natural fractures showed that the shear stress at the initial shearing was lower for the tests under CNL conditions (approximately 4.0–6.5 MPa, as presented in Figure 6-13) than for the specimens tested under CNS conditions (approximately 6.9–13.5 MPa, as shown by Figure 6-15). The CNL specimens had a residual shear strength on the range of 3.6–5.3 MPa. In a similar way as for the medium-size fractures, the CNS specimens displayed a dilatancy-induced increase of the normal stress, which increased to a final value to approximately in between 11–14 MPa with residual shear strength of 8.1–11.2 MPa.
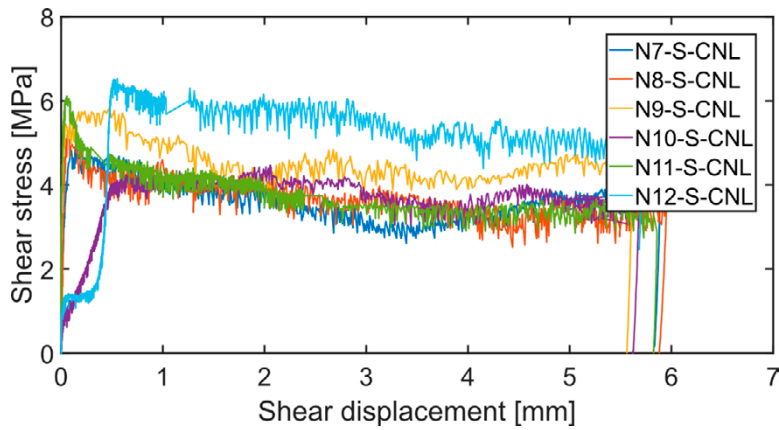
***Figure 6-13.*** *Shear stress results plotted versus shear displacement, for small-size natural fractures tested under CNL conditions (displacement results from local DIC measurements).*
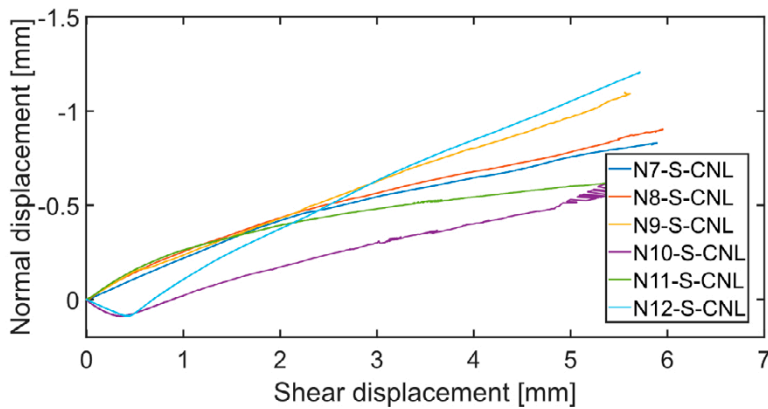


***Figure 6-14.*** *Normal displacement results plotted versus shear displacement, for small-size natural fractures tested under CNL conditions (displacement results from local DIC measurements).*
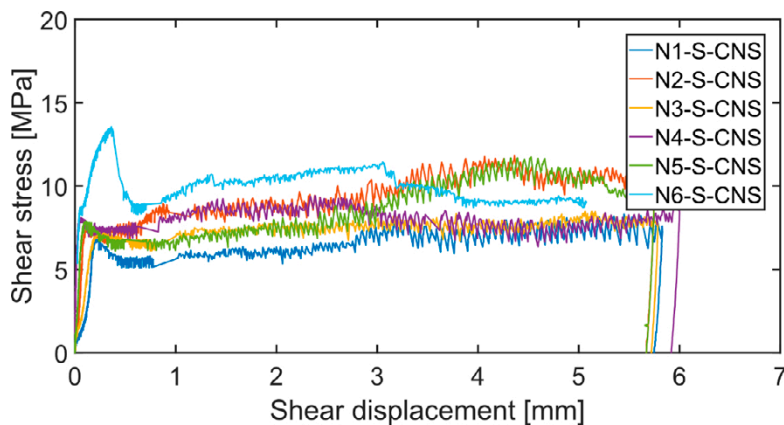


***Figure 6-15.*** *Shear stress results plotted versus shear displacement, for small-size natural fractures tested under CNS conditions (displacement results from local DIC measurements).*

***Figure 6-16.** Normal displacement results plotted versus shear displacement, for small-size natural fractures tested under CNS conditions (displacement results from local DIC measurements).*

The small-size tensile-induced rock fractures were all tested under a normal stress of 5 MPa for the CNL tests and under an initial normal stress of 5 MPa. The CNL specimens (Figure 6-17) had all peak shear strength values that were in the range of 8.5–13 MPa. The residual shear strength values for the CNL specimens displayed in the range of 3.5–5 MPa. For specimens tested under CNS conditions (Figure 6-19), the stress at the initial shearing was approximately 12–15 MPa with two outliers: TI1-S-CNS (approximately 8 MPa) which showed no peak in conjunction with onset of shearing and TI5-S-CNS which has a large peak at 19 MPa, followed by a large stress drop. The other four CNS specimens, mentioned initially, had distinct peak shear strengths. The CNS specimens displayed a dilation-induced increase of the normal stress (Figure 6-20), which increased to a final value to approximately in between 12.5–15. MPa. The residual shear strength values for the CNS specimens varied a lot, TI1 and TI2 (about 7.5 MPa), TI3 and TI4 (about 9–10 MPa) and TI5 and TI6 (about 13 MPa).

A summary of results from direct shear tests is presented in Table 6-8, for both types of fractures in small-size specimens tested under CNL conditions, and in Table 6-9, for both types of fractures in small-size specimens, tested under CNS conditions.
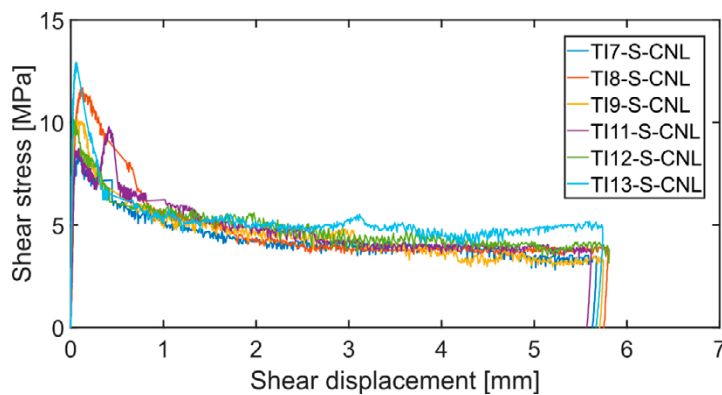


***Figure 6-17.** Shear stress results plotted versus shear displacement, for small-size tensile-induced fractures tested under CNL conditions (displacement results from local DIC measurements).*

**Figure 6-18.** *Normal displacement results plotted versus shear displacement, for small-size tensile-induced fractures tested under CNL conditions (displacement results from local DIC measurements).*
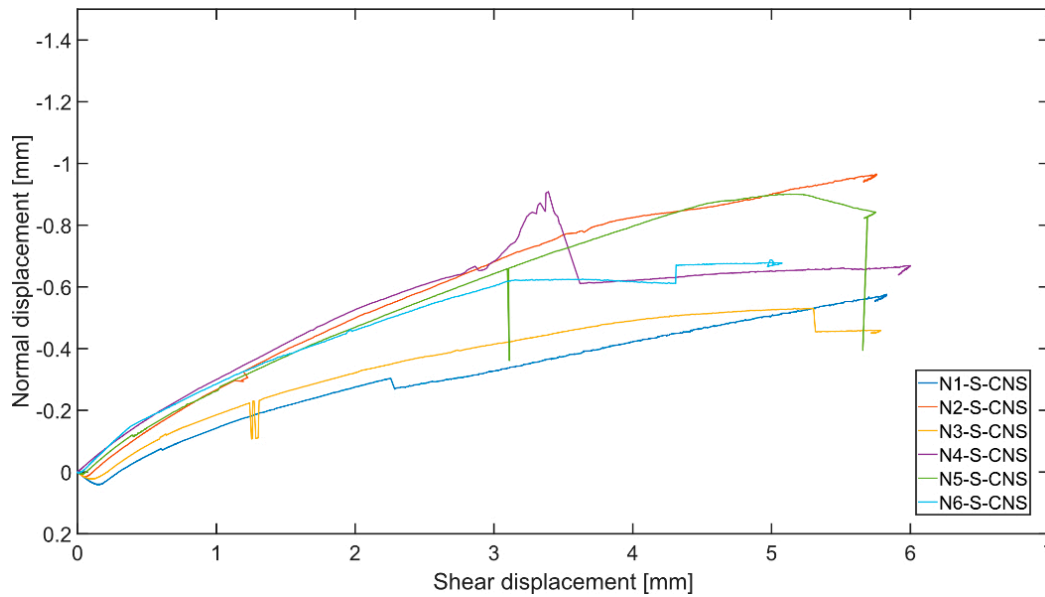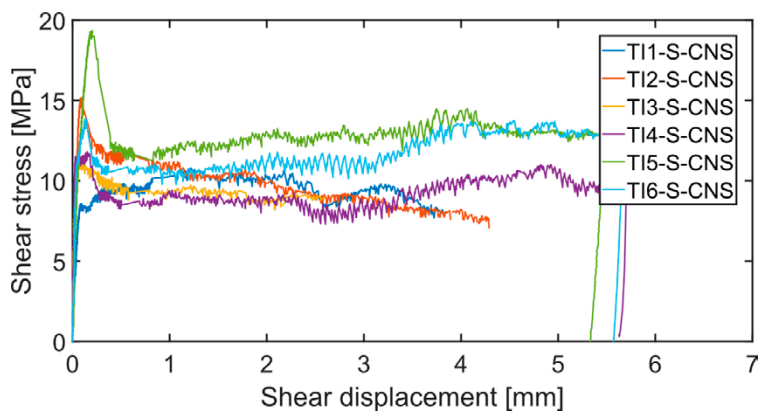


**Figure 6-19.** *Shear stress results plotted versus shear displacement, for small-size tensile-induced fractures tested under CNS conditions (displacement results from local DIC measurements).*
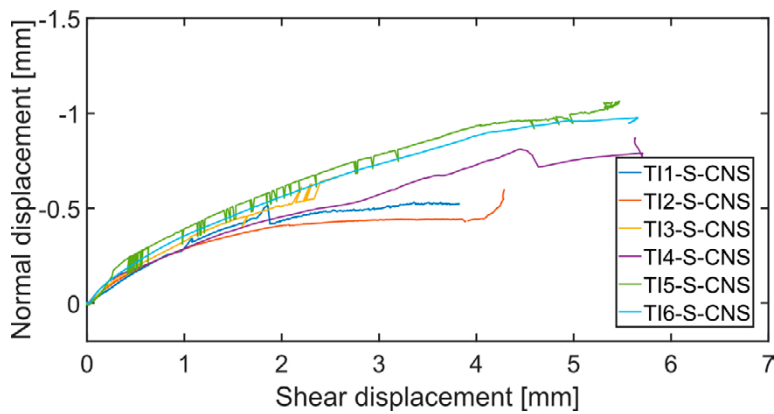


**Figure 6-20.** *Normal displacement results plotted versus shear displacement, for small-size tensile-induced fractures tested under CNS conditions (displacement results from local DIC measurements).*
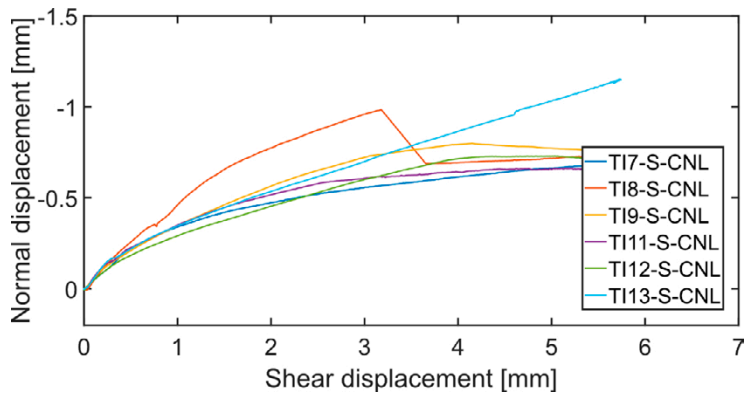
**Table 6-8. Summary of results from direct shear tests on small-size natural and tensile-induced fractures under CNL conditions.**

| Specimen ID | $\sigma_{N0}$ [MPa] | $K_s$ [MPa/mm] | $\sigma_{s,s}$ [MPa] | $\sigma_{s,p}$ [MPa] | $\sigma_{s,r}$ [MPa] | $\Psi_d$ [deg] |
|---|---|---|---|---|---|---|
| N7-S-CNL | 5 | 60.2 | 4.9 | 4.9 | 4.0 | 8.1 |
| N8-S-CNL | 5 | 121 | 5.2 | 5.2 | 3.6 | 8.3 |
| N9-S-CNL | 5 | 176 | 5.5 | 5.9 | 4.7 | 8.7 |
| N10-S-CNL | 5 | 7.27 | 4.0 | 4.5 | 3.7 | 7.1 |
| N11-S-CNL | 5 | 239 | 6.2 | 6.2 | 3.7 | 5.5 |
| N12-S-CNL | 5 | 7.98 | 6.5 | 6.5 | 5.3 | 14.7 |
| TI7-S-CNL | 5 | 253 | 8.5 | 8.5 | 3.7 | 5.8 |
| TI8-S-CNL | 5 | 180 | 11.6 | 11.6 | 3.9 | 5.4 |
| TI9-S-CNL | 5 | 364 | 10.1 | 10.1 | 3.5 | 9.2 |
| TI11-S-CNL | 5 | 252 | 8.7 | 9.8 | 4.0 | 6.7 |
| TI12-S-CNL | 5 | 461 | 10.1 | 10.1 | 4.2 | 9.2 |
| TI13-S-CNL | 5 | 702 | 12.8 | 12.8 | 4.9 | 9.7 |

**Table 6-9. Summary of results from direct shear tests on small-size natural and tensile-induced fractures under CNS conditions.**

| Specimen ID | $\sigma_{N0}$ [MPa] | $K_s$ [MPa/mm] | $\sigma_{s,s}$ [MPa] | $\sigma_{s,p}$ [MPa] | $\sigma_{s,r}$ [MPa] | $\Psi_d$ [deg] |
|---|---|---|---|---|---|---|
| N1-S-CNS | 5 | 24.5 | 6.9 | 8.4 | 8.1 | 6.3 |
| N2-S-CNS | 5 | 66.8 | 7.5 | 11.8 | 11.2 | 9.3 |
| N3-S-CNS | 5 | 34.0 | 7.4 | 8.5 | 8.4 | 5.8 |
| N4-S-CNS | 5 | 356 | 8.1 | 9.5 | 8.4 | 7.8 |
| N5-S-CNS | 5 | 101 | 7.9 | 11.9 | 10.8 | 9.4 |
| N6-S-CNS | 5 | 243 | 13.5 | 13.5 | 9.0 | 6.3 |
| TI1-S-CNS | 5 | 131 | 8.5 | 10.7 | 7.5 | 5.6 |
| TI2-S-CNS | 5 | 421 | 15.2 | 15.2 | 7.6 | 3.9 |
| TI3-S-CNS | 5 | 589 | 11.3 | 11.3 | 9.7 | 5.4 |
| TI4-S-CNS | 5 | 572 | 11.5 | 11.8 | 10.6 | 6.4 |
| TI5-S-CNS | 5 | 224 | 19.1 | 19.2 | 13.2 | 10.0 |
| TI6-S-CNS | 5 | 312 | 13.8 | 13.8 | 13.4 | 9.5 |

### 6.2.4 Replicas

Several direct shear tests were performed on different concrete fracture replicas (naturally mated and fully mated, according to the procedure shown in Section 3.6.2) from a natural fracture designated N1-CNL. The tests were performed under CNL conditions, for both types of replicas (6 tests on the naturally mated and 3 on the perfectly mated ones), and under CNS conditions only for 6 perfectly mated ones. The results from this experimental program are summarised in Figure 6-21, Figure 6-22 and Table 6-10.

Shear stress is plotted against shear displacement in Figure 6-21a, for direct shear tests on N1-CNL rock fracture and on perfectly (RPM) and naturally (RNM) mated replicas. A detailed view of these results is presented in Figure 6-21b for a 2 mm shear displacement. Overall, the characteristics of RNM-N1-CNL-(1–3) do not resemble neither those of the rock specimen (N1-CNL) nor those of RNM-N1-CNL-(4–6), as a clear peak stress is lacking, and residual stresses are higher, especially after 2 mm shearing displacement on the residual stage (Figure 6-21a). Replicas RNM-N1-CNL-5 and RNM-N1-CNL-6 show quite similar results at peak, reaching values of 3.6 and 4 MPa at a 0.5 mm shear displacement, followed by a residual state at about 3–3.5 MPa. This aligns with the results observed for the geometrical quality assurance parameter $\sigma_{mf}$ (Equation 4-1), as presented in Section 4.5.3.
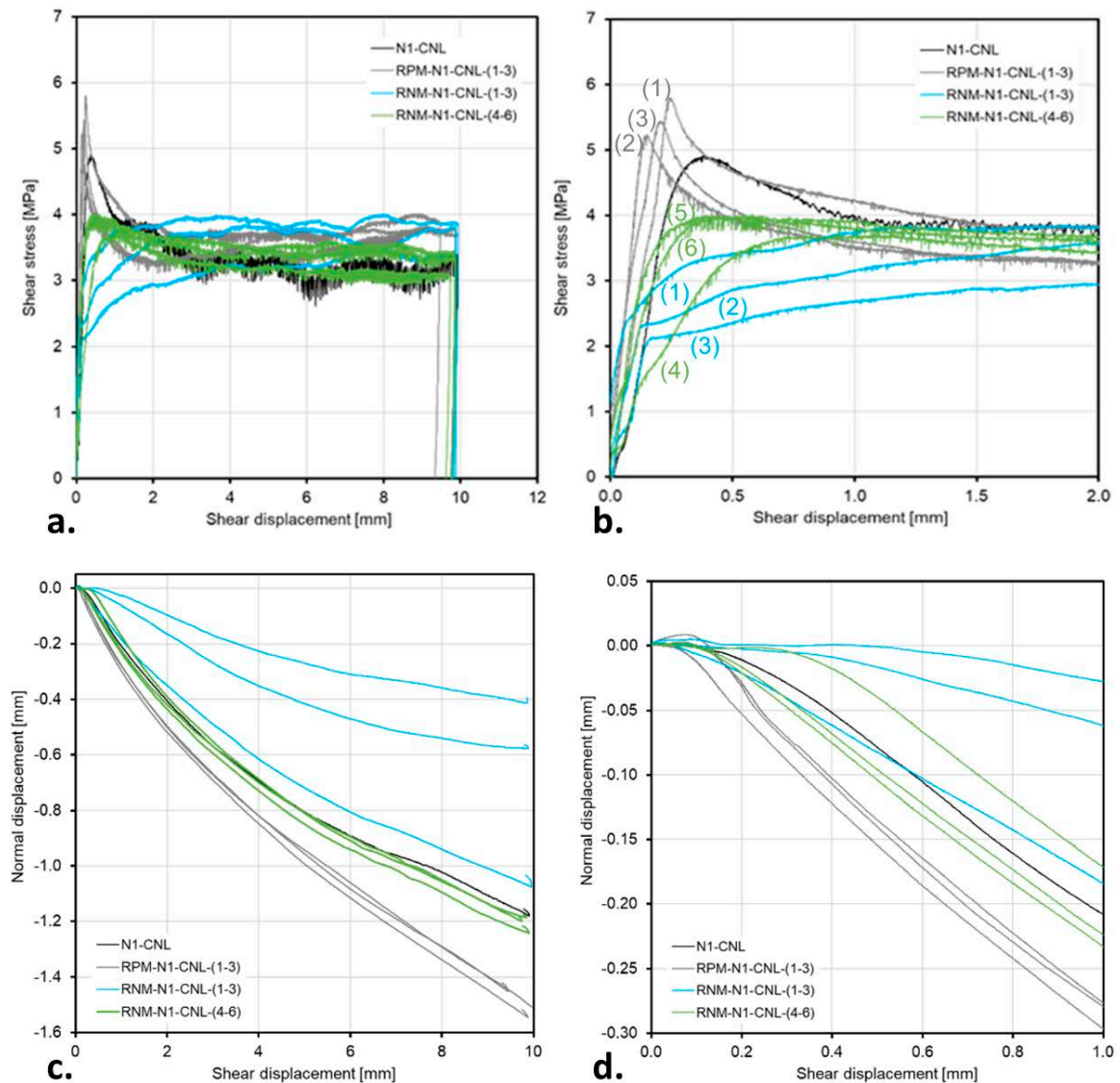
***Figure 6-21.*** *a. Shear stress versus shear displacement curves from direct shear tests on rock fracture N1-CNL, perfectly-mated replicas RPM-N1-CNL-(1-3), and naturally mated replicas RNM-N1-CNL-(1-3) and (4-6); b. Detailed view of results in a. for a maximum shear displacement of 2 mm; c. Normal displacement versus shear displacement curves for the same specimens in a., and d. Detailed view of results in c. for a maximum shear displacement of 1 mm.*

All specimens continuously dilated during the residual stage, as shown in Figure 6-21c and d, with maximum values of about 1.2 mm at 10 mm of shear displacement for specimens RNM-N1-CNL-1, and RNM-N1-CNL-(4–6), close to those shown by the rock specimen, but with lower values (0.4 to 0.6 mm) for specimens RNM-N1-CNL-2 and RNM-N1-CNL-3. For perfectly matched replica fractures, dilation about 1.5–1.6 mm can be observed for 10 mm shear displacement.

The influence of the positioning plugs (sprues) in the moulds is clearly seen through the absence of clear peak stresses in RNM-N1-CNL-1–3. It is not obvious that RNM-N1-CNL-2 shall be ranked higher than RNM-N1-CNL-3 in terms of extent of match. A possible explanation to the higher shear stress levels in RNM-N1-CNL-2, despite the large depression in the lower part, could be that the elevation in the upper part contributes to improve the match compared to RNM-N1-CNL-3. Overall, the characteristics of RNM-N1-CNL-1–3 do not resemble those of the rock specimen and RNM-N1-CNL-4–6, as a clear peak stress is lacking, and the residual shear strengths are higher. The reasoning behind these observations needs to be further investigated but is thought to be related to a lower degree of matedness. The characteristics of RNM-N1-CNL-4–6 do however have a better correlation to those of N1-CNL, such that a peak stress is apparent, and the residual stresses are within a similar range.

It is such that these specimens have peak shear strengths between 3.6 and 4 MPa at a displacement ranging between 0.5 to 1 mm, which is followed by a lower residual stress of about 3 MPa for larger displacements. Moreover, the internal ranking between RNM-N1-CNL-4–6 correlates to the presence of elevations in the upper part (Figure 4-26 and Figure 4-27), which in turn affects the match. Table 6-10 shows a summary of results from all direct shear tests on replica specimens.

Figure 6-22 shows results on perfectly-mated replicas under CNS conditions where, unlike most of the results for CNL conditions, pronounced peak shear values can be observed between 0.2 to 0.4 mm of shear displacement, distributed in the range of 5 to almost 10 MPa. Regarding post-peak behaviour, dilation-induced shear stress values that increase with shear displacement are particularly observed for RPM-N1-CNS-(2–6), reaching approximately 17.5 MPa for, i.e., RPM-N1-CNS-4.

**Table 6-10. Summary of results from direct shear tests on replica specimens.**

| Specimen ID | $\sigma_{N0}$ (MPa) | $k_N$ [MPa/mm] | $\sigma_{S,s}$ [MPa] | $\sigma_{S,p}$ (MPa) | $\sigma_{S,r}$ (MPa) | $\Psi$ (deg) |
|---|---|---|---|---|---|---|
| RNM-N1-CNL-1 | 5 | 0 | 3.6 | 4.0 | 3.9 | 8.2 |
| RNM-N1-CNL-2 | 5 | 0 | 3.0 | 3.9 | 3.7 | 5.5 |
| RNM-N1-CNL-3 | 5 | 0 | 2.6 | 3.5 | 3.4 | 3.8 |
| RNM-N1-CNL-4 | 5 | 0 | 3.7 | 3.7 | 3.1 | 9.8 |
| RNM-N1-CNL-5 | 5 | 0 | 4.0 | 4.0 | 3.5 | 9.0 |
| RNM-N1-CNL-6 | 5 | 0 | 4.0 | 4.0 | 3.4 | 9.4 |
| RPM-N1-CNL-1 | 5 | 0 | 5.8 | 5.8 | 3.9 | 10.2 |
| RPM-N1-CNL-2 | 5 | 0 | 5.2 | 5.2 | 3.8 | 10.4 |
| RPM-N1-CNL-3 | 5 | 0 | 5.4 | 5.4 | 3.8 | 10.2 |
| RPM-N1-CNS-1 | 5 | 2 | 5.5 | 5.7 | 5.5 | 9.5 |
| RPM-N1-CNS-2 | 5 | 5 | 7.3 | 8.8 | 8.5 | 8.1 |
| RPM-N1-CNS-3 | 5 | 10 | 7.4 | 14.7 | 14.3 | - |
| RPM-N1-CNS-4 | 5 | 15 | 9.4 | 17.7 | 17.5 | 6.2 |
| RPM-N1-CNS-5 | 5 | 10 | 9.9 | 14.5 | 13.8 | 7.1 |
| RPM-N1-CNS-6 | 5 | 10 | 8.9 | 15.4 | 14.7 | 7.4 |
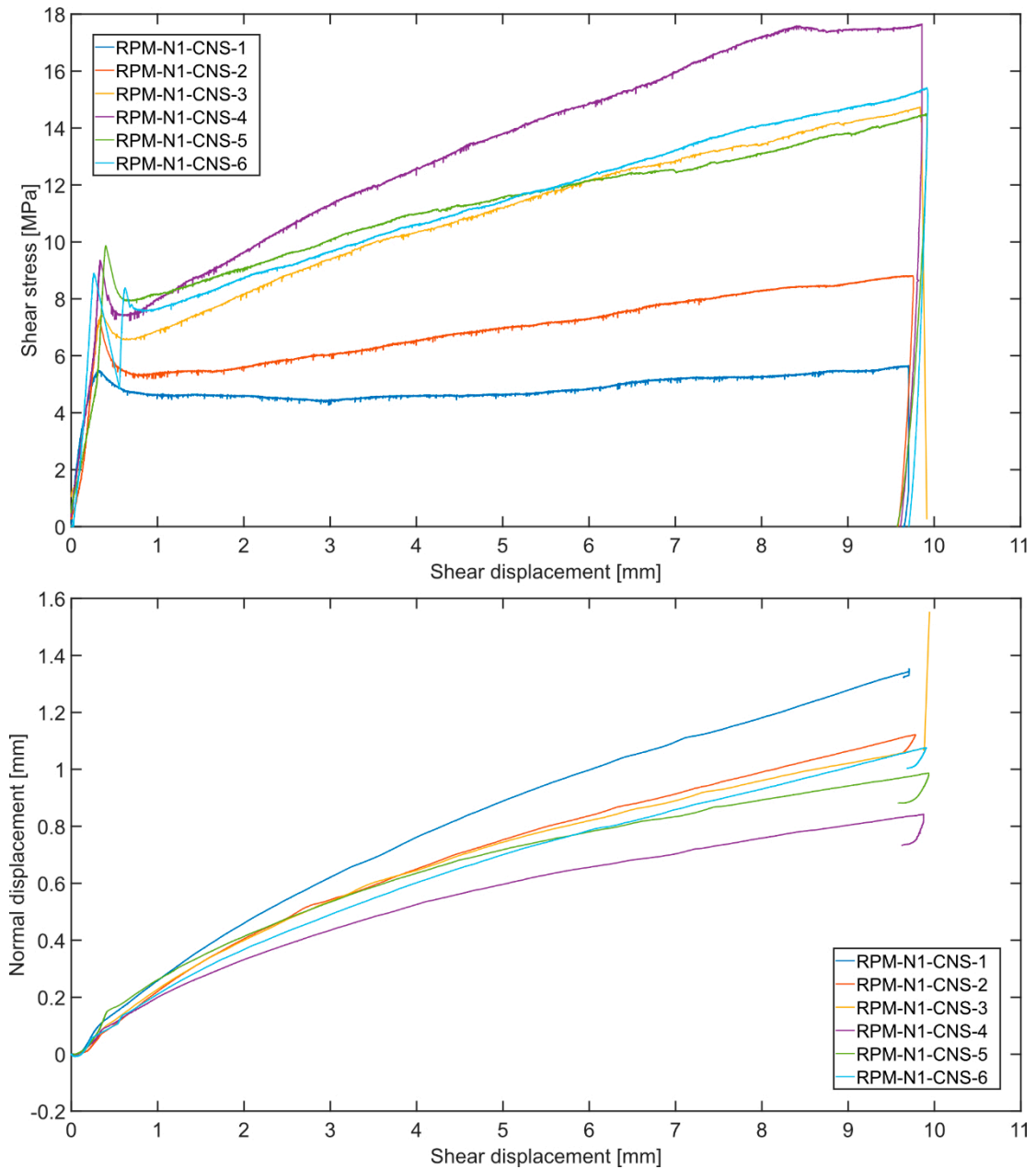
***Figure 6-22.*** *Shear stress and normal displacement versus shear displacement, from direct shear tests on perfectly mated replicas RPM-N1-CNS-1 to RPM-N1-CNS-6 under CNS conditions and different $K_n$ values ($K_n$ = 15 MPa/mm for RPM-N1-CNS-4; $K_n$ = 10 MPa/mm for RPM-N1-CNS-3, -5 and-6; $K_n$ = 5 MPa/mm for RPM-N1-CNS-2, and $K_n$ = 2 MPa/mm for RPM-N1-CNS-1 ).*

# 7 Discussion

A comprehensive experimental program on direct shear tests on two types of rock fractures (natural and tensile induced) at three different scales under CNL and CNS conditions has been performed for this project. In this context, a new large-scale direct shear test equipment was specifically designed and manufactured for tests on the large-size fractures (300 mm × 500 mm). A procedure for acquiring undisturbed fractured rock specimens of three sizes from a single fracture set and tensile induced fractures from intact rock blocks as well as manufacturing replicas of hard rock fractures were developed including a method for quality assurance of replicas. Normal loading and direct shear tests were performed both on rock and concrete replica fractures, with conventional non-local (LVDT-based) and novel local (DIC-based) fracture displacement measurements. While the overall aims of this project can be considered successfully achieved, it becomes necessary to open a discussion on certain aspects like the implications of using a particular local (DIC-based) displacement measuring technique, or the impact of boundary conditions on strength and deformability, as well as the effect of scale on the results. The use of fracture replicas as representative samples is also discussed together with some general aspects at the end of this section.

## 7.1 Acquiring prototype fractured rock specimens

The location of the planned repository in Forsmark (Sweden) is at approximately 400–500 m depth. It is challenging to access representative naturally fractured rock material from these locations. In Siren et al. (2017), two main options were discussed, (1) to cut blocks out of a tunnel wall, e.g. close to a tunnel intersection by wire sawing, and (2) extracting large cores from the wall with a fracture plane along the core diameter as it was done at a smaller scale in the first project phase (Jacobsson 2016).

In this project phase, a rock material similar to other granitic rock-types from the Forsmark area was obtained from a quarry in Flivik (Sweden). This rock material has slightly weathered natural fractures with small amount of infill material and presents a geological history representative of the target location. Blocks with a size of about 2 m side length having a visible natural planar fracture on the lateral sides of the blocks were selected. In the end, two blocks had a fracture that terminated, leaving a large rock bridge to secure the fracture. They were carefully processed in stages down to a final specimen size keeping undisturbed fractures. Some intermediate-size blocks were split by a sledgehammer and wedges. It should be mentioned that the best block found in the quarry had a planar fracture going through the whole block and the fracture was visible all around the block. However, the fracture opened during subsequent handing in the quarry. A lesson learned is that some reinforcement can help to keep the fracture intact in case of handling fully fractured blocks with through-going fractures.

The alternative option to extract large diameter cores (300 to 400 mm diameter) from a tunnel wall and to process these cores is still to be investigated.

## 7.2 Implications of local fracture displacement measurements

Local fracture deformation measurements using crack opening displacement gauges were previously used at RISE rock mechanics laboratory in conjunction with normal loading tests to measure the displacements directly on the specimen sides across the fracture and was found necessary for accurate determination of the fracture normal stiffness (e.g. Jacobsson et al. 2012, Jacobsson 2016). Conventional indirect-measuring devices typically read the relative displacement between the shear boxes, which means also undesired deformations of all components between the fracture and the transducers besides the desired fracture displacements. Moreover, as pointed out by (Jacobsson and Flansbjer 2005), the correction method provided by the current ISRM Suggested Method for Laboratory Determination of the Shear Strength of Rocks (Muralha et al. 2014) is still not completely accurate for determining fracture stiffness.

The design of the new large-scale shear test equipment allowed easy access to the specimen sides, and it was decided to add an optical system based on DIC able to directly measure relative displacement of the fracture. The advantage with this optical system is that no mechanical gauges are used. This means that the same measurement setup can be used for both the normal loading and the direct shear tests and measure both normal and shear displacements across the fracture. The initial measurements were successful, and it was therefore decided to add a similar but adapted system to the small-scale testing equipment. It is only the later part of the tested medium-scale specimens and all small-scale specimens that were conducted with the direct DIC-based measurements.

The plots for normal loading tests illustrate the significant differences when comparing results from LVDT (non-local) and from DIC-based (local) displacement measurements. This has been observed to have a significant impact on determining fracture normal stiffness, leading to quite major differences between the stiffness values obtained by means of the two methods if no correction is made, and particularly, a generalised underestimation of these parameters for the case of LVDT-based measurements (see Figure 6-1, Figure 6-2 and Figure 6-3). Even though other fracture features like surface geometry, asperity deformability or degree of interlocking may affect its deformability behaviour (Zangerl et al. 2008), a relevant influence of the type of measuring method (local or non-local) was confirmed.

The differences in shear displacement values are evident when comparing LVDT and DIC-based measurements at the shear tests. With non-local LVDT-based measurements, the fracture shear stiffness becomes lower (as for the normal stiffness during the normal loading tests), but also, the peak shear stress is systematically displayed at larger shear displacement values than they actually are. Existing shear strength models that include shear displacement at peak shear strength (or onset of fully mobilised shear slip for the CNS case) will likely need to be revised.

Finally, with access to the accurate local fracture displacement measurements, new possibilities open up to in detail analyses of the deformation processes that takes place during the normal loading tests and the early stage of the direct shear tests. These analyses gain an increased understanding of the deformation processes in the fracture, especially with access to additional data such as fracture geometries and contact pressure distributions.

It should be noted that the local measurements by DIC are sensitive to local fracturing at the areas where the measurements are done on the specimen sides. The local measurements by the DIC are therefore more suitable to determine the behaviour during the initial phase of the shearing (the first few millimetres).

## 7.3 The significance of CNS condition

One of the main objectives of the project was to determine the behaviour and the mechanical parameters of rock fractures subjected to 50 mm of shear displacement under conditions representative to repository depth, and to verify the strengthening effect under CNS conditions. That concerns an initial stress level of approximately 5 MPa and CNS conditions with an anticipated rock mass stiffness of 10 MPa/mm. Direct shear tests with 50 mm shear displacement were done on the large specimens (300 × 500 mm) which was in compliance with the ISRM recommendation, Muralha et al (2014), i.e. max shear displacement of 10 % of the specimen length. These tests were performed under both CNL and CNS conditions on natural and tensile induced fractures.

The deformations in system components affects the fracture dilation measurements when the non-local measurement system by LVDTs is used as pointed out in Section 7.2. This affects the normal stress control under CNS tests since the control is based on the non-local fracture displacement measurements. A correction is needed where the contribution of the system deformation at normal stress control is cancelled. This was done during all CNS tests according to the method described in Larsson and Flansbjer (2020). The correction of the applied CNS value implies that a larger value must be used by the test system, in this case 7 %, 19 % and 15 % for the three specimen sizes (small, medium and large), to impose the correct stiffness value during the test.

In the results from the large-size CNL tests studied in Figure 6-5 and Figure 6-7, a clear peak shear strength can be observed at 5.95 MPa for the natural rock fracture and an average value of 10.2 MPa for the tensile induced. This is followed by a rapid decrease in shear strength with shear displacement and a relatively uniform residual shear strength. This type of behaviour was expected and has been observed in several other studies, such as Grasselli and Egger 2003, and Johansson (2016) among others, especially for more mated fractures. For the CNS tests on the other hand, no clear peak shear strength can be observed in Figure 6-7 and Figure 6-8. Instead, the shear strength rapidly increases as the dilation of the fracture starts to mobilize additional normal stress. For the natural fractures, a shear strength of 12–17 MPa was observed, while a shear strength of 17–23 MPa was observed for the tensile induced. These results are typical for shear tests performed under CNS conditions, (i.e., Indraratna et al. 2015, Jiang et al. 2004), and clearly show the significance of the CNS conditions on the shear strength for rock fractures. However, for the small and medium sized CNS test, this clear increase in shear strength with shear displacement could not be observed. A possible reason for this discrepancy could be that smaller scales of asperities were mobilized in the small- and medium-sized samples compared to the large-size samples, resulting in a lower dilation, increase in normal stress and therefore a lower shear strength for these sample sizes.

The main parameter governing the shear strength under CNS conditions is the dilation of the fracture during shear. In hard crystalline rock such as granite, even at high normal stresses of 5 MPa, dilatation clearly influences the mechanical behaviour. According to the results of the large sample sizes in Figure 6-5 and Figure 6-7, the natural fractures do not exhibit any peak at the onset of shearing (shear displacements less than 1 mm). This is followed by an almost linear increase in the shear stress with shear displacement. For the tensile induced fractures, the behaviour is different. A small peak in the shear stress can be observed at 0.3–0.4 mm of shear displacement, followed by a strain softening behaviour to approximately 1 mm of shear displacement. After that, the shear stress is almost constant, with no clear increase in dilation. Similar behaviour for the medium and small size samples can be observed as shown in Figure 6-9, Figure 6-11, Figure 6-13, Figure 6-15, Figure 6-17 and Figure 6-19. However, it should be noted that the tests performed in this study were performed in unfilled, single fractures. Presence of infill material, or lenses of intact rock, will lead to decreased dilation or no dilation at all depending in the infill material type and thickness (Jacobsson 2016, Indraratna et al. 1999). Under such conditions, a more ductile behaviour without any significant increase in shear strength with shear displacement can be observed.

Another interesting observation can also be made if the results from the large-size CNL tests in Figure 6-5 and Figure 6-7 are compared against the CNS tests in Figure 6-7 and Figure 6-8. It can also be observed that the shear strength at the onset of shearing, $\sigma_{ss}$, under CNS conditions are slightly higher for both natural and tensile induced fractures. The shear strength of the sample N1-L-CNL was 5.95 MPa, while the average value for the three samples N1-L-CNS, N2-L-CNS and N3-L-CNS was 7.24 MPa. For the tensile induced fractures under CNL conditions, the average value of the results for the samples TI1-L-CNL, TI2-L-CNL, and TI3-L-CNL was 10.2 MPa, while the average value for the tensile induced samples TI1-L-CNS, TI2-L-CNS, and TI3-L-CNS was 14.6 MPa. Similar tendencies can also be observed for the medium and small-size samples in Figure 6-9, Figure 6-11, Figure 6-13 and Figure 6-20. The reason the CNS tests had a higher shear strength at the onset of shearing depends on the fact that the shear displacement at the onset of shearing was 0.3–0.4 mm for the CNS tests. At this shear displacement, a noticeable normal displacement of approximately 0.2 mm was observed in these tests, which corresponds to an additional normal stress of 2 MPa at the onset of shearing, resulting in the observed higher shear strength.

The tests on the large natural fractures conducted under CNS condition were sheared up to 50 mm shear displacement with a significant increase of the normal stress. However, the CNS tests on the large specimens with the TI fractures were prematurely aborted between circa 22–38 mm of shear displacement since the capacity limit for the normal force of the machine was close, and the normal force still appeared to continue with increased shearing. The very rough fractures of the TI specimens generated a large dilation. The TI fractures were selected as an extreme case which confirmed that increased roughness yields an increased shear resistance despite high stresses. The effect of roughness can be compared in view of the study by Jiang et al. (2004).

In recent decades, most of the tests carried out on rock fracture shear strength, and the failure criteria developed, have been carried out under CNL conditions, such as Patton (1966), Barton and Choubey (1977), Grasselli and Egger (2003), Johansson and Stille (2014), Ríos-Bayona et al. (2021), and Zou and Cvetkovic (2023) to name a few. Only a limited number of tests have been carried out on rock fractures under CNS conditions and consequently few attempts have been made to model this case. Existing models derived from CNL experiments can capture an increasing shear strength given by dilatancy. However, they do not incorporate a non-constant dilatancy angle which is needed to control the shear strength development. A few constitutive models have especially been developed for CNS condition, see for example Saeb and Amadei (1990), Saeb and Amadei (1992), Seidel and Haberfield (2002), and Indraratna et al. (2005). However, there are several limitations in those models. Natural rock fractures have not been sampled in the experiments from which they were derived, and some of the models have only been validated against sample data from idealised saw-toothed fractures. Furthermore, in most cases, the models have only been validated against a few data under low normal loads (0–2 MPa) for soft rocks. This is especially important to be able to predict the shear strength of rock fractures at conditions corresponding to the planned repository for spent nuclear fuel in Forsmark. The dataset provided in this report can be used and support such research.

To this end, it remains to benchmark the performance of the existing constitutive models against experimental data obtained from tests on larger fractures of crystalline rock under high normal loads in the range of 5–10 MPa and under CNS condition. The existing models cannot account for the influence of mismatched fractures where aperture and roughness interact. New or refined constitutive models are most likely needed to obtain acceptable prediction capability at the given rock mass conditions. With the produced data regarding fracture properties (e.g. roughness, aperture, surface strength), although not fully processed within this project, future models may incorporate these parameters.

## 7.4    Scale effects

During the last decades, significant experimental research has been performed to study a potential scale effect on the peak shear strength of rock fractures. Despite these efforts, the mechanisms behind this potential scale effect are yet not completely understood and the findings are contradictory. For instance, various studies on the shear behaviour of rock fractures show that their peak shear strength decreases when the size of the tested specimens increases (negative scale effect) (Pratt et al. 1974, Barton and Choubey 1977, Bandis 1980, Bandis et al. 1981, Muralha and Pinto Da Cunha 1990, Yoshinaka et al. 1993, Ohnishi and Yoshinaka 1995, or Huang et al. 2020a). Kutter and Otto (1990) observed both negative and positive scale effects (i.e. increasing peak shear strength with increasing specimen size) when testing rock fractures with both poor and perfect match between their fracture surfaces, respectively. Both negative and positive scale effects have also been observed in tilt tests performed on two different rock types (Giani et al. 1995), and in direct shear tests performed at different levels of applied normal stress (Castelli et al. 2001). Johansson (2016) on the other hand, reported an absence of a scale effect in his experiments, while some studies suggest that the utilised sampling method may influence the conclusions reached regarding the scale effect (Yong et al. 2019, Huang et al. 2020b).

Due to these seemingly contradictory results, one of the main objectives in this project was to study if any scale effects could be observed in the mechanical properties of matched rock fractures, and especially on the shear strength. Moreover, the progressive dilatancy induced increased shear resistance at CNS tests also depends on specimen size. Altogether, 46 direct shear tests were performed at three different sample sizes (35 mm × 60 mm, 70 mm × 100 mm, and 300 mm × 500 mm). 24 tests were performed under CNS conditions and 22 tests under CNL conditions. In addition, both natural and tensile induced fractures were tested.

To be able to use all the tests to study a potential scale effect on the shear strength, this needs to be defined consistently in a way that results from both CNL and CNS can be used in the assessment. Here, the shear strength was defined as the shear strength at the onset of shearing. For the CNL tests, this point coincides with the peak shear strength. For the CNS tests, this point coincides with the shear stress just at the onset of a shear slip presumably before any asperity degradation occurs.

The point of onset of shearing can be identified by plotting the shear displacement of the actuator and the measured relative shear box displacement measured by LVDTs. As long as energy is stored in the system, the measured relative shear box displacement rate will deviate from the displacement rate of the actuator. Once friction is fully mobilised and shearing starts, the measured relative shear box displacement rate will gradually increase to the same rate as the actuator. The inflection point between these two phases of the measured relative shear box displacement defines the shear strength at the onset of shearing consistently for both CNL and CNS tests. By using this definition, it was possible to use the test results from all direct shear tests in the assessment of a potential scale effect on the shear strength.

To analyse if any scale effect could be observed, Larsson (2025) performed a three-factor analysis of variance (ANOVA) on the test results using the program SPSS. The test statistics was an F-test on the quotient between the mean square of the factor effect and the error sum of squares. A large quotient indicates an impact of the factor on the shear strength. The three factors that were analysed were fracture type, boundary condition and fracture size. One of the null hypotheses was that "the effect of fracture size on the shear strength is zero" and the hypothesis was tested at a 5 % level of significance. The results from the ANOVA analysis clearly showed that no scale effect could be observed. The F-value was 0.132 and the reject criterion for the hypothesis was $F > 3.22$. These results support findings presented by Johansson (2016); changes in (peak) shear strength are a function of the contact points (their size and number), which in turn are a function of the roughness, matedness and the relation between normal stress and the uniaxial compressive strength of the fracture surface.

The no scale effect contradicts some of the previous findings regarding the scale dependence of the peak shear strength of rock fractures. Another reason for this could have been that all the tests were performed under a high normal stress (5 MPa). However, if the scale corrections suggested by Barton and Bandis (1982) are used, assuming a JRC value of 20 for the tensile induced rock fractures and a UCS of 270 MPa, a reduction in the peak shear strength from 32° to 13° could be anticipated, when going from 35 mm × 60 mm to 300 mm × 500 mm sample sizes. Such a reduction cannot be seen if the results in Figure 6-5, Figure 6-9, and Figure 6-17 are studied. These figures suggest that the natural rock fractures have a significantly lower shear strength compared to the tensile induced fractures. This was expected since the natural rock fractures have a less rough surface compared to the tensile induced. The natural fractures also have a larger aperture and hence a poorer matedness. These results are in line with results presented by for example Zhao (1997a, b) and Ríos-Bayona et al. (2021).

Other reasons for the contradictory findings concerning the scale effect, as discussed by Larsson (2025), is that previous studies contain various types of uncertainties which may influence the interpretation of the results. One such uncertainty is the combination of in-situ testing and laboratory testing. In in-situ testing, as illustrated in the study by Krsmanovic and Milovan (1966), the test conditions can be challenging to control. If in-situ testing and laboratory testing are combined, as done in for example Pratt et al. (1974), Yoshinaka et al. (1993), and Sanei et al. (2015), these uncertainties will potentially be embedded in wrong conclusions. Another type of uncertainty is if the same specimen is used in multiple tests, as done in for example, Locher and Urs (1970), Leichnitz and Natau (1979), and Ohnishi and Yoshinaka (1995). A third type of uncertainty arises if the results are based on replicas, as done by for example Kutter and Otto (1990), Ohnishi et al. (1993), Castelli et al. (2001), Ueng et al. (2010), Azinfar et al. (2019), and Huang et al. (2020a), without performing any geometric quality assurance method on the replica manufacturing, as suggested by Larsson et al. (2023a, b). A final type of uncertainty arises due to the absence of a statistically representative number of tests. Despite this, most studies only present results from single measurements or means, which may lead to incorrect conclusions. All these uncertainties have been reduced in the present study. Several direct shear tests have been performed for each type of sample, which enabled a statistical evaluation of the scale effect. Also, unique rock specimens have been used for each test, and the same material has been used in all tests under controlled laboratory conditions. However, only granite from the Flivik quarry was tested in this study. It may be possible that other results would be obtained concerning the scale effect if fractures in other types of intact rock were tested. Further studies are therefore recommended to verify the findings in this study.

A progressively increased shear strength due to shear-induced dilation in CNS tests and the effect of fracture scale was seen in the tests of large rock fractures. The tests of the natural fractures saw an increase of shear resistance from an initial shear strength value of 6.6–7.9 MPa to a peak value of 12–17 MPa reached at a shear displacement between 20–40 mm. The corresponding results for the tests on the tensile induced fractures were an initial shear strength of 13.4–16.5 MPa to 17–23 MPa when the shear tests were aborted at 22–38 mm shear displacement. The total shear strength increases due to CNS condition compared with the tests at CNL condition can be said to generate a dilation-induced strengthening effect from 6 to 13–16 MPa for the natural fractures and 10 to 17–23 MPa for the tensile induced fractures and reached within a shear displacement less than 40 mm. This is roughly about a factor of two. The similar strengthening effect associated with dilation for the inter-mediate and small-scale specimens is small or negligible. It was seen that the peak shear strength was obtained at less than 10 mm shearing. The scale is thus important to exploit the dilation-induced strengthening effect. To fully study this potential strengthening effect at the given initial normal stress and rock mass stiffness for the natural fractures (with a similar roughness) at 50 mm shear would require larger (longer) specimens assuming that the scaling continues at further upscaling.

For rough fractures as the tensile induced fractures, the capacity of the current equipment sets the limit if these fracture types are going to be further investigated in the same equipment. One option to keep within the normal force limitation is to decrease the imposed rock mass stiffness which would yield a reduced dilation-induced strengthening. Another option might be to increase the maximum normal force in the equipment by a modification. That would require an adaption of the current test system.

Finally, the normal and shear stiffness were also determined at three scales. Without deeper analyses, it appears that there is no obvious scale effect that can be seen. This could be confirmed (or rejected) by a statistical analysis like the ANOVA made of the shear strength.

## 7.5    The use of replicas as representative samples

Replicas are useful for parametric investigations on the shear mechanical behaviour of rock fractures, which are unique by nature. Nevertheless, only a limited number of studies have addressed, in a quantitative way, the geometric quality of rock fracture replicas. Motivated by these facts, a method for geometric quality assurance of rock fracture replicas (Larsson et al. 2023a, b) was developed as part of this project, through the introduction of two quality assessment parameters ($\sigma_{mf}$ and $V_{Hp100}$, which were experimentally validated by means of direct shear tests.

In terms of geometric quality assessment, previous studies like Jiang et al. (2016) investigated the geometric error between the mother rock fracture and corresponding replica through the mean of the absolute values of the coordinate points with respect to the best-fit plane for each dataset. However, as observed from the analyses included in this project, the consideration of absolute values prevents obtaining information about which value the deviations are distributed around. The calculation of errors between two fracture surfaces from individual best-fit planes, as suggested by Jiang et al. (2016) was also observed to introduce imprecisions. It was also seen that using the mean of the deviations of coordinate points, as a geometric quality assurance parameter is unsuitable, since two apparently different surfaces could have the same mean.

From the analysis of other results from Huang et al. (2020a), directional surface roughness parameters were also found inappropriate for describing morphological deviations between fractures. One-to-one comparisons of coordinate points, through $\sigma_{mf}$ parameter as suggested in this report, are required to account for the spatial deviation between fractures surfaces. The novel method summarised in this report and published elsewhere (Larsson et al. 2023a, b) ensures reliable manufacturing of fracture replicas, especially useful for parameter studies.

With reference to the results presented in Figure 6-21, a remarkably similar shear behaviour, not presented so far in other published works to the best of the authors' knowledge, can be observed in results from specimens RNM-N1-CNL-5 and RNM-N1-CNL-6. The shear mechanical behaviour of these two specimens (shear stiffness, peak shear displacement and shear stress at the residual stage) is fairly similar to that shown by the natural rock fracture (N1-CNL), even though slight differences

in peak shear values are observed. These differences cannot be explained based on surface comparisons, neither on morphological differences, dilation or rotation, and neither on differences in compressive strength or basic friction angle (in turn, higher for the concrete material saw-cut planar fracture). Other aspects associated with differences in fracture toughness could be behind these discrepancies and may be captured through quasi-static toughness testing.

More relevant differences in shear behaviour are observed for replicas RNM-N1-CNL-1 to RNM-N1-CNL-4 in Figure 6-21 when compared to the rest of the results. Despite being manufactured in the same way, some shortcomings during the manufacturing process of these specimens caused geometric deviations and, therefore, a reduction in matedness that affected the shear behaviour.

Regarding the perfectly matched replicas tested under CNL conditions and as shown by Figure 6-21a, clear peaks on the shear strength can be seen for the three tested specimens at about 0.5 mm of displacement, and similar behaviour in terms of normal displacement with shearing (dilation). The effect of slight variations in matedness and aperture is clearly visible here. If a simple analysis of peak shear strengths in Figure 6-21 is considered, differences in mobilised peak friction angle (as derived from the shear stress-normal stress ratio) for RPM-type fractures (average peak stress about 5.5 MPa) and N1-CNL (shear stress about 4.9 MPa) are in the range of 3°, and even higher (~9°) if RPM-type fractures are compared with the RNM-type ones. These results bring to light that even subtle differences in matedness and aperture can significantly influence the fracture shear behaviour. These observations were also confirmed by Ríos-Bayona et al. (2021), and can be seen from the analysis of Figure 7-1b, where it is shown that differences in fracture aperture (0 to 0.5 mm), cause significant variations on the peak friction angle for several fractures, and in a similar range of values as observed herein.

The main limitation of the experimental program with replica fractures was related to the specimen sizes. Even though the original project plan included large-scale testing of replicas, only specimens of a given size (70 mm × 100 mm) were used, and no large-scale shear tests on replicas were possible to perform. The experience gained with the experimental program performed with these specimen size, together with budget and time constraints implied abandoning the large-size testing program. Another limitation associated with these tests was the maximum shearing displacement attained (about 10 mm), which is far from the 50 mm shear displacement aimed initially. Overall, being able to perform parametric studies was deemed not relevant for attaining the project objectives, especially since no scale effect could be observed on the shear strength of rock fractures according to the statistical assessment of the experimental results.
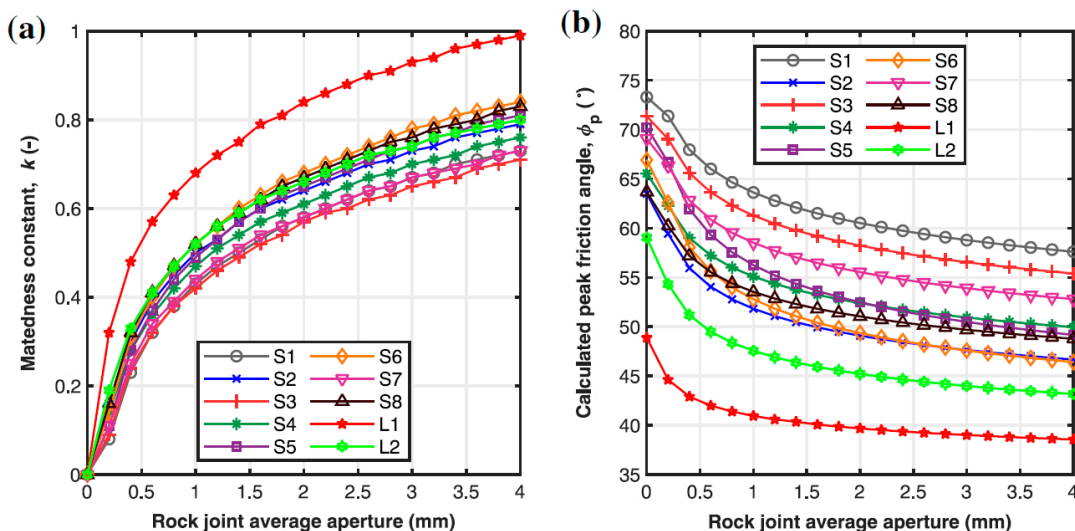


*Figure 7-1.* *Comparison between (a) matedness constant (k) and rock fracture average aperture, and (b) calculated peak friction angle and rock fracture average aperture on fracture samples taken from the foundation at the Storfinnforsen buttress dam (© Ríos-Bayona et al. (2021) CC–BY 4.0, https://creativecommons.org/licenses/by/4.0)*

## 7.6 General aspects

In general, previous datasets from other studies of direct shear testing are lacking one or several parameters from the characterisation of the samples. For example, even if high resolution optical scanning has been performed, the scanning data has not been arranged in a global coordinate system to enable determination of fracture aperture of the samples. This, in combination with the uncertainties involved in many of the previous studies mentioned in Section 7.3, implies both that it may be difficult to compare different failure criteria against each other, or to assess their accuracy. It also makes it more difficult to develop new failure criteria and constitutive models for rock fractures. Therefore, one of the objectives of this report was to provide a comprehensive and well documented dataset using best available standards and techniques for future research to enable future improvement on existing constitutive models and development of new ones.

The main aim of this project was to experimentally investigate the mechanical properties of rock fractures by conducting high-quality laboratory direct shear testing under conditions representative for the nuclear waste repository planned at Forsmark. Consequently, no assessment of existing constitutive models, or development of new ones, were covered within this project. It is recommended that the dataset provided by this project are used by the research community in developing new constitutive models for fracture behaviour, especially for CNS conditions where limited research has been performed.

Natural fractures in a rock mass constitute a complex mechanical system which we today are only able to partly represent. By continuously performing systematic high-quality research on aspects where our knowledge is limited, we will be able to better represent this complex mechanical system. However, due to budget and time constrains it was not possible to cover all aspects on fracture behaviour in the testing programme. Further aspects that need to be studied in future research are the influence from lower normal stresses, especially in combination with the new DIC measurements, as well as the influence from rock bridges, mineral coatings, and fracture infilling materials. It should also be noted that all direct shear test in the project were performed at a constant shear rate. More rapid shear rates, as may be the case in earthquakes, may influence the shear behaviour of the rock fractures obtained in this project.

# 8 Conclusions and recommendations for future work

From a geomechanical point of view, a safe and efficient design of an underground spent nuclear fuel repository requires, among other aspects, sound predictions of potential displacement of surrounding rock fractures in the rock mass. A 50 mm shear displacement induced by one or several post-glacial earthquakes is considered a threat to the copper canister integrity in the context of KBS-3 repository concept, according to SKB (2011). The groundwater flow can also be affected by thermal, glacial or seismic-induced normal and shear fracture displacements. To be able to make these predictions of the fracture displacements, data on fracture behaviour tested under conditions representative for repository depth is needed to assess existing constitutive models and validate new ones.

## 8.1 Meeting the project objectives

In this project, a comprehensive high-quality laboratory testing program comprising normal loading and direct shear tests of rock fractures and replicas under geomechanical conditions representative for the nuclear waste repository at stress and rock mass stiffness representative at 400–500 m depth in a crystalline, hard rock mass has been successfully developed and executed. There were five main objectives for the project (Section 1.3):

1. Develop a laboratory equipment for conducting well-controlled normal loading and shear tests on large rock fracture specimens and their replicas at relatively large normal stresses under CNL and CNS conditions while allowing a 50 mm shear displacement: A large shear testing equipment was developed, manufactured and validated by try-out tests and reference shear tests to validate its performance. The ability to conduct well-controlled normal loading and shear tests with accurate measurements with the given requirements were confirmed.

2. Determine the mechanical behaviour of large rock fractures subjected to 50 mm of shear displacement including shear strength, normal and shear stiffness, and dilation under CNS and CNL conditions to verify the strengthening due to dilation effects under CNS conditions: Shear tests were conducted on natural fractures with small amount of weathering and little infill material, as well as on tensile induced rough, fresh rock fractures. These two types of fractures represent two cases, one representing the case of a natural fracture, more typical to the repository conditions and the other one representing an ultimate case with respect to expected roughness and dilation. The results from the shear tests showed a clear dilation-induced strengthening effect with a factor of approximately two within 30–50 mm shear displacement by using CNS condition at an initial normal stress of 5 MPa and an equivalent rock mass stiffness of 10 MPa/mm compared to test performed under CNL conditions. As expected, this dilation-induced strengthening effect was more pronounced in the tensile induced fracture compared to the natural ones.

3. Clarify if any scale effect could be observed on the mechanical parameters when samples on rock fractures of different sizes were tested: Shear tests were conducted on both natural and tensile induced fractures at three scales. The fractures of the two types at the three scales were sampled of the same fracture sets respectively. By a statistical analysis it was clarified that there was no effect of scale on the shear strength defined as the onset of full shear slip with a 95 % significance. There is a clear scale effect when the strengthening due to shear induced dilation is considered in the CNS tests. The medium and small-scale specimen cannot capture the same magnitude of this strengthening effect as seen in the tests of the large-scale specimens.

4. Investigate if replicas are suitable to use for parameter investigations of the mechanical properties of hard rock fractures: Replicas of a medium scale rock fracture were manufactured. After the development stages of the manufacturing process, two types of replicas were manufactured in ultra-high strength concrete: (1) natural match which are replicas of each side of a fracture individually copied, and (2) perfect match fractures which means that one side is copied of a rock fracture and the other side is copied on the fracture replica. The effective aperture in the natural match replica appears to be larger than the rock fracture, whereas the replica with the perfect match replica appears to be smaller than the rock fracture. The replica manufacturing method, in combination with a novel method for geometric quality assessment developed within the project, are suitable to use for further parameter studies.

5. Generate a comprehensive and well-documented dataset using best available standards and techniques for future research to enable future improvement on existing constitutive models and development of new ones, and also to help in the development and validation of detailed numerical models for simulation of fracture behaviour: A comprehensive set of 46 direct shear tests on natural and artificially tensile-induced rock fractures of three different sample sizes were conducted under both CNL and CNS conditions. Parallel to the mechanical investigations, further characterisations were made such as high-resolution geometry scanning of the fracture surfaces before and after testing, contact pressure distribution measurements and acoustic emission measurements. The mechanical tests were evaluated, whereas some of the evaluations of the other data is partly in progress. Several methods are either novel or of state-of-the-art character.

It is concluded that the main objectives of the project were fulfilled. Moreover, several other important findings were obtained. Further and more detailed descriptions of all main achievements within the project are described in the following subsection.

## 8.2 Main achievements within the project

The project has spanned over several technical areas and extended over several years and generated increased knowledge and experience of tests on rock fractures. Several achievements were obtained during the work. The main achievements are listed below.

### 8.2.1 Importance of local fracture displacement measurements

- A novel method for measuring normal and shear displacements directly over the fracture were developed using Digital Image Correlation (DIC). This method enabled us to perform local measurements which yields a higher accuracy, since no correction of measured values due to the inclusion of system deformations in the measured values is needed as is required for non-local methods.

- The results from the local fracture displacement measurements, versus non-corrected non-local measurements, where relative shear box displacements are measured demonstrate the effect of incorrectly including system deformations. Significantly higher normal and shear stiffnesses of the fractures are obtained with the local measurements compared with the uncorrected non-local measurements.

- The accurate local fracture displacement measurements identify new possibilities for detailed analyses of the deformation processes that takes place during the normal loading tests and the early stage of the direct shear tests. These analyses can result in an increased understanding of the deformation processes in the fracture, especially with access to additional data such as fracture geometry and contact pressure distributions.

### 8.2.2 Mechanical tests on large rock fractures

- New and unique custom-built equipment were designed and manufactured for normal loading and direct shear tests of specimens of hard rock fractures up to $400 \times 600$ mm. Some of the design requirements were given from the project and additional requirements were defined based on several years of experimental experience at RISE, such as high stiffness and tolerances, accurate fracture deformation measurements, concurrent acoustic emission measurements, to be able to obtain rich and high-quality data. The properties and performance were verified by tests on reference specimens.

- Large-scale specimens of fractures in hard, crystalline rock with a size of $300 \times 500$ mm were tested under normal loading and direct shear tests at stress levels representative for repository depth under both CNS and CNL conditions. The results from the tests display a good control of the whole experimental process chain starting from acquiring large specimens with undisturbed natural fractures and tensile induces fractures, fixing the specimens in the holders, scanning fracture surfaces and repositioning the fractures to a fully mated state before the mechanical tests.

- The results from the experiments are novel since there are no comparable data for this large specimen size and stress levels found elsewhere. The results constitute an important contribution for investigating scale effects on deep located fractures.

### 8.2.3    Effect of CNS and scale at direct shear tests

- An instant strengthening effect on the shear strength was observed at the onset of shearing (within 0.3–0.4 mm shear displacement) at the CNS loading condition compared to the CNL loading condition. The strengthening was caused by a dilation induced increase of the normal stress by approximately 2 MPa. There were some small variations between the specimens.

- The strengthening effect on the shear strength due to dilation after fully mobilised shear slip (at approximately 30–50 mm of shear displacement) for the tested fractures under CNS conditions were verified for the large-scale specimens. For the natural fractures, a "residual" shear strength in the range of 12–17 MPa was observed, while it was 17–23 MPa for the tensile induced fractures. This is significantly higher than the residual strength of slightly under 4 MPa observed in the CNL tests for the same type of fractures.

- To study the dilation-induced shear strengthening effect at CNS conditions for shear displacements in the order of 50 mm for the studied fracture types, fracture sizes (lengths), in the order of the one for the large-scale specimens or larger, is needed. The test results for the medium and small size specimens show that those smaller sample sizes are not sufficient to produce 50 mm shear displacement.

- There is no observed effect of fracture size on the shear strength (defined as the onset of fully mobilised shear slip) for the tested rock fractures and used loading conditions. The result obtained from the statistical analysis was clear on this point. The rationale behind this is that local conditions at the asperity level at the onset of shearing are constant or invariant and independent of the fracture size.

- No observed scale effect implies that the shear strength can be determined by performing multiple tests on smaller sample sizes and calculating their average value. However, if the residual strength at a 50 mm shear displacement intends to be studied, large sample sizes are needed, as mentioned above.

### 8.2.4    Replicas of hard rock fractures

- A method for manufacturing replicas of rock fractures made of high-strength concrete resembling the properties of a crystalline rock and novel quality assurance method were developed. With this, high-quality replicas can be manufactured with excellent geometrical control. This enables to capture the mechanical behaviour of the rock fracture making them suitable for parametric investigations.

- Two types of replicas, with natural match and perfect match, respectively, were developed. The natural match provides a fracture replica with slightly poorer matching fracture surfaces (resembling more weathered fractures) than for the original rock fracture and the perfect match provides a fracture replica with better matching fracture surfaces than for the original rock fracture.

- The manufacturing techniques were gradually improved to, in the end, yield fracture surfaces with few or no defects such as pores caused by air bubbles in the concrete. Moreover, the final specimens had no distorted surfaces as was in the case for the first manufactured specimens. The believe is that nearly identical copies can be manufactured.

- The shear tests on replicas revealed a very high sensitivity of the fracture geometry on the shear properties. Natural match replicas versus rock fractures with almost perfect geometric replication of the natural rock fracture surface (geometrical deviation roughly within ±0.1 mm of the surface geometry) had a lower peak shear strength of approximately 4 MPa compared to the natural rock fracture sample which had a peak shear strength of 4.9 MPa. The replicas with perfect match on the other hand had a peak shear strength with an average value of approximately 5.5 MPa. The main reason for the difference seems to be related to the small differences in the effective aperture distribution (matching). Other contributions for this discrepancy may be due to differences in material properties between rock and concrete such as strength, fracture toughness and friction coefficient.

- Despite that a perfect copy of the original rock fracture surface geometries could not be achieved, the individual copies of the replicas are expected to be small. This needs to be confirmed by a larger study where several igentical fracture replicas are manufactured and its geometrical variations quantified. Moreover, the two replica types provide means to systematically study the behaviour of fractures e.g. by various loading schemes, with both high matching and with lower matching.

## 8.3 Future work

In this summary report, a comprehensive and well documented dataset of results from direct shear tests is presented, using best available standards and techniques. Since it is important to be able to predict the shear strength of rock fractures at conditions corresponding to the planned repository for spent nuclear fuel, this dataset can be used to investigate how well existing constitutive models for constant stiffness conditions can predict the shear strength of a fracture in hard crystalline rock. The dataset can also be used to develop new constitutive models that can consider how roughness, aperture, surface strength and normal stress interact.

However, due to budget and time constrains it was not possible to cover all aspects on fracture behaviour in the testing programme and to test all types of fractures. In the performed study, only samples from two natural fractures were tested coming from the Flivik quarry. No fractures coming from the rock mass at the planned repository at Forsmark were tested. Additional testing on fractures from the Forsmark area will be needed in the future to produce data representative for the conditions at Forsmark. Further aspects that need to be studied in future research are, for example, the influence from lower normal stresses, especially in combination with the new DIC measurements, as well as the influence from rock bridges, mineral coatings, and fracture infilling materials. It should also be noted that all direct shear tests in the project were performed at a constant shear rate. More rapid shear rates, as may be the case in earthquakes, may influence the shear behaviour of the rock fractures obtained in this project.

# References

SKB's (Svensk Kärnbränslehantering AB) publications can be found at www.skb.com/publications. SKBdoc documents will be submitted upon request to document@skb.se.

**Alejano LR, Pérez-Rey I, 2025.** Basic friction angle of intact granitic rock and concrete planar contacts by means of tilt testing – Final Report, University of Vigo. SKBdoc 2072352 ver 1.0, Svensk Kärnbränslehantering AB.

**Alejano L, Muralha J, Ulusay R, Li C C, Pérez-Rey I, Karakul H, Chryssanthakis P, Aydan Ö, 2018.** ISRM Suggested Method for Determining the Basic Friction Angle of Planar Rock Surfaces by Means of Tilt Tests. Rock Mechanics and Rock Engineering 51, 3853–3859.

**ASTM, 2004.** ASTM D7012-04 – Standard Test Method for Compressive Strength and Elastic Moduli of Intact Rock Core Specimens under Varying States of Stress and Temperatures. ASTM.

**ASTM, 2008.** ASTM D2936-08 – Standard Test Method for Direct Tensile Strength of Intact Rock Core Specimens. ASTM.

**ASTM, 2016.** ASTM D3967-16 – Standard Test Method for Splitting Tensile Strength of Intact Rock Core Specimens. ASTM.

**Aydin A, 2014.** ISRM Suggested Method for Determination of the Schmidt Hammer Rebound Hardness: Revised Version. In: R Ulusay, Ed. The ISRM Suggested Methods for Rock Characterization, Testing and Monitoring: 2007-2014. Springer, pp. 25–33.

**Aydin A, Basu A, 2005.** The Schmidt hammer in rock material characterization. Engineering Geology 81(1), 1–14.

**Azinfar M, Ghazvinian A, Nejati H, 2019.** Assessment of scale effect on 3D roughness parameters of fracture surfaces. European Journal of Environmental and Civil Engineering 23(1), 1–28.

**Bahaaddini M, Hagan P, Mitra R, Hebblewhite B, 2014.** Scale effect on the shear strength behaviour of rock joints based on a numerical study. Engineering Geology 181, 212–223.

**Bandis S, 1980.** Experimental Studies of Scale Effects on Shear Strength, and Deformation of Rock Joints. Leeds, UK: The University of Leeds.

**Bandis S, Lumsden A C, Barton N R, 1981.** Experimental studies of scale effects on the shear behaviour of rock joints. International Journal of Rock Mechanics and Mining Sciences & Geomechanics Abstracts 18, 1–21.

**Barton N, Bandis S, 1982.** Effects of block size on the shear behaviour of jointed rock. Proceedings of the U.S Symposium on Rock Mechanics (USRMS), Berkeley, California, August 1982. ARMA-82-739, 739–760.

**Barton N, Choubey V, 1977.** The shear strength of rock joints in theory and practice. Rock Mechanics 10, 1–54.

**Basu A, Aydin A, 2004.** A method for normalization of Schmidt hammer rebound values. International Journal of Rock Mechanics and Mining Sciences, 41(7), pp. 1211–1214.

**Castelli M, Re F, Scavia C, Zaninetti A, 2001.** Experimental evaluation of scale effects on the mechanical behavior of rock joints. Espoo, Finland, CRC Press, p. 205–210.

**Dearman W R, Irfan T Y, 1978.** Assessment of the degree of weathering in granite using petrographic and physical index tests. In Proceedings of the International Symposium on Deterioration and Protection of Stone Monuments. Unesco, Paris. Paper 2.3, 1–35.

**Flansbjer M, Williams Portal N, Larsson J, Jacobsson L, Hanquist C, 2024.** Parametrization of Structures 2 – Normal loading and direct shear tests on intermediate size on high-strength replicas of a natural rock fracture in laboratory. RISE rapport 2024: 28, Borås, Sweden: Research Institutes of Sweden AB.

**Fujifilm Corporation, 2019.** Prescale. Pressure measurement film. https://www.fujifilm.com/es/en/business/inspection/measurement-film/prescale

**Gercek H, 2007.** Poisson's ratio values for rocks. International Journal of Rock Mechanics and Mining Sciences 44(1), 1–13.

**Giani G, Ferrero A, Passarella G, Reinaudo L, 1995.** Scale effect evaluation on natural discontinuity shear strength. Lake Tahoe, California, US, CRC Press, p. 447–452.

**Glamheden R, Fredriksson A, Röshoff K, Karlsson J, Hakami H, Christiansson R, 2007.** Rock Mechanics Forsmark. Site descriptive modelling Forsmark stage 2.2. SKB R-07-31, Svensk Kärnbränslehantering AB.

**GOM, 2018.** GOM Inspect Professional. Shape and dimension analysis, 3D inspection and mesh processing for 3D point clouds and CAD data sets. GOM GmbH, Braunschweig, Germany.

**Goodman RE, 1976.** Methods of Geological Engineering in Discontinuous Rocks. California, US, West Publishing Company, 484 p.

**Grasselli G, Egger P, 2003.** Constitutive law for the shear strength of rock joints based on three-dimensional surface parameters. International Journal of Rock Mechanics and Mining Sciences 1(40), 25–40.

**Huang M, Hong C, Du S, Luo Z, 2020a.** Experimental Technology for the Shear Strength of the Series-Scale Rock Joint Model. Rock Mechanics and Rock Engineering 53, 5677–5695.

**Huang M, Hong C, Ma C, Luo Z, Du S, Yang F, 2020b.** A new representative sampling method for series size rock joint surfaces. Scientific Reports 10, Article number: 9129.

**Indraratna B, Haque A, Aziz N, 1999.** Shear behaviour of idealised infilled joints under constant normal stiffness. Géotechnique 49(3), 331–355.

**Indraratna B, Thirukumaran S, Brown E T, Zhu S P, 2015.** Modelling the shear behaviour of rock joints with asperity damage under constant normal stiffness. Rock Mechanics and Rock Engineering 48(1), 179–195.

**ISO, 2012.** ISO 25178–2:2012 – Geometrical product specifications (GPS). Surface texture: Areal. Part 2: Terms, definitions and surface texture parameters. Geneva: ISO.

**ISRM, 2007.** Suggested Methods for Determining Shear Strength. In: Ulusay R, Hudson J, Eds. The Complete ISRM Suggested Methods for Rock Characterization, Testing and Monitoring: 1974–2006. Ankara: Turkey, ISRM, 628.

**Jacobsson L, 2016.** Parametrisation of Fractures – Direct Shear Tests on Calcite and Breccia infilled Rock Joints from Äspö HRL under Constant Normal Stiffness Condition. Workreport 2016-19, Eurajoki, Finland: Posiva OY.

**Jacobsson L, Flansbjer M, 2005.** Forsmark site investigation. Borehole KFM05A. Normal stress test with direct and indirect deformation measurement together with shear tests on joints. SKB P-05-141, Svensk Kärnbränslehantering AB.

**Jacobsson L, Glamheden R, Hakami E, Olofsson I, 2012.** Rock mechanics laboratory testing in SKB site investigation program. Stockholm, Sweden, Stiftelsen Bergteknisk Forskning – BeFo.

**Jacobsson L, Mas Ivars D, Kasani H K, Johansson F, Lam T, 2021.** Experimental program on mechanical properties of large rock fractures. Turin: Italy, IOP Publishing Ltd.

**Jacobsson L, Flansbjer M, Larsson J, 2023.** Direct shear tests on large natural and artificially induced rock fractures in a new laboratory equipment. Salzburg: Austria, ÖGG Österreichische Gesellschaft für Geomechanik.

**Jacobsson L, Larsson J, Flansbjer M, Hanquist C, 2024a.** Parametrization of Structures 2 – Normal loading and direct shear tests on large natural and tensile induced rock fractures in laboratory, RISE rapport 2024:30., Borås, Sweden: Research Institutes of Sweden AB.

**Jacobsson L, Larsson J, Flansbjer M, Hanquist C, 2024b.** Parametrization of Structures 2 – Normal loading and direct shear tests on small and intermediate size natural and tensile induced rock fractures in laboratory. RISE rapport 2024: 29, Borås, Sweden: Research Institutes of Sweden AB.

**Jacobsson L, Larsson J, Williams N, 2024c.** Parametrization of Structures 2 – Extraction of rock specimens with natural and tensile induced fractures from quarried granite blocks. RISE rapport 2024:27, Borås, Sweden: Research Institutes of Sweden AB.

**Jiang Q, Feng X, Gong Y, Song L, Ran S, Cui J, 2016.** Reverse modelling of natural rock joints using 3D scanning and 3D printing. Computers and Geotechnics 73, 210–220.

**Jiang Y, Xiao J, Tanabashi Y, Mizokami T, 2004.** Development of an automated servo-controlled direct shear apparatus applying constant normal stiffness condition. International Journal of Rock Mechanics and Mining Sciences 41, 275–86.

**Johansson F, 2016.** Influence of scale and matedness on the peak shear strength of fresh, unweathered rock joints. International Journal of Rock Mechanics and Mining Sciences 82, 36–47.

**Johansson F, Stille H, 2014.** A conceptual model for the peak shear strength of fresh and unweathered rock joints. International Journal of Rock Mechanics and Mining Sciences 69, 31–38.

**Kahraman S, 1996.** Basınç direnci tahmininde Schmidt ve nokta yük indeksi kullanmanın güvenilirliği. In: S. Korkmaz, M. Akçay (Eds.), K.T.Ü. Jeoloji Mühendisliği Bölümü 30. Yıl Sempozyumu, Trabzon, 362–369 (In Turkish).

**Krsmanovic D, Milovan P, 1966.** Large Scale Field Tests of the Shear Strength of Limestone. Proceedings of the 1st ISRM Congress, 773–779. Lisbon, Portugal.

**Kutter H, Otto F, 1990.** Influence of parallel and cross joints on shear behaviour of rock discontinuities. In: Barton N, Stephansson O, Eds. Rock joints. Loen, Norway. Rotterdam: A.A. Balkema, 243–250.

**Larsson J, 2021.** Experimental investigation of the system normal stiffness of a 5 MN direct shear test setup and the compensation of it in CNS direct shear tests. IOP Conference Series: Earth and Environmental Science. Volume 833, Paper presented at the EUROCK 2021: Mechanics and Rock Engineering, from Theory to Practice 20–25 September 2021, Turin, Italy.

**Larsson J, 2025.** Approaches for increased accuracy in laboratory direct shear testing of rock joints. PhD Thesis. Royal Institute of Technology (KTH), Stockholm, Sweden.

**Larsson J, Flansbjer M, 2020.** An Approach to Compensate for the Influence of the System Normal Stiffness in CNS Direct Shear Tests. Rock Mechanics and Rock Engineering 53, 2185–2199.

**Larsson J, Johansson F, Mas Ivars D, Johnson E, Flansbjer M, Portal N W, 2023a.** A novel method for geometric quality assurance of rock joint replicas in direct shear testing – Part 1: Derivation of quality assurance parameters and geometric reproducibility. Journal of Rock Mechanics and Geotechnical Engineering 15(9), 2193–2208.

**Larsson J, Johansson F, Mas Ivars D, Johnson E, Flansbjer M, Portal N W, 2023b.** A novel method for geometric quality assurance of rock joint replicas in direct shear testing – Part 2: Validation and mechanical replicability. Journal of Rock Mechanics and Geotechnical Engineering 15(9), 2209–2223.

**Leichnitz W, Natau O, 1979.** The Influence of Peak Shear Strength Determination On The Analytical Rock Slope Stability. Paper presented at the 4th ISRM Congress, Montreux, Switzerland. September 1979.

**Locher H, Urs G, 1970.** Shear Tests on Layered Jurassic Limestone. Paper presented at the 2nd ISRM Congress, Belgrade, Yugoslavia. September 1970.

**Magsipoc E, Zhao Q, Grasselli G, 2020.** 2D and 3D Roughness Characterization. Rock Mechanics and Rock Engineering 53, 1495–1519.

**Mas Ivars D, Lope Álvarez D, Sánchez Juncal A, Ghazal R, Damjanac B, 2015.** Parametrisation of Fractures – Estimation of fracture shear displacement due to excavation of new slots at the TASQ tunnel via numerical modelling, workreport 2015-28, Eurajoki, Finland: Posiva OY.

**Muralha J, Pinto Da Cunha A, 1990.** About LNEC experience on scale effects in the mechanical behaviour of joints. Proceedings of the First International Workshop on Scale Effects in Rock Masses. Loen, Norway. June 7–8. Balkema, Rotterdam,

**Muralha J, Grasselli G, Tatone B, Blümel M, Chryssanthakis P, Yujing J, 2014.** ISRM Suggested Method for Laboratory Determination of the Shear Strength of Rock Joints: Revised Version. Rock Mechanics and Rock Engineering 47, 291–302.

**Nadan B J, Engelder T, 2009.** Microcracks in New England granitoids: A record of thermoelastic relaxation during exhumation of intracontinental crust. Bulletin of the Geological Society of America, 121(1-2), 80–99.

**Ohnishi Y, Yoshinaka R, 1995.** Laboratory investigation of scale effect in mechanical behavior of rock joint. Vienna, Austria, u.n., p. 465–470.

**Ohnishi Y, Herda H, Yoshinaka R, 1993.** Shear strength scale effect and the geometry of single and repeated rock joints. Lisbon, Portugal.

**Patton F D, 1966.** Multiple modes of shear failure in rock. In Proceedings of the 1st ISRM Congress, Lisbon, Portugal.

**Pratt H, Black A, Brace W, 1974.** Friction and deformation of jointed quartz diorite. Denver, US, u.n., p. 306–310.

**Ríos-Bayona F, Johansson F, Mas Ivars D, 2021.** Prediction of shear strength of natural, unfilled rock joints accounting for matedness based on measured aperture. Rock Mechanics and Rock Engineering 54, 1533–1550.

**Saeb S, Amadei, B, 1990.** Modelling joint response under constant or variable normal stiffness boundary conditions. International Journal of Rock Mechanics and Mining Sciences & Geomechanics Abstracts 27(3), 213–217.

**Saeb S, Amadei B, 1992.** Modelling rock joints under shear and normal loading. International Journal of Rock Mechanics and Mining Sciences & Geomechanics Abstracts 29(3), 267–278.

**Sanei M, Faramarzi L, Fahimifar A, Goli S, Mehinrad A, Rahmati A, 2015.** Shear strength of discontinuities in sedimentary rock masses based on direct shear tests. International Journal of Rock Mechanics and Mining Sciences 75, 119–131.

**Seidel J P, Haberfield C M, 2002.** A theoretical model for rock joints subjected to constant normal stiffness direct shear. International Journal of Rock Mechanics and Mining Sciences 39(5), 539–553.

**Siren T, Hakala M, Valli J, Christiansson R, Mas Ivars D, Lam T, 2017.** Parametrisation of fractures – Final report, Posiva 2017-01. Eurajoki, Finland: Posiva.

**SIS, 2000.** Swedish Standard SS 137245 – Concrete testing – Hardened concrete – Shrinkage. Swedish Institute for Standards (SIS).

**SKB, 2011.** Long term safety for the final repository for spent nuclear fuel at Forsmark.Main report of the SR-site project. SKB TR-11-01, Svensk kärnbränslehantering AB.

**Sutton M, Orteu J, Schreier H, 2009.** Image Correlation for Shape, Motion and Deformation Measurements: Basic Concepts, Theory and Applications. Springer, Verlag.

**Ueng T S, Jou Y J, Peng I, 2010.** Scale effect on shear strength of computer-aided manufactured joints. Journal of Geoengineering 5, 29–37.

**Valli J, Hakala M, 2016.** Parametrisation of fractures – Model generation methodology and prediction calculations. Workreport 2016-32, Eurajoki, Finland: Posiva OY.

**Valli J, Hakala M, Suikkanen J, Mattila J, Heine J, Simelius C, 2016.** Parametrisation of Fractures – PUSH Test Execution and Back Analysis. Workreport 2016-52, Eurajoki, Finland: Posiva OY.

**Yong R, Qin J-B, Huang M, Du S-G, Liu J, Hu G-J, 2019.** An innovative sampling method for determining the scale effect of rock joints. Rock Mechanics and Rock Engineering 52, pp. 935–946.

**Yoshinaka R Y J, Arai H, Arisaka S, 1993.** Scale effects on shear strength and deformability of rock joints. In Proceedings of the 2nd International Scale Effects in Rock Masses. Lisbon, Portugal, CRC Press, London, 143–149.

**Zangerl C, Evans KF, Eberhardt E, Loew S, 2008.** Normal stiffness of fractures in granitic rock: A compilation of laboratory and in-situ experiments. International Journal of Rock Mechanics and Mining Sciences, 45(8), 1500–1507.

**Zhao J, 1997a.** Joint surface matching and shear strength part A: joint matching coefficient (JMC). International Journal of Rock Mechanics and Mining Sciences 34, 173–178.

**Zhao J, 1997b.** Joint surface matching and shear strength part B: JRC-JMC shear strength criterion. International Journal of Rock Mechanics and Mining Sciences 34, 179–185.

**Zou L, Cvetkovic V, 2023.** A new approach for predicting direct shear tests on rock fractures. International Journal of Rock Mechanics and Mining Sciences 168, 105408.

SKB is responsible for managing spent nuclear fuel and radioactive waste produced by the Swedish nuclear power plants such that man and the environment are protected in the near and distant future.

**skb.se**